Synthesis of Au/Ag-CdS Nanostructures – Effect of Size and Shape on Photocatalytic Activity

A Thesis

Submitted in the fulfilment of the requirement for the degree of

Doctor of Philosophy

by

Rohit Singh

(Regn. No. 900909012)

Under the supervision of

Dr. Bonamali Pal

(Professor & Head)

School of Chemistry and Biochemistry

Thapar University

Patiala – 147004

Punjab, India

November, 2014

Certificate

This is to certify that thesis entitled "**Synthesis of Au/Ag-CdS Nanostructures – Effect of Size and Shape on Photocatalytic Activity**", being submitted by Rohit Singh in the fulfilment of the requirement for the award of Degree of Doctor of Philosophy to the School of Chemistry and Biochemistry, Thapar University, Patiala, is a record of candidate's own work carried out by him under my supervision and guidance. The matter presented in this thesis has not been submitted in part or full for the award of any degree in any other University or Institute.

(Supervisor)

Dr. Bonamali Pal
Professor & Head
School of Chemistry and Biochemistry
Thapar University, Patiala - 147 004
Punjab (India)

Candidate's Declaration

I, hereby declare that the work presented in the thesis entitled "**Synthesis of Au/Ag-CdS Nanostructures – Effect of Size and Shape on Photocatalytic Activity**" in fulfilment of the requirement for the award of the Degree of Doctor of Philosophy, School of Chemistry and Biochemistry, Thapar University, Patiala, is an authentic record of my own work carried out under the supervision of Dr. Bonamali Pal, Associate Professor, School of Chemistry and Biochemistry, Thapar University, Patiala, India. The matter embodied in this thesis has not been submitted in part or full to any other university or institute for the award of any degree in India or Abroad.

Rohit Singh

(Supervisor)

Dr. Bonamali Pal
Professor & Head
School of Chemistry and Biochemistry
Thapar University, Patiala - 147 004
Punjab (India)

Dedicated to
My
Parents and Teachers

I am indebted to my father for living, but to my teacher for living well

Alexander the Great

Acknowledgements

I humbly prostrate myself before the Almighty God for his grace and enduring blessings which enabled me to complete this work successfully with my full satisfaction.

First and foremost, I would like to express my sincere gratitude to my research supervisor ***Dr. Bonamali Pal,*** *for introducing me to this exciting field of science and for his valuable guidance, continuous support, motivation and patience throughout the Ph.D. work. I have learnt extensively from his, including how to regard an old question from a new perspective and how to approach a problem by systematic thinking. His persistent courage and confidence will always inspire me, and I hope to continue to work with his noble thoughts. I am really glad to be associated with a person like him in my life.*

I am profoundly obliged to ***Dr. Satnam Singh****, Associate Professor and Head, School of Chemistry and Biochemistry, Thapar University, Patiala for their good wishes and motivation.*

I would like to thank my doctoral committee for their encouragement, constructive criticism and inspirations.

Special regards to my beginning teachers and teachers of the School of Chemistry and Biochemistry for providing suggestions and taking interest in the progress of work along with lab facility. Deep sense of gratitude to all because of whose teaching at different stages of education has made it possible for me to see this day.

I am thankful to my lab-mates and other friends for always standing by my side and sharing a great relationship as compassionate friends. I will forever cherish the warmth shown by them, whose smiling face always made me refreshing.

I would like to thank ***other staff*** *of the School of Chemistry and Biochemistry, Thapar University, Patiala for the constant official help and cooperation.*

I would like to pay high regards to my mother ***Mrs. Darvesh Kaur,*** *my father* ***Gian Singh,*** *my sister* ***Renu,*** *brother in law* ***Prince Pal*** *and my Nephew* ***Agam*** *for their love, affection, patience and blessings. I am extremely happy to fulfil their ultimate desire that today, I achieve.*

Most of the results described in this thesis would not have been possible without the help of laboratories at the institutes like, ***SAI,*** *Thapar University, Patiala,* ***SAIF,*** *Punjab University, Chandigarh,* ***AIRF,*** *Jawaharlal Nehru University, Delhi,* ***SAIF,*** *IIT Bombay,* *and Central Salt & Marine Chemicals Research Institute.*

I gratefully acknowledge, ***Department of Science and Technology (DST),*** *Government of India, for providing me financial support in the initial years and* ***Rajiv Gandhi National Fellowship Scheme (RGNF),*** *Ministry of Social Justice & Empowerment, India for financial support in the later years.*

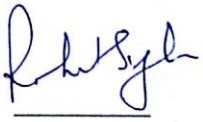

Rohit Singh

Table of Contents

Chapter	Section	Contents	Page No.
		List of Abbreviations	I-II
		List of Symbols	III
		Abstract	IV-VII
1		**Introduction**	**1-14**
	1.1	Photocatalysis	1-5
	1.1.1	CdS as a Photocatalyst and its crystallography	5-7
	1.2	Introduction to Nanomaterials	7
	1.2.1	Classification of nanostructured materials	7
	1.2.2	Quantum confinement effect	8
	1.3	Literature survey	8-10
	1.4	Motivation of thesis	10-11
	1.5	Objectives	11
	1.6	References	11-14
2		**Synthesis and Experimental Techniques**	**15-27**
	2.1	Materials	15-17
	2.2	Methods for the preparation of bare CdS and metal-CdS nanostructures	17
	2.2.1	Synthesis of CdS nanospheres	17
	2.2.2	Synthesis of CdS nanorods of different aspect ratios	17-18
	2.2.3	Synthesis of one dimensional (1D) CdS nanowires	18-19
	2.2.4	Deposition of Au, Ag and Cu nanoparticles onto CdS nanorods	19-20
	2.2.5	Preparation of silica coated CdS (SiO_2@CdS) nanorods	20
	2.2.6	Doping of Au, Ag and Cu (1-5 mol%) into CdS-NR	20
	2.2.7	Synthesis of Au nanoparticles of different shapes	20-21

	2.2.8	Synthesis of spatial alignment of Au-CdS nanostructures	21
	2.2.9	Au doped CdS/ TiO2 solar cells preparation	21
	2.3	Characterizations	21
	2.3.1	UV-vis spectrophotometer	21-22
	2.3.2	UV-Vis diffuse reflectance spectrophotometer	22
	2.3.3	Photoluminescence (PL) measurement	22
	2.3.4	Time resolved spectroscopy	22-23
	2.3.5	Scanning electron microscopy (SEM)	23
	2.3.6	Energy Dispersive X-ray (EDX) spectrophotometer	23
	2.3.7	Transmission electron microscopy (TEM)	23
	2.3.8	X-ray diffraction analysis	23
	2.3.9	Surface area analysis	23
	2.3.10	Current – voltage (I-V) characteristics	23-24
	2.3.11	High Performance Liquid Chromatography (HPLC)	24
	2.3.12	Gas chromatography-mass spectroscopy (GC-MS)	24
	2.3.13	Gas chromatography (GC)	24
	2.3.14	Magnetic susceptibility	24
	2.4	Photocatalytic reaction setups	24
	2.4.1	Photocatalytic reactor with Hg (UV) light source	24-25
	2.4.2	Sunlight as a visible light source	25-26
	2.5	References	27
3		**Enhanced Photocatalytic Activity of Coinage Metal-Cadmium Sulfide Nanorod Composites under Sun Light Irradiation**	**28-39**
	3.1	Introduction	28-29
	3.2	Experimental section	29
	3.2.1	Synthesis of CdS nanospheres and nanorods	29
	3.2.2	Deposition of Au, Ag and Cu NPs onto CdS-NR	29
	3.2.3	Photocatalytic reactions	29-30

	3.2.4	Characterization	30
	3.3	Results and discussion	30
	3.3.1	Optical study	30-31
	3.3.2	Morphological study	31-32
	3.3.3	Photodegradation of salicylic acid	32
	3.3.3.1	Effect of catalyst shape	32
	3.3.3.2	Effect of solution pH	32-33
	3.3.3.3	Effect of catalyst amount	33-34
	3.3.3.4.	Effect of concentration	34
	3.3.3.5	Effect of light intensity	34-35
	3.3.3.6	Effect of nature of metal deposition	35-36
	3.3.3.7	Kinetic study	36-37
	3.4	References	38-39
4		**Fine-tuning the Photoluminescence and Photocatalytic Properties of CdS Nanorods of Varying Dimensions**	**40-54**
	4.1	Introduction	41-42
	4.2	Experimental details	42
	4.2.1	CdS-NR of different aspect ratios and Au and Ag (1-2 wt%) photodeposition	42
	4.2.2	Photocatalytic activity	42
	4.2.3	Characterizations	42
	4.3	Results and discussion	42
	4.3.1	Morphological analysis	42-46
	4.3.2	Structural analysis	46-47
	4.3.3	Optical properties	47-50
	4.3.4	Photochemical activity of CdS samples	50-52
	4.4	References	53-54
5		**Study of Excited Charge Carrier's Lifetime for the Observed Photoluminescence and Photocatalytic Activity of CdS Nanostructures of Different Shapes**	**55-69**

5.1	Introduction	56-57
5.2	Experimental details	57
5.2.1	Synthesis of CdS nanostructures and their surface modifications	57
5.2.2	Preparation of silica coated CdS (SiO_2@CdS) nanorods	57
5.2.3	Photocatalytic activity	57
5.2.4	Characterizations	57
5.3	Results and discussion	57
5.3.1	Morphological and structural characterization	57-61
5.3.2	Optical spectroscopy	62-65
5.3.3	Photocatalytic activity study	65-68
5.4	References	69
6	**Highly Enhanced Photocatalytic Activity of Au Nanorod–CdS Nanorod Heterocomposites**	**70-89**
6.1	Introduction	71-72
6.2	Experimental details	72
6.2.1	Preparation of CdS and Au nanoparticles of different shapes	72
6.2.2	Preparation of Au–CdS junctions	72
6.2.3	Photocatalytic reaction	72
6.2.4	Characterizations	72-73
6.3	Results and discussion	73
6.3.1	Absorption study of Au-CdS nanocomposites	73-75
6.3.2	Morphological study	75-77
6.3.3	Photoluminescence spectroscopy	77-79
6.3.4	Time resolved spectroscopy	79-80
6.3.5	Structural properties of Au-CdS nanocomposites	80-81
6.3.6	Current-voltage characteristics	82-83
6.3.7	Photocatalytic study	83-84
6.3.7.1	Recyclability test	84-87

	6.4	References	88-89
7		**Woollen Bun like CdS Microspheres Wrapped with Lengthy Nanowires Exhibit Superior Photoactivity for Dye Degradation Under Sunlight**	**90-100**
	7.1	Introduction	91
	7.2	Experimental Section	91
	7.2.1	Synthesis of CdS nanowires	91
	7.2.2	Photocatalytic reactions	91-92
	7.2.3	Characterizations	92
	7.3	Results and Discussion	92
	7.3.1	Structural analysis of CdS nanostructures	92
	7.3.2	SEM/TEM analysis of CdS nanostructures	93-95
	7.3.3	Optical study	95-96
	7.3.4	Photoactivity study	96-99
	7.4	References	100
8		**Preparation of Coinage Metal doped CdS Nanorods for Highly Improved Photocatalytic Oxidation and Reduction Processes.**	**101-115**
	8.1	Introduction	101-102
	8.2	Experimental section	102
	8.2.1	Synthesis of coinage metal doped CdS-NR	102
	8.2.2	Photocatalytic and other properties	102
	8.2.3	Characterizations	102
	8.3	Results and discussion	102
	8.3.1	Optical study	102-105
	8.3.2	Structural analysis	105-110
	8.3.3	Morphological and composition study	111
	8.3.4	Photocatalytic study	111-115
	8.4	References	116
		Conclusions	**116-120**

List of Abbreviations

UV	Ultraviolet
Vis	Visible
DRS	Diffuse reflectance spectroscopy
SEM	Scanning electron microscopy
FEG-SEM	Field emission gun scanning electron microscope
HPLC	High pressure liquid chromatography
GC	Gas chromatography
GC-MS	Gas chromatography - mass spectrometry
TEM	Transmission electron microscopy
XRD	X-ray diffraction
SAED	Selected area electron diffraction
HRTEM	High resolution transmission electron microscopy
BET	Brunauer Emmett Teller
PL	Photoluminescence
JCPDS	Joint committee on powder diffraction standards
EDX	Energy dispersive X-ray spectroscopy
SA	Salicylic acid
PNP	p-nitrophenol
PAP	p-aminophenol
MB	Methylene blue
RhB	Rhodamine B
m-DNB	*meta*-dinitrobenzene
m-NA	*meta*-nitroaniline
m-PDA	*meta*-phenylenediamine
VB	Valence band
CB	Conduction band
SC	Semiconductor
M	Metal
NS	Nanosphere
NR	Nanorod
NW	Nanowire

NP	Nanoparticle
NC	Nanocrystals
1D	One dimensional
0D	Zero dimensional
QD	Quantum dot
SP	Surface plasmon
SPR	Surface plasmon resonance
LSP	Longitudinal surface plasmon
TSP	Transverse surface plasmon
DOS	Density of states
wt%	Weight percent
L	Length
W	Width
ml	Millilitre
min	Minute
mol	Mole
mM	Milli molar
nm	Nanometre
AR	Aspect ratio
mM	Milimolar
PCA	Photocatalytic activity
SI	Supporting information
a.u.	Arbitrary unit
c.a.	Calculated amount
AAM	Anodic alumina membrane
c-NS	Cubic-nanosphere
h-NS	Hexagonal nanosphere
AC	Autoclaved
RF	Refluxed
at%	Atomic percentage
wt%	Weight percentage
vol%	Volume percentage
ppm	Part per million

List of Symbols

e^-	Electron
h^+	Hole
$OH^{\cdot}$	Hydroxyl radical
E_g	Band gap
Å	Angstrom
α	Absorption coefficient
A	Absorbance
°	Degree
λ	Wavelength
%	Percentage
μ	Micro
θ	Theta
τ_{av}	Average lifetime
h	Hour
ϕ	Work function
E_o	Reduction potential
m	Meter
g	Gram
mg	Milligram
E_f	Fermi energy
V	Volt
d	Distance
s	Second
L	Length
W	Width
D	Diameter
I	Current
V	Voltage
MΩ	Mega ohm
C	Concentration
R	Resistance
S	Siemens
υ	Frequency

Abstract

This thesis presents a fine insight into many aspects of nanostructures and their applications in photocatalysis. Au/Ag − Cadmium sulfide (CdS) nanostructures viz., nanospheres, nanorods and nanowires of different dimensions have been synthesized to investigate the effect of size, shape, nature and spatial orientations of co-catalyst onto the change in photophysical, (absorbance, photoluminescence, relaxation lifetimes) and photocatalytic properties to achieve the best information in CdS nanostructures. The present thesis is divided into **eight** chapters:

Chapter 1: Introduction

The first chapter introduces the brief aspects and literature survey on semiconductor nanostructures with photocatalysis as an application point of view. Specific attention has been paid on cadmium sulfide (CdS) vis-à-vis their structure, morphology, their heterocomposites with coinage metals.

Chapter 2: Synthesis and Experimental Techniques

The second chapter gives a brief description of various techniques used for synthesis and characterize pure and Au/Ag-CdS nanocomposites. CdS nanostructures of different morphologies viz.; nanospheres, nanorods and nanowires have been synthesized by reverse micelles method, solvothermal and anodic alumina membrane (AAM) template techniques. Coinage metals were introduced onto CdS surface by means of in-situ deposition, photodeposition, impregnation and doping techniques.

To understand the potential of CdS nanostructures, a deeper knowledge of their overall properties is required. Therefore, the synthesized materials have been characterized by UV-vis, Diffused absorbance, Photoluminescence and Time resolved spectroscopy, Scanning electron microscope (SEM), Field emission-electron microscope (FE-SEM), Low resolution (TEM) and High resolution (HRTEM) Transmission microscope, BET surface analyzer, X-ray diffraction study. Electrical properties (resistance, current, voltage and conductance) were studied by current-voltage (IV) characteristics curves. Photochemical reactions were tested under both UV and direct sunlight irradiations. Products and intermediates have been identified by UV spectroscopy, High performance liquid chromatography (HPLC), Gas chromatography-Mass spectroscope (GC-MS) and Gas chromatography (GC) measurements.

Chapter 3: Enhanced Photocatalytic Activity of Coinage Metal-Cadmium Sulfide Nanorod Composites under Sun Light Irradiation

It deals with the influence of size, shape and nature of co-catalyst, pH and concentration of solution, catalyst amount, and light intensity for optimum photooxidation of salicylic acid (0.5 mM) by CdS nanostructures. The bare CdS nanorod exhibited higher photoactivity as compared to low activity of bare CdS (~10 nm) nanosphere and Au & Ag photodeposition highly improved the CdS nanorod photoactivity compared with Cu deposition. The fluorescence emission of CdS nanorod at 479 nm is also quenched due to metals deposition. It is observed that Au-CdS-nanorod composites completely degrade salicylic acid within 2 h of sun light exposure. The significant effect of Au-CdS photocatalytic activity on the various sizes (3.5 & 2 nm) of Au deposits has been observed during salicylic acid photodegradation.

Chapter 4: Fine-tuning the Photoluminescence and Photocatalytic Properties of CdS Nanorods of Varying Dimensions

The effect of aspect ratio, crystallinity, band gap energy, surface area and Au/Ag loading on the various photoactive properties of CdS nanostructures have been discussed here. CdS nanorods having different aspect ratio viz., 17 (length ~170 nm and width ~10 nm) and 28 (length ~140 nm and width ~5 nm) has been synthesized by solvothermal technique at different time intervals (2–10 h). The photocatalytic activity for salicylic acid oxidation under UV irradiation is gradually improved with the increasing crystallinity of CdS nanostructures, length (140 < 170 nm), exposed area (2358 < 5722 nm^2) per particle and decreasing surface area (158 < 122 < 76 m^2g^{-1}), surface to volume ratio (0.82 < 0.41 nm^{-1}) and aspect ratio (28 < 17). The deposition of 1–2 wt% Au (~3.5 nm) and Ag (~1.8 nm) nanoparticles onto CdS drastically quenched the emission and enhanced the photocatalytic activity.

Chapter 5: **Study of Excited Charge Carrier's Lifetime for the Observed Photoluminescence and Photocatalytic Activity of CdS Nanostructures of Different Shapes**

This chapter demonstrates the influence of the relaxation time of photoexcited charge species on the photoluminescence and photocatalytic activity for oxidation–reduction reactions by CdS nanostructures of different dimensions. CdS nanospheres (size ~10 nm) and different aspect ratio (17 and 23) CdS nanorods have been prepared by two different techniques. CdS nanorods formed by autoclaving is found to be more lengthy, wider (length ~170 nm and width ~10 nm) and having better crystallinity than CdS nanorods (length ~126 nm and width ~5.5 nm) prepared by refluxing under similar conditions. Relaxation lifetime of photoexcited electron–hole pairs is

measured to be 20, 24 and 116 μs for CdS nanosphere, shorter and longer CdS nanorod, respectively, seems to be responsible for the observed fluctuation in photoluminescence and photocatalytic activity. The photooxidation rate of salicylic acid (0.5 mM) and photoreduction of p-nitrophenol (0.2 mM) are significantly improved with increasing dimensions of CdS nanorods despite having a comparable surface area (81 and 76 $m^2 g^{-1}$) and CdS nanospheres (18 $m^2 g^{-1}$) exhibit poor photocatalysis. The better delocalization of charge species along the radial as well as longitudinal dimensions of CdS nanorods, higher crystallinity and delayed recombination time facilitate electrons or holes for active participation in the photoinduced reactions, and Au deposition always displayed superior photoactivity.

Chapter 6: Highly Enhanced Photocatalytic Activity of Au Nanorod–CdS Nanorod Heterocomposites

This chapter signifies the importance of different shapes of Au and CdS-nanoparticles for fabricating Au–CdS heterocomposites {prepared by mixing or impregnation of Au-nanosphere (9.1 nm), Au-nanorod (20 nm × 8.6 nm; L × W), CdS-nanosphere (10–12 nm) and CdS-nanorod (126 nm × 5.5 nm)} onto the photoluminescence and photocatalytic study. Second derivative absorption spectra's exhibit precise onset at 441 nm (CdS-nanosphere) and 469.5 nm (CdS-nanorod) that are significantly red-shifted to 509 nm (Au-nanosphere–CdS-nanosphere), 485 nm (Au-nanosphere–CdS-nanorod), 520 nm (Au-nanorod–CdS-nanosphere) and 485.5 nm (Au-nanorod–CdS-nanorod) depending upon interfacial contact-area. XRD patterns reveal the hexagonal phase of pure and Au–CdS nanocomposites. Photoluminescence of CdS nanorods has been effectively inhibited by modifying its surface with Au-nanoparticles (0.002–0.04 wt%). Relaxation lifetime of photoexcited charge-carriers found to be improved ca. 12.5 μs for Au-nanosphere–CdS-nanorod and 34 μs for Au-nanorod–CdS-nanorod due to effective charge transfer kinetics at the interface, in contrast to prompt charge-recombination (2.7 μs) in CdS. Under UV light (10.4 mW/cm^2) irradiation, Au-nanorod–CdS-nanorod exhibits the best photocatalytic activity for the oxidation of salicylic acid (86%, $k = 9 \times 10^{-3} min^{-1}$) and reduction of p-nitrophenol to p-aminophenol (53%) as a function of improved stability and better current–voltage (I–V) characteristics suitable for rapid charge transfer process during photoreaction.

Chapter 7: Woollen Bun like CdS Microspheres Wrapped with Lengthy Nanowires Exhibit Superior Photoactivity for Dye Degradation Under Sunlight

This chapter deals with the synthesis of woollen buns like CdS microspheres (2–5 μm) wrapped by lengthy, broader and crystalline hexagonal CdS nanowires (8–10 μm × 50–80 nm; L × W) via

anodic alumina membrane to achieve the best photoactivity for the decomposition of rhodamine B (50 μM) and methylene blue (20 μM) dyes under sunlight (50 $mWcm^{-2}$) irradiation in comparison to CdS nanospheres {cubic (~12 nm) and hexagonal (~15 nm) phase} and nanorods (170 nm × 10 nm). Higher crystallinity, least surface defects, better charge separation as evident from longer relaxation lifetime (3.6 ns) of photoexcited electron–hole pairs seems to be the cause for its outstanding performance and maximum (>80%) photoluminescence quenching. The largest surface area (1.42 μm^2), more surface exposed CdS molecules (2.5×10^6) and higher dye coverage (4.9×10^5) per–CdS nanowire led to the drastic improvement in the photoactivity. Many intermediate products and a linear increase in CO_2 production are quantified during rhodamine B degradation by CdS nanowires under different time periods of solar exposure.

Chapter 8: Preparation of Coinage Metal Doped CdS Nanorods for Highly Improved Photocatalytic Oxidation and Reduction Processes

This chapter introduce the doping of Au, Ag and Cu into CdS hexagonal nanorods with different mol ratio of metal/Cd^{2+} {$M_{1-x}Cd_xS$ (x = 0, 0.01, 0.02, 0.03, 0.05, 0.1)} by a facile solvothermal method. Results show that absorption and photoemission spectra of CdS exhibit a significant red-shift (506−532 nm) with luminescence quenching over 80% by varying the content and nature of dopant. Distortion in hexagonal crystal structure of CdS has been interestingly observed due to lattice mismatching of introduced coinage metal ions. The rate of photooxidation of salicyldehyde and photoreduction of nitroaromatics was remarkably influenced by the nature and concentration of doping metal. Many important parameters such as surface area, current-voltage characteristics, lattice distortion, magnetic properties, and crystallite size are correlated with photocatalytic properties.

Chapter 1: Introduction

1.1. Photocatalysis

The influential brief note on the electrochemical photolysis of water into H_2 and O_2 using titanium dioxide (TiO_2) as a semiconductor (SC) published by Fujishima and Honda [1] in 1972 initiate the development of semiconductor photocatalysis for a wide range of environmental and energy applications. Followed soon, a series of studies [2,3] were initiated to dispute on ideal TiO_2 in terms of its nature and the site at which the reaction occurs. In 1984, for the very first time, Serpone et al**.** showed [4-6] that the combination of two semiconductors such as CdS and TiO_2 led to a remarkable improvement in charge separation through interparticle electron transfer (IPET) pathway. Breakthrough of the 1990's studies by O'Regan and Graetzel in photosensitizing TiO_2 with a dye to produce electrical power, bring revolution in this area [7]. Thereafter, consistent efforts have been employed with pros and cons to develop visible light sensitive semiconductors or push the absorption onset of pristine TiO_2 toward longer wavelengths by surface modification with metal (M) and non-metal nanoparticles (NPs) [8-15].

Photocatalysis, light of energy greater than or equal to the band gap (the energy difference between the VB and the CB) of a semiconductor, excites an electron (e^-) from the valence band to the conduction band (CB) by leaving a positive hole (h^+) in the valence band (VB). These photogenerated charge carriers either can recombine on the surface (or in the bulk) of the particle in a fraction of seconds or capture in the surface states where they can react with donor or acceptor species to initiate various oxidation- reduction reactions.

Mechanism of photocatalysis

Valence band positive holes can oxidize water molecules present at the surface to produce •OH radicals, which consequently oxidize organic species to CO_2 and H_2O.

$$SC \xrightarrow[E \geq E_g]{h\upsilon} SC\,(e^-_{CB} + h^+_{VB}) \longrightarrow \text{Recombination}$$

$$SC\,(h^+_{VB}) + H_2O \longrightarrow OH^{\bullet} + H^+$$

$$OH^{\bullet} + \text{substrate} \longrightarrow H_2O + CO_2$$

Conduction band electrons can be rapidly trapped by molecular oxygen adsorbed on the semiconductor particle, and as a result, superoxide radicals ($O^{2\bullet-}$) are formed which may further react with H^+ to generate hydroperoxyl radical (•OOH).

$$SC\,(e^-_{VB}) + O_2 + H^+ \longrightarrow SC + HO_2^\bullet \rightleftharpoons SC + O_2^{\bullet-} + H^+$$

$$O_2^{\bullet-} + H^+ \longrightarrow {}^\bullet OOH$$

$${}^\bullet OOH + {}^\bullet OOH \longrightarrow H_2O_2 + O_2$$

$$H_2O_2 + SC\,(e^-_{VB}) \longrightarrow OH^\bullet + OH^-$$

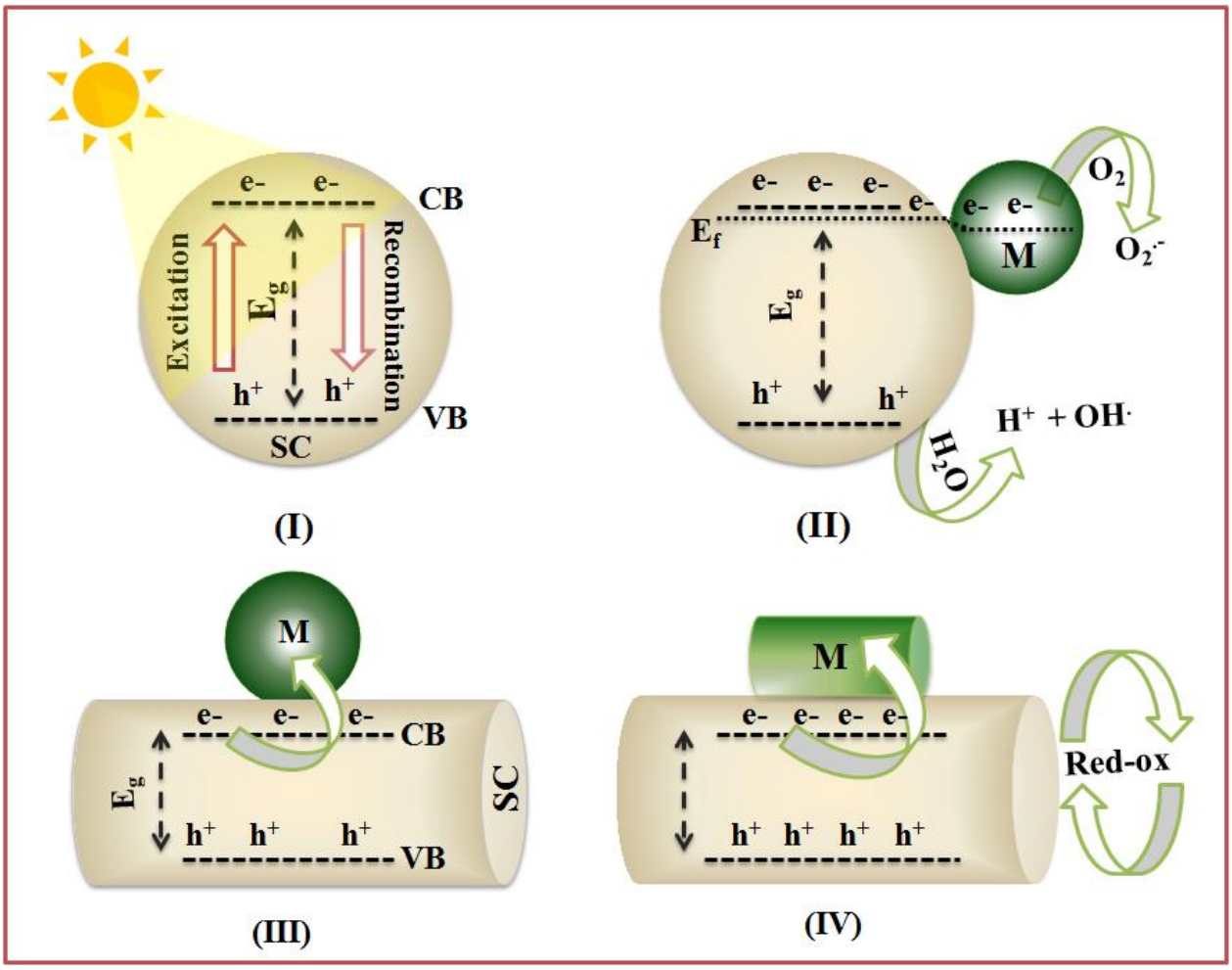

Fig. 1. Schematic illustration of charge-separation in various bare and M-SC nanocomposites.

Recently, it has been observed that the fate of *optoelectronic, photophysical and photochemical* properties of SC particle has been drastically changed by their size-, shape- and surface modifications with metal nanoparticles. The charge transfer at the bare SC and M-SC interface as a function of their geometrical modifications are presented in four cases (namely; case **I**, case **II**, case **III**, case **IV**) in Fig. 1.

Case I: First generation photocatalyst

In conventional photocatalysis, metal oxide (say TiO_2) semiconductor NP's were mainly investigated with a view of its nature of oxidative agent and the reaction sites [16-18]. But, instant recombination of photogenerated charge carriers and only absorb in the UV region was the major limitation in such type of single component semiconductor photocatalysis as it dilute the overall quantum efficiency [19-21]. During the recombination period, the excited electron reverts to the valence band without reacting with adsorbed species and dissipating the energy as light or heat. Several strategies have been adopted to sort out this problem, and improving the photocatalytic efficiency of single component material as either by morphological modifications, such as increasing surface area and porosity.

Case II: Metal–semiconductor heterocomposites

Low quantum efficiencies due to fast recombination of excited e^-/h^+ pairs and lack of satisfactory visible light response in a single component system give a strong thrust in the direction of M-SC heterocomposites [22-24]. Metal–semiconductor (M–SC) interface provides a unique pathway for capture, storage and discharges of photogenerated electrons [25-27]. In actual, metal in contact with semiconductor serves as a reservoir of photoelectrons, thus improving the interface charge-transfer process, which helps in retarding the recombination of photoexcited e^-/h^+ pairs [28,29]. When the work function of M is more than SC, there is a barrier formed at their interface, called the Schottky barrier and electrons will flow from SC to M until Fermi levels of M and SC are energetically aligned at the same level [30]. Choice of metal is done on the basis of their reduction potential, so that the metals which have lower reduction potential than SC photocatalyst are preferred, as more and more electrons get transferred to the metal and further to the reacting species. In this respect, spherical metal–semiconductor nano/ micro composites were mainly investigated to study their optical properties.

Case III: Importance of elongated nanostructures

It is well known that the CB and VB positions of a given SC are noted to vary depending on the size of particles. If the size is enough small, e.g., in the range of a few nanometers, it result in size quantization effect, smaller the size is the higher and lower is the positions of CB and VB, respectively, and hence the larger is the energy gap between the CB and VB.

Similarly, it is also well known that the Fermi energy of M-NPs changes with size and shifts to the negative direction with decreasing NPs size [29]. Hence, the charge transfer process by Fermi energy equilibrium at the M-SC interface is size and shape dependent as a function of their spatial arrangements.

Much emphasis has been done very recently to study various one dimensional (1D) elongated SC nanostructures, such as Nano– rods, wires, tubes, towers etc. [31-34]. Compared to spherical NP's, elongated morphologies of semiconductor have a higher potential due to higher photon absorption cross sections, controlled porosity, restrain aspect ratio, superior delocalization, higher relaxation lifetime and polarized light absorption scattering & emissions [31,35,36]. These 1D nanostructures, especially nanorods (NR) that are located between 0D quantum dots (QDs) to 1D nanowires (NW) found to be most suitable geometry in terms of the quantum confinement in radial or longitudinal direction due to limiting nanoscale dimensions, the superior delocalization of the charge carriers which reduces the e^-/h^+ overlap and exposed surface area of the NR that increases the probability for surface trapping. Furthermore continuous efforts are employed in the direction of making suitable geometry of spherical (M) nanoparticles – (SC) nanorod for drastic improvement in charge separation.

Case IV: Importance of metal – semiconductor interface

Difficulty in stabilization of small particles of monodisperse size by the use of conventional procedures often led to the aggregation of particles into large ones, which obscures their size-dependent photocatalytic activity. Time to time, different strategies have been adapted to control over their particles size and shape. Very interestingly, limited control over the size, shape and their distribution has been overcome by a simple ex-situ approach, where the NPs with different shapes are synthesized first, purified and deposited over the SC surface [37]. By considering different geometries with different orientation of M-SC nanocomposites, M-NR – SC-NR (rod-rod combination) supposed to have additional benefits owing to:

1. Double charge rectification - First, the 1D geometry leads to a fast and long-distance electron transport and which is supposed to rectify further by M-NR particle.
2. Extend the scope of charge transfer through a larger contact area of the interface, developed by NR-NR.
3. The light absorption and scattering can be obviously enhanced because of the high

length-to-diameter ratio of the elongated structure, which can be further improved by depositing metal with different shape.

A large number of metal oxides and sulfides have been examined as photocatalyst for a variety of applications. The major obstacle to progress in the development of a photocatalyst has been fulfilled by the following conditions;

- Band gap narrower than 3 eV for optimum absorption of light.
- Band edge potentials suitable for redox reactions.
- Stability during the overall photocatalytic reaction.

Absorption in the UV light ($\lambda < 380$ nm; approximately 3-4% of the solar radiation energy) and fast recombination of photoexcited charge carriers (e^-/h^+) in the wide band gap metal oxides ($E_g > 3$ eV; TiO_2, WO_3 and ZnO etc.) impair their applications to a greater extent [20,21]. In contrary, metal chalcogenides, especially, CdS emerge to be suitable material due to suitable band gap energies that are sufficiently low to permit absorption of visible light and having appropriate conduction and valence band positions for reduction and oxidation reactions.

1.1.1. CdS as a Photocatalyst and its crystallography

The direct band gap of CdS (bulk band gap 2.42 eV), simple tailoring of structures, anisotropic growth, visible light-driven sensitivity and suitable band edge positions gives it much more importance over others. Due to its suitable oxidation potential (+2.0 eV vs NHE), it is usually used for the wastewater treatment and decolourization and mineralization of dyes. It is also known to be one of the most potential photocatalyst because of their high reduction potential over Nitro group (-0.5 V). The conduction band position relative at negative potential (-0.4 eV) offer CdS excellent photocatalytic activities for the photoreduction of H^+ to H_2 and NO_2 to NH_2 [38,39]. Energy band positions of CdS in comparison to commonly used semiconducting materials, including the conduction and valence band positions, and the various parameters of the noble metals are given in Fig. 2.

Nevertheless, the photocatalytic efficiency of CdS is seriously restricted by the immediate recombination of e^-/h^+ pairs and its photocorrosion during the reaction, which resulted from itself oxidization by holes [39,40]. To shed light out this problem, elongated CdS nanostructures have been studied with the benefits of the extendable delocalization of

charge carriers, which prevents immediate charge recombination, contrary to nanospheres (NS) and secondly various metal NPs such as Au, Ag, Pt, Mn, Ni and Zn were deposited/ doped in the CdS-NPs to prevent the accumulation of charge [41-46]. In contrast to other metals, fascinating resonant behavior exhibited by Au, Ag and Cu after interacting with UV and visible light photons, stability, and size-, shape, Fermi level equilibration and composition dependent plasmonic interactions with solar spectrum [47-52] make them a promising candidate (act as antennae) for integrated with CdS.

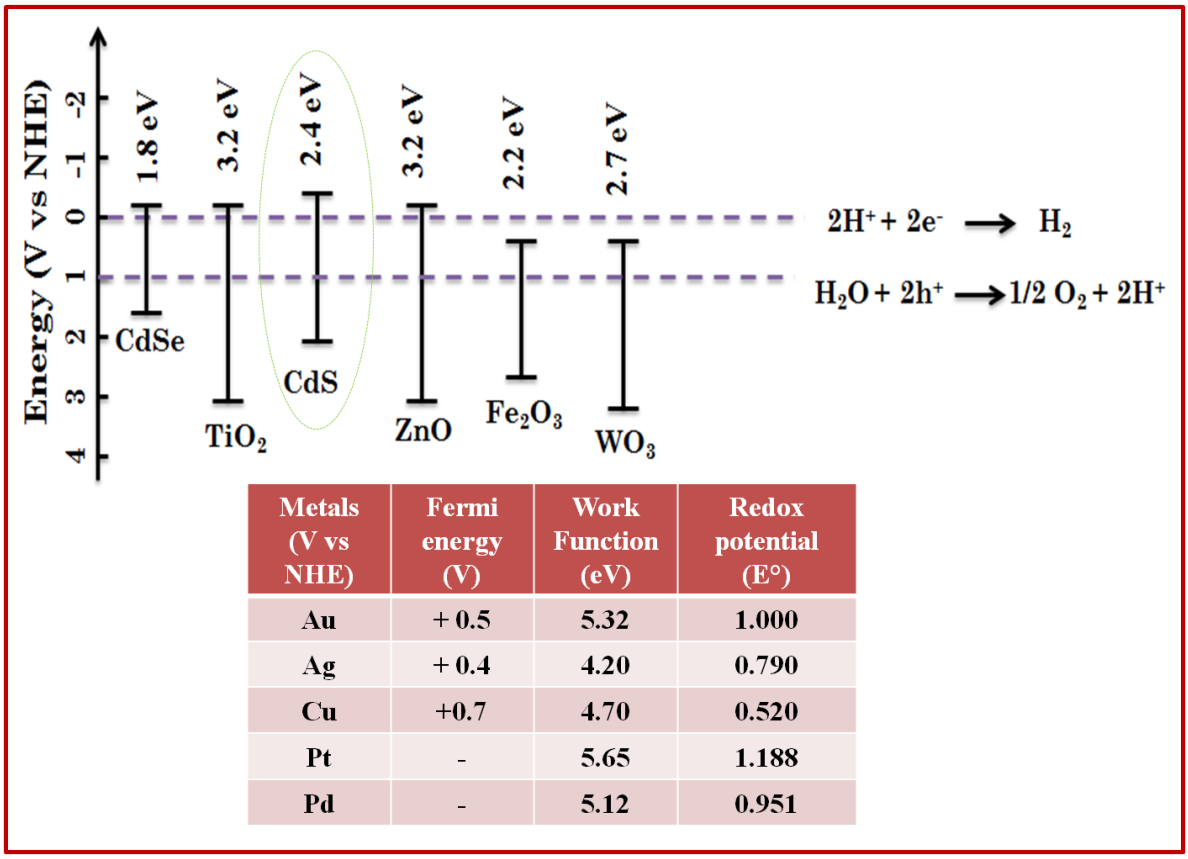

Metals (V vs NHE)	Fermi energy (V)	Work Function (eV)	Redox potential (E°)
Au	+ 0.5	5.32	1.000
Ag	+ 0.4	4.20	0.790
Cu	+0.7	4.70	0.520
Pt	-	5.65	1.188
Pd	-	5.12	0.951

Fig. 2. Energy band positions of common semiconducting materials and Fermi energy, work functions and reduction potential of the noble metals.

CdS have two kinds of structures, namely, the zinc blende crystal structure (cubic) and the wurtzite structure (hexagonal) as shown in Fig. 3. The stacking sequence of the close-packed planes of zinc blende is represented by the *ABCABCABC* repeating pattern, while that of wurtzite is represented by the *ABABAB* repeating pattern. The cadmium and sulfur atoms are four coordinate in both of these forms. The lattice constants and angles in the cubic and hexagonal system are $a = b = c$, $\alpha = \beta = \gamma = 90°$ and $a = b \neq c$, $\alpha = \beta = 90°$, $\gamma = 120°$ respectively.

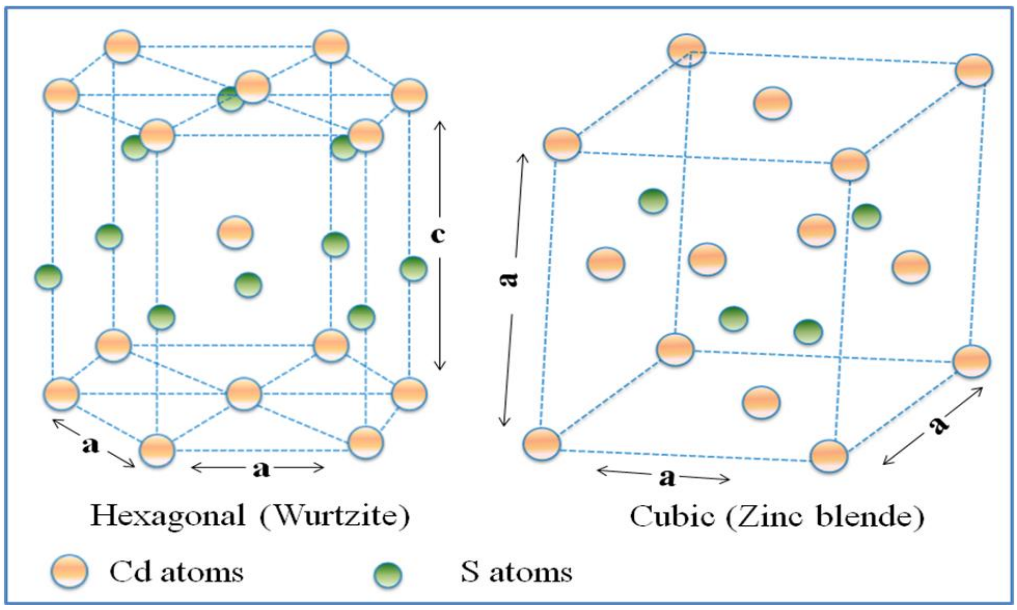

Fig. 3. Hexagonal and cubic crystallographic structure of CdS.

1.2. Introduction to Nanomaterials

The word 'Nano' is to a Greek prefix meaning dwarf or something very small and depicts one billionth (10^{-9}) of a unit. Nanomaterials, therefore, refers to the class of materials having at least one of its dimension in the nanoscale (1−100 nm).

1.2.1. Classification of nanostructured materials

Nanomaterials can be classified into four types according to their dimensionality (morphology & composition); 0D, 1D, 2D and 3D as shown below in Fig. 4.

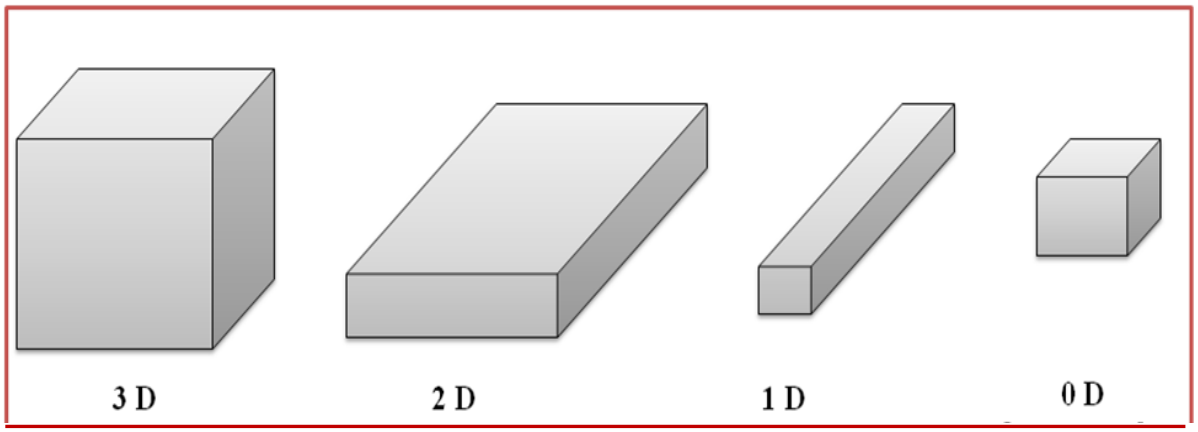

Fig. 4. Schematic diagram of classification of nanostructures.

1.2.2. Quantum confinement effect

Quantum concepts generally refer to energy levels, bandgaps, and conduction and valence band positions. Nanoclusters are comprised of a number of atoms and atoms have their well known atomic orbital's. Each of N atoms contributes with its atomic states to a band so that, although the width of a band increases slightly when more atoms are added, the density of states (DOS) within a band is basically proportional to the number of atoms. Size quantization of SC particles will lead to the change in the position of CB and VB to higher and lower values, respectively which result in widening of the band gap (Fig. 5).

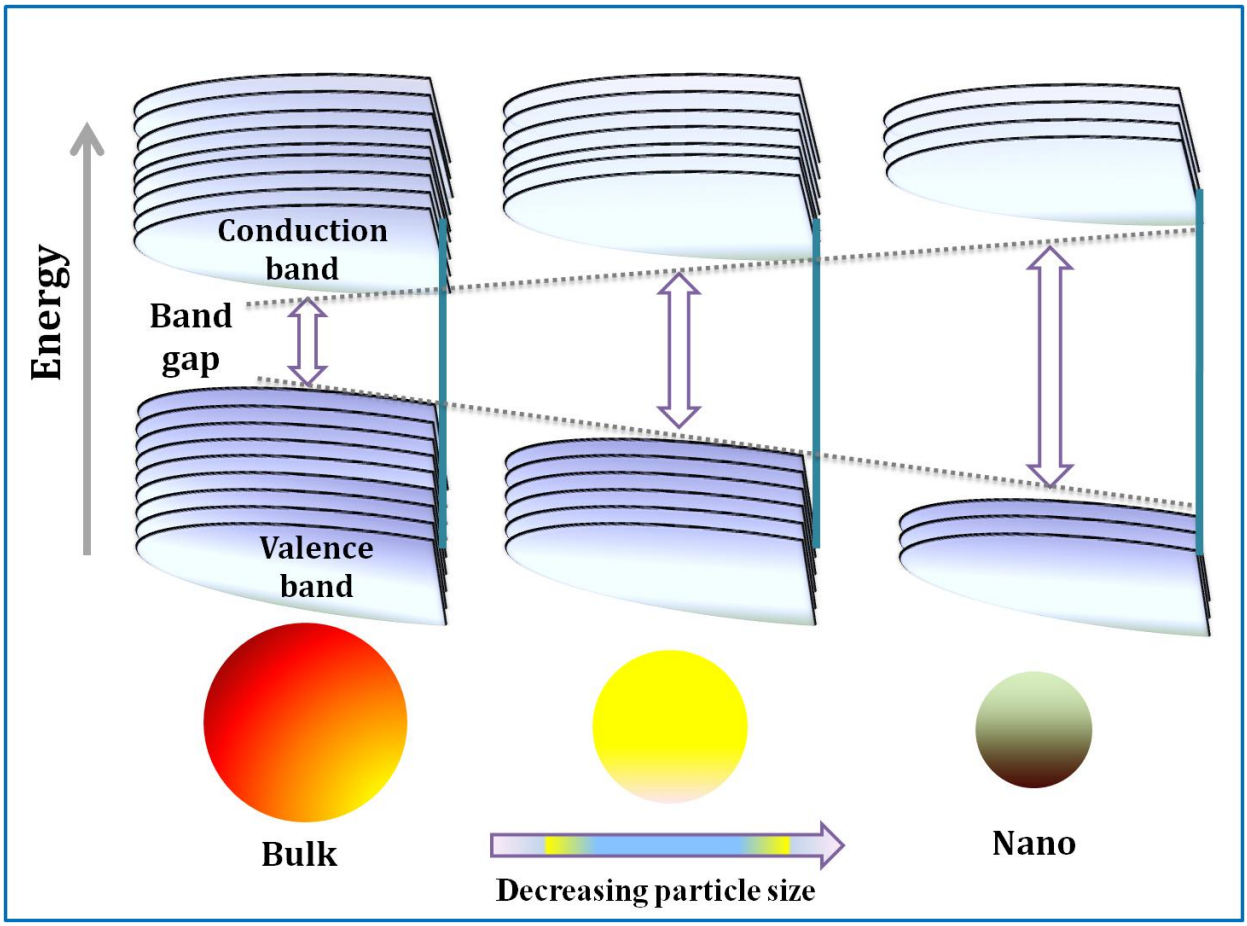

Fig. 5. Change in band gap and the density of states as the number of atoms in a system decreases.

1.3. Literature survey

Cadmium sulfide (CdS), a direct wide band gap semiconductor, found to be of special concern and investigated regarding of its synthesis and applications in a variety of disciplines.

Li et al. have successfully reported the controlled synthesis of CdS nanocrystals (NC) by controlling the reaction conditions such as reaction temperature, precursor concentration monomer linkage [53]. Kar et al. have discussed [54] the single crystalline CdS nanoribbons (width 200-400 nm and length few hundred micrometers) with a hexagonal wurtzite phase that have been achieved by thermal evaporation of CdS powder on Si wafers. Several techniques such as electrochemical deposition template method [55], hydrothermal [56], solvothermal [57], CVD-template assisted [58], thermal evaporation process [59] have been employed for the growth of CdS nanostructures; nanowires, nanorods, nanotubes, nanobelts, nanoribbons etc.

Time resolved emission studies of Ag-adenine-templated CdS (Ag/CdS) nanohybrids were investigated by the Yang group in detailed [60]. The observed changes in fluorescence behavior in terms of intensity, lifetime and spectral shift are nicely discussed by considering electronic interaction between Ag and CdS phases. Makori et al. attempted to selectively grow the Au-NC onto the CdS surface to avoid the growth of metal clusters over the entire rod, with less selectivity for the tips. Matchstick, dumbbell and double dumbbell like fascinating morphologies of Au-CdS has been successfully optimized by this group [61,62]. Au growth on the CdS nanorods by thermal and light induced routes has been reported by Uri Banin group for the observed change in photoluminescence [63].

Photo-catalytic H_2 production activity of CdS nanorods was tested and compared with bulk CdS, calcined CdS, noble metal (0.2% Pt) loaded CdS by Janet et al. Surface area, pore volume and band gap were correlated to justify the observed change [38]. Growth mechanism and optical properties of CdS nanostructures as a function of reaction time and surfactants (cationic and anionic) were studied by Pandey et al. They have found that size of CdS-NPs increased with an increase in reaction time, and a dramatic shape conversion from spherical to triangular, star-shaped, and geodesic spheres has evolved on prolongation of reaction time [65].

Reduction of nitrobenzene to azoxybenzene [39] yield (28%) by CdS-NPs was increased up to 68% by Rh loaded core-shell structure of CdS nanocomposites. It was found that nitrosobenzene was the main product without loading of Rh metal. H. Yang et al. nicely reported [66] the solution phase synthesis of CdS nanorods and Au nanocrystals of ~ 2 nm in

diameter were grown on the CdS surface in the presence of $NaBH_4$. The deposition of Au-NC on the CdS nanorods resulted in a dramatic quenching of luminescence. Khon et al. scrutinized the nature of exciton-Plasmon interactions in Au-tipped CdS nanorods and observed that strongly coupled systems promote mixing of electronic states at semiconductor-metal domain interfaces, which causes a significant suppression of both Plasmon and exciton excitations of carriers [67].

The satisfactory information on the benefits of nanorods over nanospheres as a function of the increased delocalization of charge carriers along the length and their large surface area has been nicely given by Sitt et al [36]. A thin layer of silica was successfully coated (1-1.3 nm) over the CdS-NR surface [39,68] to improve its stability and activity for a long term, as CdS undergo photo dissolute under UV light irradiation. Similarly, doping of Ni, Zn [44,45] into CdS was investigated for facilitates electron/hole pair separation and to prevent its photocorrosion.

1.4. Motivation of Thesis

From the critical literature review it has been found that most of the work is done regarding the synthesis of Au and CdS nanostructures of different shape and sizes. Up to this date, much effort has been employed to elucidate the growth mechanism, optical, structural, fluorescence emission properties to achieve the best information on CdS and Au-CdS nanostructures. It has been concluded that:

- Mainly optical and structural properties of CdS-NR were studied, but very few reports on their size and shape dependent photo-oxidation and reduction reactions.
- The correlation of the photoluminescence and photoactivity of CdS as a function of their tunable aspect ratios, surface and structural parameters, defects has not been considered.
- Au/CdS nanocomposites are mainly investigated for growth mechanism, interactions, and their photoluminescence properties, but their impact onto the controlled photoredox reactions is rarely observed.
- Spherical Au-NPs were mainly investigated over the CdS surface, but impact of other asymmetric arrangements of Au-CdS nanostructures for the overall change in optoelectronic and photochemical properties are never discussed.

Out of four possible combinations i.e., sphere (M) – sphere (SC), sphere (M) – rod (SC), rod (M) – sphere (SC) and rod (SC) – rod (M) for the metal (M) – semiconductor (SC) alignments, only first two nanostructures has been studied in the literature. To the best of our knowledge there is no report about the other two alignments and their optical and photocatalytic properties. Therefore, it should be very interesting to align or assemble this size and shape dependent heterocomposites and study their optical absorption, fluorescence emission and photocatalytic redox reactions.

1.5. Objectives

Keeping in view the above points, the following objectives have been designed.

[1] Synthesis of Au/Ag and CdS nanoparticles of different sizes and shapes.

[2] To study and characterize alignment of Au/Ag nanoparticles on CdS nanostructures.

[3] To investigate the photocatalytic activity of M-SC composites for the photodegradation of phenol/salicylic acid and photoreduction of nitroaromatics.

1.6. References

[1] A. Fujishima, K. Honda, Nature 238 (1972) 37−38.

[2] H.D. Duong, N. Serpone, M. Graetzel, Helv. Chim. Acta 67 (1984) 1012−1018.

[3] N. Serpone, E. Pelizzetti, M. Graetzel, Coord. Chem. Revs. 64 (1985) 225−245.

[4] N. Serpone, E. Borgarello, M. Graetzel, J. Chem. Soc. Chem. Commun. 1984, 342−344.

[5] N. Serpone, E. Borgarello, E. Pelizzetti, J. Electrochem. Soc. 135 (1988) 2760−2766.

[6] N. Serpone, P. Maruthamuthu, P. Pichat, E. Pelizzetti, H. Hidaka, J. Photochem. Photobiol., A 85 (1995) 247−255.

[7] B. O'Regan, M. Grätzel, Nature 353 (1991) 737–740.

[8] S. Matsuda, A. Kato, Appl. Catal. 8 (1983) 149−165.

[9] M. Inomata, A. Miyamoto, Y. Murakami, J. Chem. Soc., Chem. Commun. 1980, 233−234.

[10] F.A. Luck, Bull. Soc. Chim. Belg. 100 (1991) 781−800.

[11] S. Sato, Chem. Phys. Lett. 123 (1986) 126−128.

[12] R. Asahi, T. Morikawa, T. Ohwaki, K. Aoki, Y. Taga, Science 293 (2001) 269−271.

[13] T. Ohno, M. Akiyoshi, T. Umebayashi, K. Asai, T. Mitui, M. Matsumura, Appl. Catal., A 265 (2004) 115−121.

[14] M. Anpo, Catal. Surv. Jpn. 1 (1997) 169−179.

[15] H. Kisch, L. Zang, C. Lange, F.W. Maier, C. Antonius, D. Meissner, Angew. Chem., Int. Ed. 37 (1998) 3034−3036.

[16] S.N. Frank, A.J. Bard, J. Am. Chem. Soc. 99 (1977) 303–304.

[17] G.N. Schrauzer, T.D. Guth, J. Am. Chem. Soc. 99 (1977) 7189–7193.

[18] B. Kreutler, A.J. Bard, J. Am. Chem. Soc. 100 (1978) 4317–4318.

[19] Y. Shiraishi, Y. Togawa, D. Tsukamoto, S. Tanaka, T. Hirai, ACS Catal. 2 (2012) 2475−2481.

[20] J. Zhang, Y. Wang, J. Zhang, Z. Lin, F. Huang, J. Yu, Appl. Mater. Interfaces 5 (2013) 1031−1037.

[21] Q. Deng, X. Duan, D.H.L. Ng, H. Tang, Y. Yang, M. Kong, Z. Wu, W. Cai, G. Wang, ACS Appl. Mater. Interfaces 4 (2012) 6030−6037.

[22] A.V. Emeline, N. Serpone, J. Phys. Chem. B 106 (2002) 12221−12226.

[23] N. Serpone, A.V. Emeline, Res. Chem. Intermed. 31 (2005) 391−432.

[24] A.V. Emeline, A.V. Frolov, V.K. Ryabchuk, N. Serpone, J. Phys. Chem. B 107 (2003) 7109−7119.

[25] A. Takai, P.V. Kamat, ACS Nano 4 (2011) 7369–7376.

[26] R. Chapman, P. Mulvaney, Chem. Phys. Lett. 349 (2001) 358–362.

[27] H. Choi, W.T. Chen, P.V. Kamat, ACS Nano 5 (2012) 4418–4427.

[28] A. Wood, M. Giersig, P. Mulvaney, J. Phys. Chem. B 105 (2001) 8810–8815.

[29] V. Subramanian, E.E. Wolf, P.V. Kamat, J. Phys. Chem. B 107 (2003) 7479–7485.

[30] Z. Zhang, J.T. Yates, Chem. Rev. 112 (2012) 5520–5551.

[31] B. Sun, N.C. Greenham, Phys. Chem. Chem. Phys. 8 (2006) 3557−3560.

[32] T. Zhai, X. Fang, L. Li, Y. Bando, D. Golberg, Nanoscale 2 (2010) 168–187

[33] J.G. Zhao, Z.H. Hua, Y. Yao, Superlattices Microstruct. 61 (2013) 146–151

[34] M. Muruganandham, Y. Kusumoto, C. Okamoto, A. Muruganandham, M.A. Al-Mamun, B. Ahmmad, J. Phys. Chem. C 113 (2009) 19506–19517.

[35] P.D. Cozzoli, A. Kornowski, H. Weller, J. Am. Chem. Soc. 125 (2003) 14539–14548.

[36] A. Sitt, A. Salant, A. Menagen, U. Banin, Nano Lett. 11 (2011) 2054–2060.

[37] A. Salant, M. Shalom, Z. Tachan, S. Buhbut, A. Zaban, U. Banin, Nano Lett. 12 (2012) 2095–2100.

[38] C.M. Janet, R.P. Viswanath, Nanotechnology 17 (2006) 5271–5277.

[39] B. Pal, T. Torimoto, K.I. Okazakib, B. Ohtani, Chem. Commun. (2007) 483–485.

[40] K. Wu, H. Zhu, Z. Liu, W.R. Córdoba, T. Lian, J. Am. Chem. Soc. 134 (2012) 10337−10340.

[41] T. Shanmugapriya, P. Ramamurthy, J. Phys. Chem. C 117 (2013) 12272−12278

[42] A. Kumar, V. Chaudhary, J. Photochem. Photobiol., A 189 (2007) 272–279.

[43] R. Zeng, M. Rutherford, R. Xie, B. Zou, X. Peng, Chem. Mater. 22 (2010) 2107−2113.

[44] M. Luo, Y. Liu, J. Hu, H. Liu, J. Li, ACS Appl. Mater. Interfaces 4 (2012) 1813−1821

[45] F. Yang, N.N. Yan, S. Huang, Q. Sun, L.Z. Zhang, Y. Yu, J. Phys. Chem. C 116 (2012) 9078−9084.

[46] X. Zhang, Y.L. Chen, R.S. Liu, D.P. Tsai, Rep. Prog. Phys. 76 (2013) 1−41.

[47] S. Linic, P. Christopher, D.B. Ingram, Nat. Mater. 10 (2011) 911–921.

[48] H. Zhu, X. Ke, X. Yang, S. Sarina, H. Liu, Angew. Chem. Int. Ed. 49 (2010) 9657–9661.

[49] J. R. Adleman, D.A. Boyd, D.G. Goodwin, D. Psaltis, Nano Lett. 9 (2009) 4417–4423.

[50] P.V. Kamat, J. Phys. Chem. B 106 (2002) 7729–7744.

[51] S.D. Borse, S.S. Joshi, Adv. Chem. Lett. 1 (2013) 15-23.

[52] M.A. El-Sayed, Acc. Chem. Res. 34 (2001) 257–264.

[53] Y. Li, X. Li, C. Yang, Y. Li, J. Mater. Chem. 13 (2003) 2641–2648.

[54] S. Kar, B. Satpati, P. V. Satyam, S. Chaudhuri, J. Phys. Chem. B 109 (2005) 19134-19138.

[55] D. Routkevitch, T. Bigioni, M. Moskovits, J. M. Xu, J. Phys. Chem. 100 (1996) 14037–14047.

[56] F. Chen, R. J. Zhou, L. G. Yang, M. M. Shi, G. Wu, M. Wang, H. Z. Chen, J. Phys. Chem. C 112 (2008) 13457–13462.

[57] Y.X. Li, Y.F. Hu, S.Q. Peng, G.X. Lu, S.B. Li, J. Phys. Chem. C 113 (2009) 9352–9358.

[58] X.P. Shen, A.H. Yuan, F. Wang, J.M. Hong, Z. Xu, Solid State Commun. 133 (2005) 19–22.

[59] Y.K. Liu, J.A. Zapien, C.Y. Geng, Y.Y. Shan, C.S. Lee, Y. Lifshitz, S.T. Lee, Appl. Phys. Lett. 85 (2004) 3241–3243.

[60] A. Kumar, V. Chaudhary, Nanotechnology 20 (2009) 1-10.

[61] S.E. Habas, P. Yang, T. Mokari, J. Am. Chem. Soc. 130 (2008) 3294-3295.

[62] T. Mokari, Nano Rev. 2 (2011) 5983.

[63] G. Menagen, J.E. Macdonald, Y. Shemesh, I. Popov, U. Banin, J. Am. Chem. Soc. 131 (2009) 17406–17411

[64] M. Sathish, B. Viswanathan, R.P. Viswanath, Int. J. Hydrogen Energy 31 (2006) 891– 898

[65] G. Pandey, S. Dixit, J. Phys. Chem. C 115 (2011) 17633–17642.

[66] H. Yang, Metals Mater. Int. 12 (2006) 351–355.

[67] E. Khon, A. Mereshchenko, A.N. Tarnovsky, K. Acharya, A. Klinkova, N.N. Hewa- Kasakarage, I. Nemitz, M. Zamkov, Nano Lett. 11 (2011) 1792–1799.

[68] N. Gupta, B. Pal, J. Colloid Interface Sci. 368 (2012) 250–256.

Chapter 2: Synthesis and Experimental Techniques

2.1. Materials

(I) Cadmium sulfide precursors

1) Cadmium nitrate tetrahydrate ($Cd(NO_3)_2.4H_2O$)
2) Cadmium chloride ($CdCl_2$)
3) Cadmium acetate ($Cd(CH_3COO)_2.\ 2H_2O$)
4) Sodium sulfide ($Na_2S.9H_2O$)
5) Thiourea ($SC(NH_2)_2$)

(II) Solvents used for the catalyst preparations

1) Ethylenediamine ($H_2NCH_2CH_2NH_2$)
2) Heptane (C_7H_{16})
3) Toluene (C_7H_8)

(III) Materials used for the catalysts washing process

1) Ethanol (C_2H_5OH)
2) Methanol (CH_3OH)
3) Acetone (C_3H_6O)
4) Milli-Q water with conductivity 35 mho cm^{-1} at 25°C

(IV) Materials/solvents used in photodeposition techniques

1) Hydrogen tetrachloroaurate (III) hydrate ($HAuCl_4.xH_2O$)
2) Silver nitrate ($AgNO_3$)
3) Cupric nitrate ($CuNO_3.4H_2O$)
4) Isopropanol (C_3H_7OH)
5) Milli-Q water

(V) Surfactants used

1) Cetyltrimethylammonium bromide (CTAB)
2) Sodium di(2-ethylhexyl)sulfosuccinate (AOT)

(VI) Silica precursors used

1) Tetraethoxysilane (TEOS)
2) 3-mercaptopropyltrimethoxysilane (MPTMS)

(VII) Reducing agents used

1) Sodium borohydride ($NaBH_4$)
2) Ascorbic acid ($C_6H_8O_6$)

(VIII) Filters/membranes used during washing/preparation conditions

1) Anodic alumina membrane (AAM) of approximately 50 nm in pore size
2) Cellulose of 0.22 µm pore size

(IX) Model organic compounds/pollutants

1) Salicylic acid ($C_6H_4(OH)COOH$)
2) Rhodamine B ($C_{28}H_{31}ClN_2O_3$)
3) Methylene Blue ($C_{16}H_{18}N_3SCl$)
4) Salicyldehyde ($C_7H_6O_2$)
5) p-nitrophenol ($C_6H_5NO_3$)
6) p-aminophenol (C_6H_7NO)
7) m-dinitrobenzene ($C_6H_4N_2O_2$)
8) m-nitroaniline ($C_6H_6N_2O_2$)
9) m-phenylenediamine ($C_6H_8N_2$)
10) p- nitrobenzaldehyde ($C7H5NO_3$)

(X) Solvents used in HPLC

1) Water (H_2O)
2) Methanol (CH_3OH)
3) Acetonitrile (C_2H_3N)

(XI) Materials used in solar cells

1) TiO_2 (P25, Degussa)
2) Acetyl acetone
3) Fluoride-doped tin dioxide (SnO_2:FTO)
4) Triton –X 100
5) Ruthenium-polypyridine dye
6) Chloroplatinic acid hexahydrate (H_2PtCl_6)
7) Iodide electrolyte solution

(XII) Purging sources for inert atmosphere

1) Nitrogen
2) Argon

XIII) Additional solvents used

1) Nitric acid (HNO_3)
2) Sodium hydroxide (NaOH)
3) Ammonium hydroxide (NH_4OH)

Most of the chemicals were purchased from Loba Chemicals and Sigma Aldrich and used without any further purification.

2.2. Methods for the preparation of bare CdS and metal-CdS nanostructures

2.2.1 Synthesis of CdS nanospheres

Cadmium sulfide (CdS) nanospheres (CdS-NS) with ***cubic phase*** have been synthesized by a reverse micelle [1] method: Typically 1.3 ml (1.0 M) aqueous solution of Cd $(NO_3)_2.4H_2O$ and $Na_2S.9H_2O$ was added separately to 200 ml of heptane solution containing 14 g of sodium di(2-ethylhexyl)-sulfosuccinate (AOT) and 5.7 ml of water. After that each of solution was stirred for 1h, and mixed together with homogeneous stirring, which resulted in the formation of yellow colored suspension. Then resulting solution was centrifuged, and washed with distilled water and methanol repeatedly to get rid of the extra surfactant. The final product was dried in an oven at 50 $^{\circ}$C.

CdS-NS with ***hexagonal phase*** has been prepared *(chapter 1, ref. 65)* as; A solution of cadmium acetate (5 mmol; 1.33 g in 50 ml) was prepared. To an aqueous solution of thiourea (20 mmol; 1.52 g in 100 ml), an aqueous solution of NaOH was added to make it (pH = 9.5) alkaline and added to above Cd (II) solution. Surfactant CTAB (1mmol; 0.365 g in 20 ml DI water) was added to the resulting mixture in order to control the particles growth. The reaction mixture was refluxed on a water bath for 0.5 h at 90 $^{\circ}$C in constant supply of water cooling. As obtained final product was centrifuged, washed with distilled water and methanol repeatedly and dried in an oven at 50 $^{\circ}$C.

2.2.2 Synthesis of CdS nanorods of different aspect ratios

CdS nanorods (CdS-NR) of a different aspect ratio were successfully synthesized by phase growth solution method [2]. Typically, mixture of cadmium nitrate (0.888 g) and thiourea (0.438 g) and ethylenediamine (72 ml) were put into Teflon-lined stainless steel autoclave of 80 ml capacity and treated at 120 $^{\circ}$C for different time periods i.e., 2, 6 and 10 h to get the desired product (namely CdS-2h, CdS-6h and CdS-10h). Similarly, CdS-NR with different dimensions was prepared by refluxing of corresponding salts in ethylenediamine under the similar

conditions. The reaction was cooled to room temperature and yellow precipitates were washed repeatedly with methanol and DI water and dried in oven at 50 °C

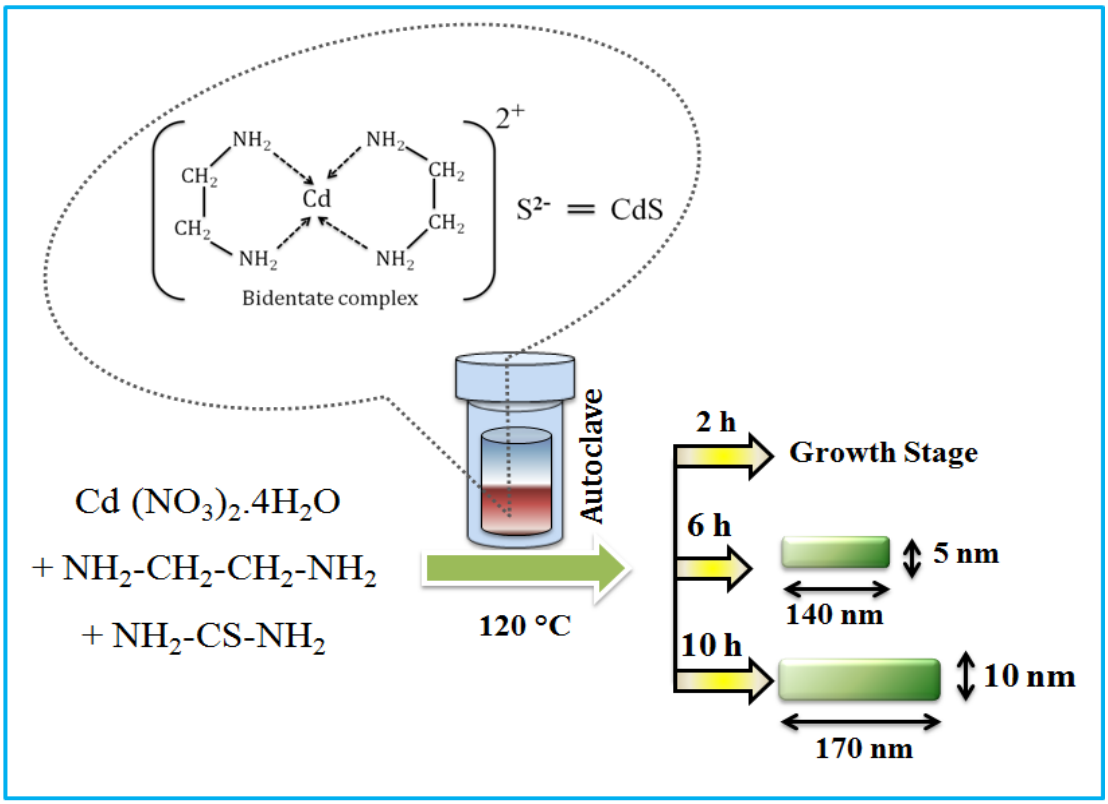

Fig. 1. Proposed reaction mechanism for the growth of CdS nanorods

Mechanism of CdS nanorods growth: The ethylenediamine nonaqueous solvent plays an important role in controlling the nucleation growth of CdS nanorod [3,4]. Initially, solvent molecule may act as a bidentate ligand to form a very stable Cd^{2+} complex (Fig. 1). The stability of the Cd^{2+}- en complex is believed to be decrease with the increase of the temperature above 120 $^{\circ}$C. At some high temperature, sulfur may coordinated to the above complex to form a one dimensional CdS-NR.

2.2.3 Synthesis of one dimensional (1 D) CdS nanowires

Two compartment cells were used for the synthesis of CdS nanowires (NW) and the alumina anodic membrane (AAM) of 50 nm fixed pore size was placed in between them [5] as shown in Fig. 2. An aqueous solutions of 50 ml $CdCl_2$ (0.01 M) with a few drops of 0.01M NH_4OH and 0.01 M Na_2S was allowed to diffuse for 2 h at room temperature. The template was finally removed by dissolving in 1 N NaOH solution, and the resulting sample was then washed several times with distilled water.

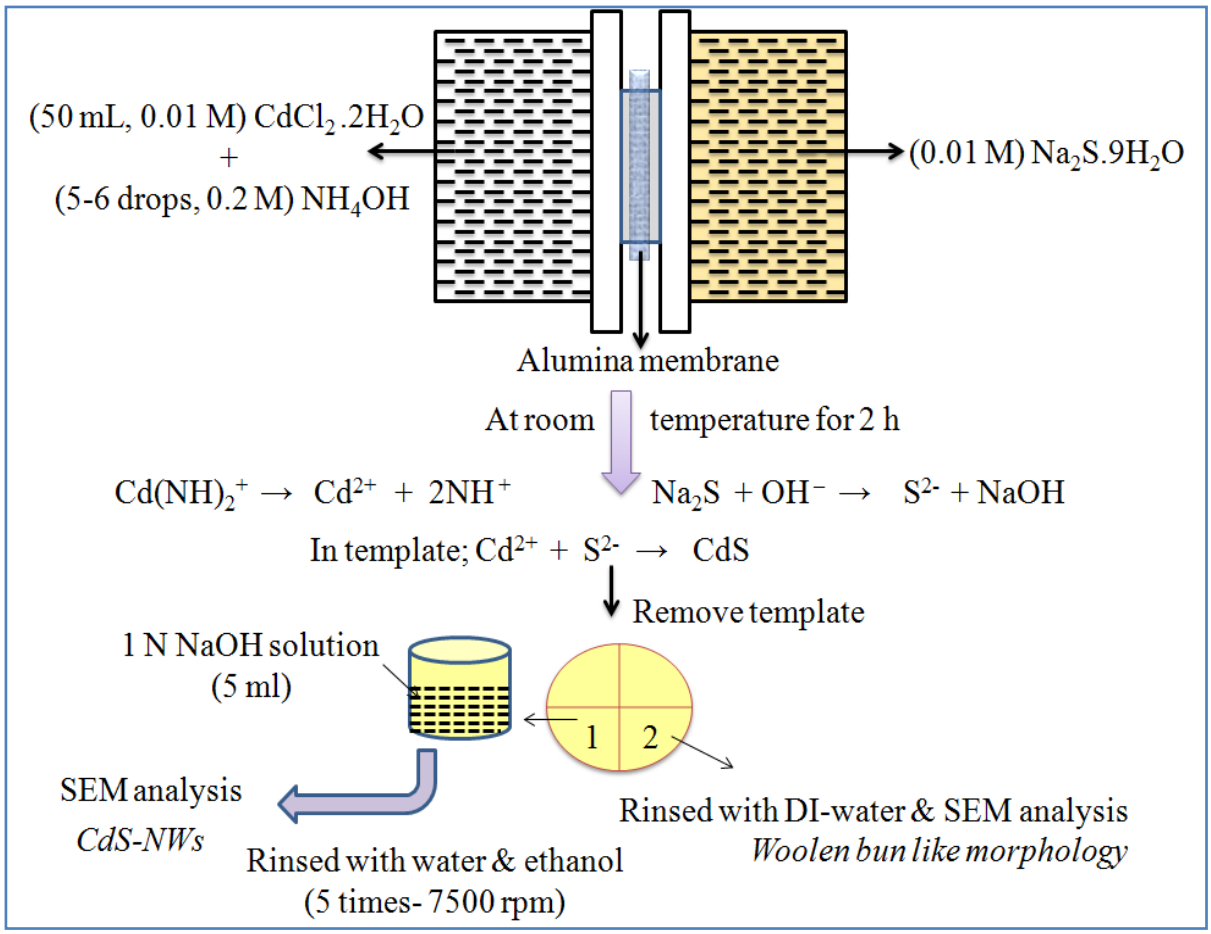

Fig. 2. Schematic illustration of two compartments cell for the template assisted synthesis of CdS nanowires.

2.2.4. Deposition of Au, Ag and Cu nanoparticles onto CdS nanorods

Photodeposition: As prepared 50 mg of CdS powder was suspended in 5 ml of an aqueous solution of isopropanol (50 vol%) in a test tube. An aqueous solution of metal salt ($HAuCl_4 .xH_2O$ or $AgNO_3$ or Cu $(NO_3)_2$) was injected (255 µl corresponds to 1 wt%) into above test tube. Test tube was sealed with a rubber septum and purged under argon (Ar) atmosphere for 15-20 min to remove

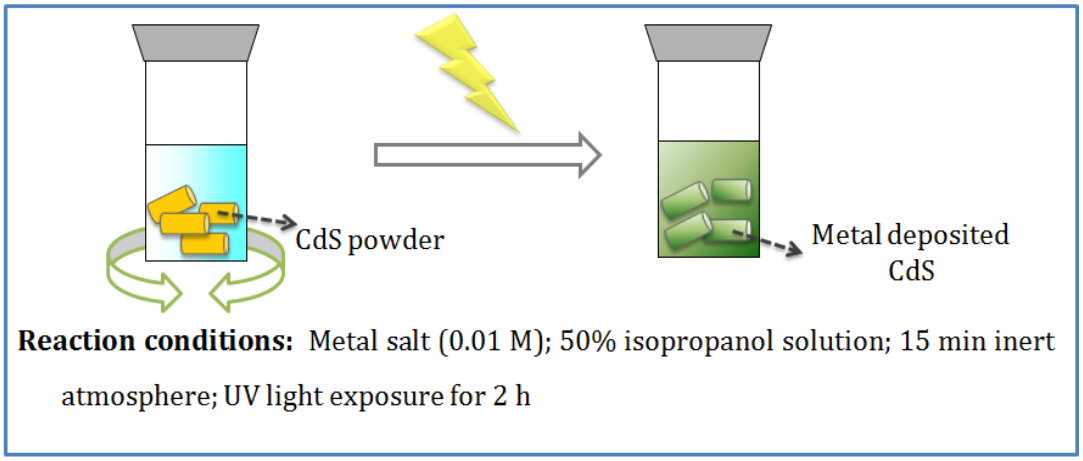

Fig. 3. Schematic illustration of photodeposition technique.

any traces of oxygen (Fig. 3). Resulting solution was photoirradiated by UV light (125 W Hg arc-10.4 mW/cm^2) under magnetic stirring for 2 h. The metal was reduced by photogenerated electrons on CdS surface. The resultant powder was washed repeatedly with distilled water and ethanol then dried in oven at 80 ºC for 30 min**.**

In-situ deposition: A solution of $HAuCl_4$ (depending upon wt%) in 10 ml of ethylenediamine was added to the solution containing the CdS-NR, and stirred for 15 min at room temperature. This solution was added to 20 ml of distilled water, which contain 0.9 mg of $NaBH_4$ and the immediately mixture turned dark gray which indicating that Au nanocrystals had formed. CdS nanocrystals were collected by centrifugation and washed with distilled water.

2.2.5. Preparation of silica coated CdS (SiO_2@CdS) nanorods

As synthesized CdS-NR were dispersed thoroughly in 250 ml toluene under constant stirring. Then, MPTMS (100–150 µl) was added to above solution to modify the CdS surface, followed by TEOS (0.7 mM) addition to increase the thickness of silica shell as reported *(chapter 1, ref. 68)* elsewhere. The solution was refluxed at 80 $^{\circ}$C for 2 h and meanwhile hydrolysis was carried out by drop wise addition of water, resulting in precipitation of SiO_2@CdS. Finally, sample was dried out by repeatedly washing with methanol.

2.2.6. Doping of Au^{3+}, Ag^{+} and Cu^{2+} into CdS-NR

Cd $(NO_3).4H_2O$ and corresponding metal salt (total sum of 0.4 mmol) and thiourea (0.8 mmol) dissolved in 10 ml of ethylenediamine and stirred for 2 h. The mixture was transferred into autoclave, which was maintained at 120 $^{\circ}$C for fixed 10 h. Thus obtained product was repeatedly washed with DI water and ethanol and dried to get metal doped CdS powder.

2.2.7. Synthesis of Au nanoparticles of different shapes

The Au nanoparticles of different sizes and shapes were synthesized by seed-mediated approach. *For the synthesis of Au nanospheres*, Au seeds [6] were first prepared by adding 250 µl (0.01 M) $HAuCl_4$ to 9.5 ml (0.1 M) cetyltrimethylammonium bromide (CTAB), followed by reduction with 600 µl (0.01 M) $NaBH_4$ solution under magnetic stirring for 2 min. The growth solution was prepared by treating a mixture of 500 µl (0.01 M) $HAuCl_4$, 9.5 ml (0.1 M) CTAB and 75 µl (0.01 M) $AgNO_3$ with 55 µl ascorbic acid (0.1 M). Then, 12 µl of above Au seed solution was introduced into the growth solution.

Au nanorod has been synthesized [7] by the same seed approach method at 70 °C. The Au nanoparticles were repeatedly washed with deionized water under four cycles of centrifugation at 8500 rpm for 10 min and then used for photocatalytic reactions.

2.2.8. Synthesis of spatial alignment of Au-CdS nanostructures

Direct assembly: Specific amount of Au NPs (10 µl) and CdS NPs (10 mg) having spherical as well as rod-like shape were mixed together with homogeneous stirring at room temperature to get desired product.

Impregnation*:* 10 µl of Au and 10 mg of CdS– NPs were dissolved in 2-3 ml of water, and the resulting solution was stirred for 2 h. Immediate after that solution was evaporated to dryness and was sintered at 200 ºC for additional 2 h to get the desired product.

2.2.9. Au^{3+} doped CdS/ TiO_2 solar cells preparation

Commercial available TiO_2 (350 mg; P25, Degussa) is mixed with 2 ml water, acetyl acetone (2 drops) and finally grind with mortar pestle for half an hour. TiO_2 paste is then spread on fluorine doped tin oxide (FTO) coated glass substrates using doctor blade method [8]. The film is annealed at 450 °C for 30 minutes in air. 5% Au^{3+} doped CdS (or pure CdS) powder (150 mg) is mixed with 2 ml water, acetyl acetone (2 drops) and 1 drop of Triton –X 100 and finally grind with mortar pestle for half an hour. The prepared paste of CdS sample is deposited on the TiO_2 substrate and annealed at 200 °C for 30 minutes. After sintering, the Au^{3+}-CdS/TiO_2 films are immersed in 0.3 mM of ruthenium dye solution for overnight.

The platinum coated counter electrode is prepared by dispersing a drop of 5 mM chloroplatinic acid hexahydrate (H_2PtCl_6) in isopropyl alcohol on separate FTO substrate and calcinating it at 450 °C for 15 min. A liquid electrolyte with redox couple I^-/I_3^- is sandwiched between both electrodes. A thin coating of parafilm is used as a spacer to avoid short circuiting between these two electrodes. A binder clip is fixed externally to maintain the mechanical grip of the cell without any further sealing, which finalized the assembly of the DSSC.

2.3. Characterization: Sophisticated instrumental techniques had been carried out to characterize nanomaterials and nanostructures to get an idea of their size, shape, crystal character, crystallite size, lattice constants, defects and surface area etc.

2.3.1 UV-vis spectrophotometer

UV-vis absorption is a very first method to acquire information about the size and the band gap of NPs, which is founded on the principle of absorption of light with suitable energy by sample molecules, which result in the promotion of an electron to a higher energy level. Analysis has been done on **Analytikjena Specord 205** instrument by taking 1mg/ ml sample powder in aqueous or acetone dispersion of the sample in 3.5 ml quartz cuvette within the range of 190−1100 nm.

Bandgap calculations of as prepared samples were done by using Tauc equation [9,10],

$$\alpha h\nu = A(h\nu - E_g)^n$$

where α is the absorption coefficient of the material, which represents the absorption ability of a material for a certain wavelength; h is the Planck constant; ν is the frequency of light; A is a constant, which depends on temperature, photo energy and phonon energy; E_g is the band gap; the exponent n is a characteristic of the type of electrons transition process (n = 1/2 for a direct allowed transition & n = 2 for an indirect allowed transition process). As CdS is direct band gap semiconductor, hence the band gap was determined by extrapolating the linear portion of the plot of $(\alpha h\nu)^2$ versus hν.

2.3.2 UV-vis diffuse reflectance Spectrophotometer

Diffuse reflectance occurs when the surface reflects light in many different directions, giving the surface a dull finish. The absorbance of solid powder was carried on **Avantes Diffuse reflectance spectrophotometer.** Sample (2-5 mg) was taken on a glass slide and and the light source probe was placed over the sample to record its absorbance/ reflectance spectra by using $BaSO_4$ as a reference.

2.3.3 Photoluminescence (PL) measurement

Photoluminescence technique deals with the transitions from the excited state to the ground state, complementary to UV-vis spectroscopy. **Perkin-Elmer LS55** spectrofluorimeter was used to study the possible defect and emission in as-synthesized materials. For PL analysis, 1mg/ml acetone dispersion of as-prepared samples were photoexcited at 380 nm by using a slit width of 2.5: 5 with an average scan rate of 4 times.

2.3.4 Time resolved spectroscopy

Time resolved spectroscopy is the study of dynamic processes in materials. **Tektronix TDS 1012 oscilloscope** was used to record fluorescence decay curves by preparing a thick paste of CdS powder (~50 mg) with a few drops of acetone to make it as a solid mass. Thereafter, stub having solid mass was suspended vertically for laser pulsation (excited at 490 nm) and an average lifetime was recorded and calculated using following equation [11,12];

$$\tau_{av} = (a_1\tau_1 + a_2\tau_2)/ a_1 + a_2$$

2.3.5 Scanning electron microscopy (SEM)

JSM-7600F (0.1–30 kV) SEM instrument was used for surface morphology analysis of sample by treated powder with ultrathin coating of electrically conducting Au material, which was deposited on the sample by low-vacuum sputter coating. After that, conducting material was mounted rigidly on a specimen holder called a specimen stub for surface analysis.

2.3.6 Energy Dispersive X-ray (EDX) spectrophotometer

EDX analysis was carried on **JEOL JSM-6510LB**. At least three analyses at different spots were performed for each sample in order to obtain an average value.

2.3.7 Transmission electron microscopy (TEM)

The specimens were prepared by depositing a drop of a dilute methanol or ethanol dispersion of nanoparticles on carbon-coated copper grids and allowing the solvent to evaporate rapidly. Low magnification **TEM (Hitachi 7500 model**) was performed at operating voltages of 20-200 kV with 2.4 A˚ resolutions and High Magnification-TEM (HR-TEM) was carried at with resolution 2 A˚ operating at voltage 120 kV **on JEOL, JEM 2100.**

2.3.8 X-ray diffraction analysis

Structural and phase identification was carried out with Cu-Kα (k = 1.54060 A°) radiation operated at 45 kV within the range of 10-90° on **PANalytical X'Pert PRO**. XRD samples were prepared by grinding dried CdS powder in a pestle and mortar to form fine powders. The average size of the particles was calculated using the Scherrer's equation [13];

$$\mathbf{L = k\lambda/\beta \cos \theta,}$$

where L is the average particle size, k is a constant of 0.9, λ is the wavelength of X-ray (1.5418 A°), β is the Full-Widths at Half-maximum (FWHM) of the (hkl) diffraction peak and θ is the Bragg angle.

2.3.9 Surface Area Analysis

BET surface area analysis was carried out in order to measure the surface area of the solids. The analysis of the porous surface was carried out by N_2 adsorption/desorption techniques at 77 K. Adsorption isotherms were determined using a **Smartsorb 92/93** instrument where 100 mg of samples are regenerated at 150 °C for 1 h.

2.3.10 Current-voltage (I-V) characteristic

I-V measurements were carried out using an 8 point-probe measuring box positioned within a hermetically sealed device holder **KEITHLEY source meter,** 4200-SCS, attached to ZYVEX S100 Nanomanipulator.

2.3.11 High Performance Liquid chromatography (HPLC) was carried out by using **Agilent, 1120 Compact LC technologies** with C-18 column (250 mm × 4.5 mm). The mobile phase used for the analysis was methanol and water in ratio of 65:35 and 70:30 with a flow rate of 1 ml/min at 220 and 254 nm wavelengths for the detection of *p*-nitrophenol and *m*-dinitrobenzene reduction products, respectively.

***2.3.12 Gas chromatography-mass spectroscopy (GC-MS*)** was carried out on **Shimadzu, GC-2010 and GC-MS-QP 2010 plus** with RTX-5Sil-MS column (30 mm × 0.25 mm × 0.25 µm) to confirm the products/intermediates. As obtained aqueous solution of substrate after final UV-light exposure was centrifuged, filtered through cellulose filter (0.22 µm) and then extracted three times with dichloromethane. Residue thus obtained was re-dissolved in methanol. Helium was used as a carrier gas with a flow of 1ml/min through capillary column. Injector was maintained at 240 $^{\circ}$C. Oven was programmed at 60 $^{\circ}$C to 300 $^{\circ}$C @ 6 $^{\circ}$C/min rise of temperature.

2.3.13 Gas chromatography (GC)

The CO_2 evolution was determined by injecting 1 ml of the gaseous mixture from the reaction vessel into the gas chromatography using Propak-Q column, **NUCON-5765** (30 mm × 0.32 mm × 12.00 µm) with nitrogen as carrier gas (30 ml/min) and Thermal Conductivity Detector (TCD). Column oven was maintained at 40 $^{\circ}$C while injector and detector were at 70 and 80 $^{\circ}$C, respectively.

2.3.14. Magnetic susceptibility is determined by Goy's method by packing the (dry) sample carefully into the glass tubes having sample length in the range 2.0 - 3.0 cm. Add the sample to the tube in small amounts, tapping the base of the tube on the wooden bench a number of times between additions to shake the solid down and ensure even packing. After that, mass (m) and length (L) of the sample was recorded and magnetic susceptibility.

2.4. Photocatalytic reaction setups

2.4.1. Photocatalytic reactor with Hg (UV) light source

It is composed of a UV light source (125 W) of low pressure mercury vapor lamp that emit mainly at 254 nm. Low-pressure lamps normally operate at temperature range from 40-50 $^{\circ}$C and emit two wavelengths at 253.7 nm and 184.9 nm. The emission at 185 nm is of no use, as it is absorbed by

the quartz which surrounds the lamp; therefore the only interesting line emission is 253.7 nm and for this cause these lamps are consider to be monochromatic.

The Hg lamp (125 W; intensity 10.4 mW/cm^2) connected to power cords was set inside a water-jacketed quartz tube as shown in Fig. 4. A continuous flow of cold water was circulating in this outer jacket to make sure it cool over the longer time. Maximum 5 ml of reaction sample was taken in 15 ml capacity test tube that is placed at a distance of 2-3 cm from light source under magnetic stirrer for homogeneous stirring. The distance between magnetic stirrer and lamp was minimized to get optimum flux. The whole set up was placed in a wooden box to prevent the UV exposure as a safety purpose.

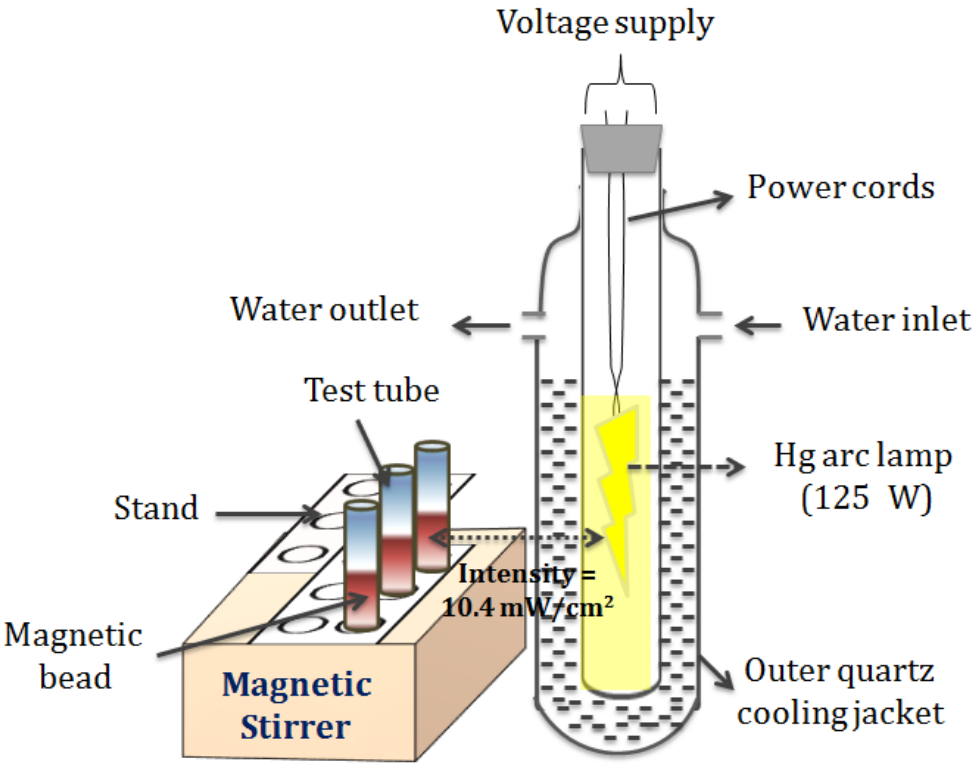

Fig. 4. Pictorial design of the UV photochemical reactor.

2.4.2. Sunlight as a visible light source

The experiment was carried out by homogeneous stirring of 10 ml of substrate solution in a 25 ml capacity beaker (exposed area = 12.56 cm^2) with 20 mg catalyst. The whole setup was placed under the direct exposure of sunlight at the terrace between 12.00 pm – 4.00 pm times. Sunlight intensity (flux) was measured by using Lux meter. The reaction samples are analysed with UV-visible spectrophotometer for different time intervals.

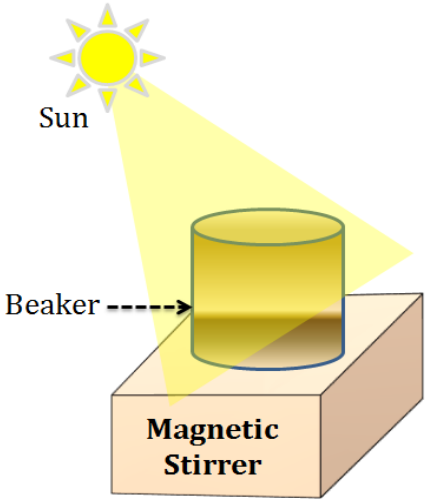

Fig. 4. Pictorial design of experimental setup under direct sunlight.

2.5. References

[1] T. Torimoto. J.P. Reyes, K. Iwasaki, B. Pal, T. Shibayama, K. Sugawara, H. Takahashi, B. Ohtani, J. Am. Chem. Soc. 125 (2003) 316–317.

[2] J. Yang, J.H. Zeng, S.H. Yu, L. Yang, G.E. Zhou, Y.T. Qian, Chem. Mater. 12 (2000) 3259–3263.

[3] S.H. Yu, J. Yang, Z.H. Han, Y. Zhou, R.Y. Yang, Y.T. Qian, Y.H. Zhang, J. Mater. Chem. 9 (1999) 1283–1287.

[4] Y.D. Li, H.W. Liao, Y. Ding, Y.T. Qian, L. Yang, G.E. Zhou, Chem. Mater. 10 (1998) 2301-2303.

[5] F. Zhang, S.S. Wong, Chem. Mater. 21 (2009) 4541–4554.

[6] J. Kimling, M. Maier, B. Okenve, V. Kotaidis, H. Ballot, A. Plech, J. Phys. Chem. B 110 (2006) 15700–15707.

[7] X. Huang, S. Neretina, M.A. El-Sayed, Adv. Mater. 21 (2009) 4880–4910.

[8] G. Katsaros, T. Stergiopoulos, I.M. Arabatzis, K.G. Papadokostaki, P. Falaras, J. Photochem. Photobiol., A 149 (2002) 191–198.

[9] Y.F. Zhu, J. Zhang, L. Xu, Y. Guo, X.P. Wang, R.G. Du, C.J. Lin, Phys. Chem. Chem. Phys. 15 (2013) 4041-8.

[10] B. Subramanian, C. Sanjeeviraja, M. Jayachandran, J. Cryst. Growth 234 (2002) 421-426.

[11] W. Wu, H. Ye, X. Ruan, Nanotechnology 21 (2010) 1–5.

[12] J. Li, J. Xia, Phys. Rev. B 62 (2000) 12613–12616

[13] N. Saravanan, G.B. Teh, S.Y.P. Yap, K.M. Cheong, J. Mater Sci: Mater Electron 19 (2008) 1206-1208

Chapter 3: Enhanced Photocatalytic Activity of Coinage Metal-Cadmium Sulfide Nanorod Composites under Sun Light Irradiation

3.1. Introduction

The metal and semiconductor nanomaterials (1−100 nm) exhibit unique optoelectronic, mechanical, antibacterial and photocatalytic properties which differ from those of their bulk behavior [1-9]. Numerous studies have been concentrated on the properties of nanomaterials that affect their catalytic performance such as their size, interaction with their support, and their oxidation state [10-12]. In contrary to this, much less research elucidates the influential role played by the NP shape [13-15]. Tuning the shape result in alteration of the arrangement of atoms, and thereby confinement of electrons and many surface related parameters such as surface area, surface to volume ratio, and surface exposure etc. Fascinatingly, different reactivity's and selectivity's may be expected on distinct facets of NPs with different shapes [15]. For an example, Ag-NPs with cube like morphology has been found to be 14 times more active for the oxidation of styrene than its plates like morphology, and 4 times more active than its spherical form [14]. Thus, various semiconductors such as ZnO, TiO_2, ZnS, CdS, WO_3 etc. and metallic nanoparticles such as Au, Ag, Cu, Pt, Pd, Rh etc. with different geometries have been become a part of a recent study in a variety of applications.

CdS, a well-known visible-light-sensitive material with direct band gap of 2.42 eV has been widely studied after TiO_2 and ZnO material as its physical properties are very close to ZnO, including crystal structures, lattice constants, and so on [16]. In particular, CdS-NR has found some special applications [4-6] in photoelectric conversion in solar cells, light emitting diodes for flat panel displays and H_2 evolutions etc. [17-19]. It is well known that the photocatalytic efficiency of CdS is seriously restricted by the immediate recombination of e^-/h^+ pairs and its photocorrosion during the photochemical reaction [20,21]. Hence, deposition of noble metal (M) co-catalysts onto CdS surface is believed to accelerate the photochemical reaction rate by preventing the recombination of photoexcited electron-hole pairs [22,23]. Intriguing optical properties of Au, Ag and Cu NPs originating from surface plasmon absorption in the visible range, make them a promising candidate to couple with CdS [Chapter 1, ref. 47-52] nanostructures. As a result, nanostructures composed of mentioned metals and CdS would show

much more interesting properties including optical and detoxification of water from a number of organic pollutants.

In the present study, *salicylic acid (SA)* was chosen as a ***model*** organic compound/pollutant to study the possible degradation trends and kinetics with bare and M-CdS (M= Au, Ag and Cu) composites because of following reasons. Firstly, industrial effluents contain a number of important organic compounds such as dyes, phenols, aromatic acids. Salicylic acid, being an important organic compound has been identified as a water pollutant which arises from a number of resources including cosmetic, paper milling and pharmaceutical industries [24]. Secondly, it is insignificant reacting with molecular ozone, hence readily degraded by generating hydroxyl radicals and thirdly, salicylic acid formed chelating complex with CdS, which resulted in better adsorption and hence degradation. Interestingly, the effect of various parameters such as catalyst morphology, pH, catalyst amount, concentration of salicylic acid, nature of metal as co-catalyst under both UV (10.4 mW/cm^2) and sunlight (40-50 mW/cm^2) irradiations have been studied.

3.2. Experimental section

3.2.1. Synthesis of CdS nanospheres and nanorods

Bare CdS-NS was prepared as discussed in *chapter 2, section- 2.2.1*. CdS-NR was synthesized as mentioned in *chapter 2, section- 2.2.2*.

3.2.2. Deposition of Au, Ag and Cu NPs onto CdS-NR

1 wt% Au, Ag and Cu was deposited onto CdS-NR surface by photodeposition and in-situ deposition techniques as mentioned in *section- 2.2.4 of chapter 2*.

3.2.3. Photocatalytic reactions

Photocatalytic activity was tested for the oxidation of 5 ml of 0.5 mM salicylic acid with 10 mg of bare and M deposited CdS catalysts in a test tube under UV light irradiations with intensity 10.4 mW/cm^2 for different time intervals. The experiment under sunlight (intensity, 40-50 mW/cm^2) was carried out by homogeneous stirring of 10 ml of 0.5 mM salicylic acid solution in a 25 ml capacity beaker with 20 mg catalyst for different time periods. The reaction aliquots were taken from the test tube and beaker at regular intervals of time. The reaction sample was analyzed by UV–vis spectrophotometer (λ_{max} = 298 nm for salicylic acid) after filtration with 0.22 μm cellulose filter. The photodegradation efficiency of salicylic acid was calculated by following equation,

$$\textbf{Degradation (\%)} = [(A_0 - A_t) / A_0] \times 100$$

Where A_0 is the initial absorbance and A_t is the absorbance at certain time t.

3.2.4. Characterization

As prepared CdS and metal loaded-CdS nanostructures were characterized by UV-vis absorption, diffuse reflectance and photoluminescence spectrophotometer. Morphological study of size and shape analysis was done by TEM. BET surface area was measured by N_2 adsorption technique. X-ray diffraction study was carried out for phase identifications. The amount of CO_2 produced on mineralization of salicylic acid was measured by GC with a TCD as a detector. All techniques are mentioned in detailed in *chapter 2, section 2.3.*

3.3. Results and discussion

3.3.1. Optical study

Fig. 1 showed the Diffused absorbance and fluorescence emission spectra of CdS-NS and NR with corresponding band gaps. The absorption onset (Fig. 1a) of CdS-NR & NS appears at 515−525 nm. It is observed from the spectrum that absorption onset edge found to be at lower wavelengths (blue shift) than bulk CdS, indicating the quantum confinement effect in CdS-NS and NR. The band gap of CdS was determined from the Tauc plot by extrapolating the linear portion of the plot of $(\alpha h\nu)^2$ versus hν. The band gap of CdS nanospheres and nanorods was calculated to be 2.46 and 2.51 eV.

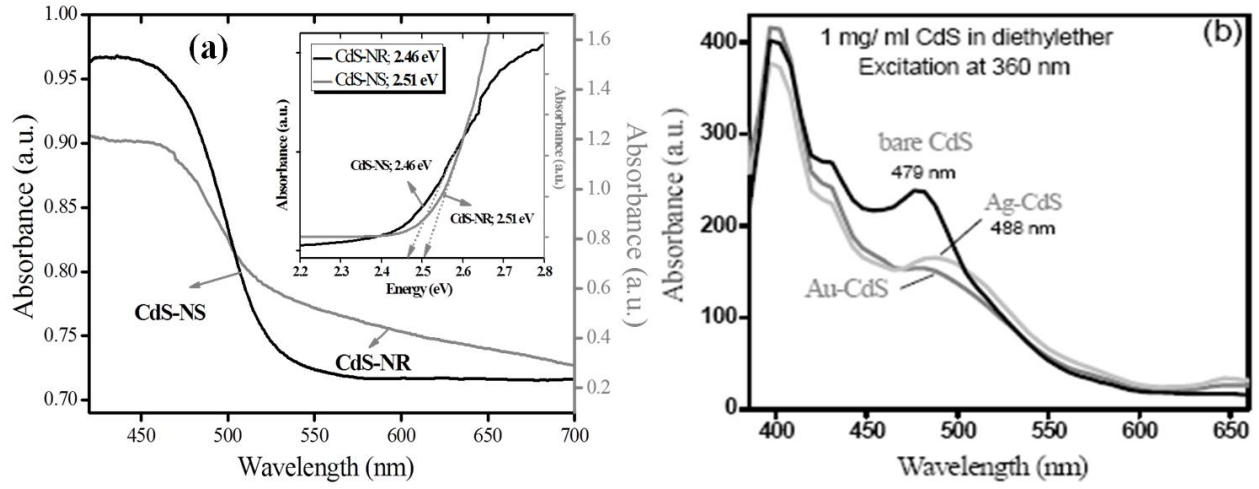

Fig. 1. (a) Diffuse reflectance spectra with corresponding bandgap in inset, and (b) fluorescence emission spectra of bare and Au & Ag photodeposited CdS-NR.

Photoluminescence (PL) spectra have been performed to investigate the luminescence properties of CdS nanostructures at excitation (λ_{ext}) = 360 nm. It is observed that PL spectra (Fig. 1b) of CdS-NR consist of a band located at 479 nm and very small hump at 520 nm due to band edge

emission and trap luminescence at the surface trap sites. This green emission band was associated with emission due to electronic transition from CB to acceptor level due to interstitial sulfur ions. Moreover, photodeposition of 1 wt% Au and Ag onto CdS-NR dramatically quenched the fluorescence emission due to the prevention of electron-hole recombination owing to rapid electron capture by the deposited Au and Ag NPs onto CdS surface. Hence, an electron-transfer from the CdS to metal NPs reduced the surface defects & trap sites and thereby changes the optical properties.

3.3.2. Morphological study

TEM images in Fig. 2a showed the monodisperse spherical particles of CdS within range of 10−12 nm. Fig. 2 (b-c) evidencing the rod-like shape of CdS-NPs. The average length and width of NR has been found to be 116 nm and 5.6 nm which corresponding to aspect ratio 21 (average size was calculated manually by considering individual 20 particles).

Fig. 2 (d-e) representing the 1 wt% Au deposited CdS-NR that are prepared by the in-situ

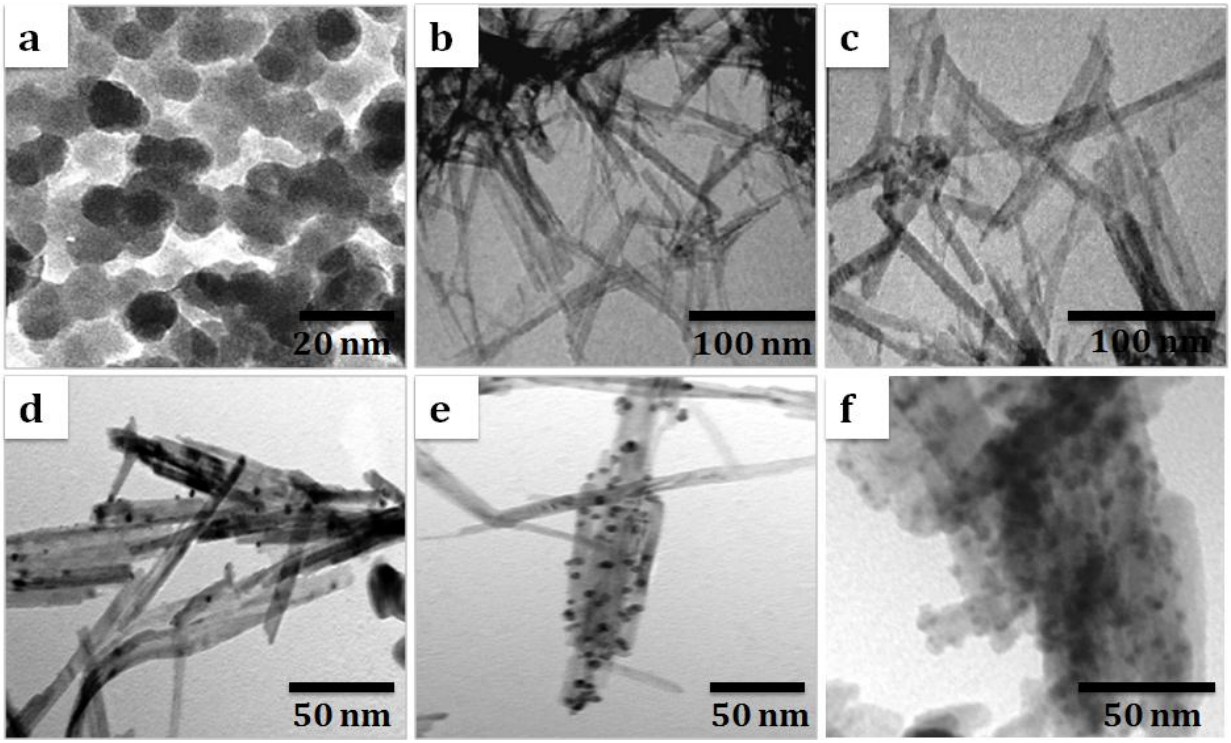

Fig. 2. TEM images of CdS (a) nanospheres, (b-c) nanorods, (d-e) 1 wt% Au (~3.5 nm) deposited-NR by $NaBH_4$ reduction and (f) 1 wt% Au (~2 nm) photodeposited NR.

approach by the reduction of Au^{+3} ions by reducing agent $NaBH_4$. Uniform spherical Au nanodeposits (black) onto CdS-NR of average size 3.5 nm are clearly noticed. Small Au-NPs of average size ~2 nm (black spot) are deposited throughout the CdS-NR surfaces that are

aggregated on drying process after photodeposition (Fig. 2f). The surface area and surface to volume ratio of the CdS-NR are measured to be ~81 m^2/g and 0.41 nm^{-1} {surface area/ volume; $(2\pi r^2 + 2\pi rh)/ (\pi r^2 h)$} respectively, which is quite high as compared to conventional CdS-NS and bulk materials.

3.3.3. Photodegradation of salicylic acid

3.3.3.1. Effect of catalyst shape

Fig. 3 displayed the changes in absorption spectra of (0.5 mM) SA during its photocatalytic activity (PCA) by CdS-NS and NR under UV light irradiations with intensity 10.4 mW/cm^2 (125 W Hg arc-lamp).

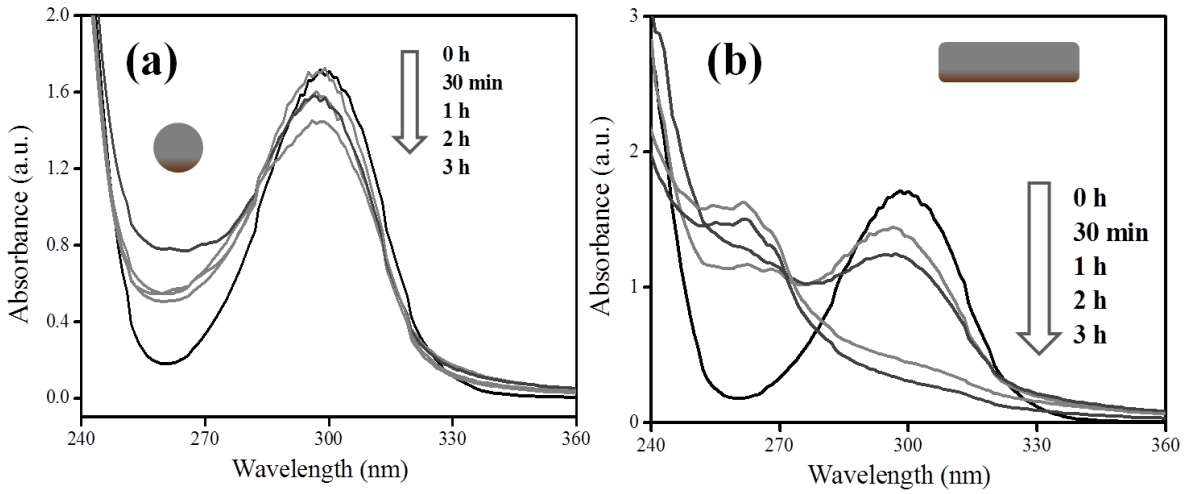

Fig. 3. Change in absorbance spectra of 0.5 mM salicylic acid by CdS (a) nanospheres, (b) nanorods under UV light irradiations for different time periods.

It is demonstrating here that geometrical effect from NS to NR led to a remarkable change (>50%) in the salicylic acid degradation trend. Even after 3 h of UV light exposure CdS-NS exhibited insignificant changes in the absorbance of SA. In contrast, CdS-NR almost photooxidized 0.5 mM SA within 3 h of UV light irradiations. Notably, these results highlight the importance of catalyst shape additionally to its size. Different crystallographic facets, proportion of surface atoms, surface area, delocalization of charge carriers and their relaxation lifetime expected to be changed by tuning the shape [14,15] from NS to NR, which have a pronounced effect on reactions that occur on the surface such as adsorption and catalysis. Higher surface area (~81 m^2/g) and crystallographic growth along {002} plane in CdS-NR resulted in long–term photoseparation of charge carriers along elongated c-axis.

3.3.3.2. Effect of solution pH

Photodegradation of SA was studied out at different pH conditions (Fig. 4a) by adjusting with HCl and NaOH.

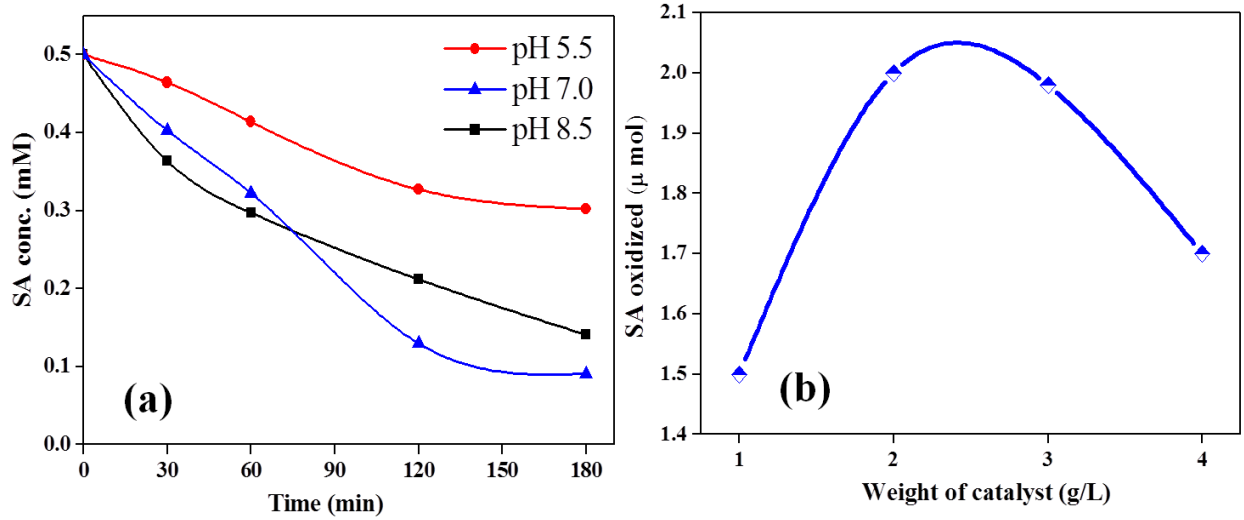

Fig. 4. (a) Effect of (a) pH and (b) catalyst loading on the photocatalytic degradation of salicylic acid.

It has been noted that optimal adsorption and hence degradation of SA was achieved at neutral pH (7.0). Salicylic acid was observed to be about 82% degraded at pH 7.0 after 180 min of UV light irradiations *(reaction conditions: SA = 0.5 mM; catalyst = CdS-NR (2.0 g/L); incident wavelength = 254 nm; absorbance measured at 298 nm)*. On the other side, the increase and decrease in pH to 8.5 and 5.5, resulted in 72% and 40% degradation. Our results are consistent with reported by Rao et al. for the decomposition of SA by ZnO [25], who suggested that salicylic acid exists as its anion when the pH > p*K*a (p*K*a = 2.97). As expected, the electrostatic attraction between the catalyst and salicylic acid increases the adsorption and photodegradation rate.

3.3.3.3. Effect of catalyst amount

Fig. 4b shows the effect of variation in amount of CdS-NR on the photodegradation of the SA in the range of 1.0–4.0 g/L *(reaction conditions: SA = 0.5 mM; pH = 7.0; reaction time = 180 min; incident wavelength = 254 nm; absorbance measured at 298 nm).* A noteworthy increase in the amount of SA oxidized was found with an increase in the catalyst weight from 1.0 to 2.0 g/L after 180 min of UV light exposure. Thereafter, increase in catalyst amount resulted in the nearly comparable reaction rate. In contrary, loading of CdS-NR catalyst above 3.0 g/L results in a reduction of degradation of salicylic acid due to decrease in UV light penetration because of

excess catalyst in the solution.

3.3.3.4. Effect of concentration

The possible photodegradation trend of SA was analyzed by C/C_o plots at different initial

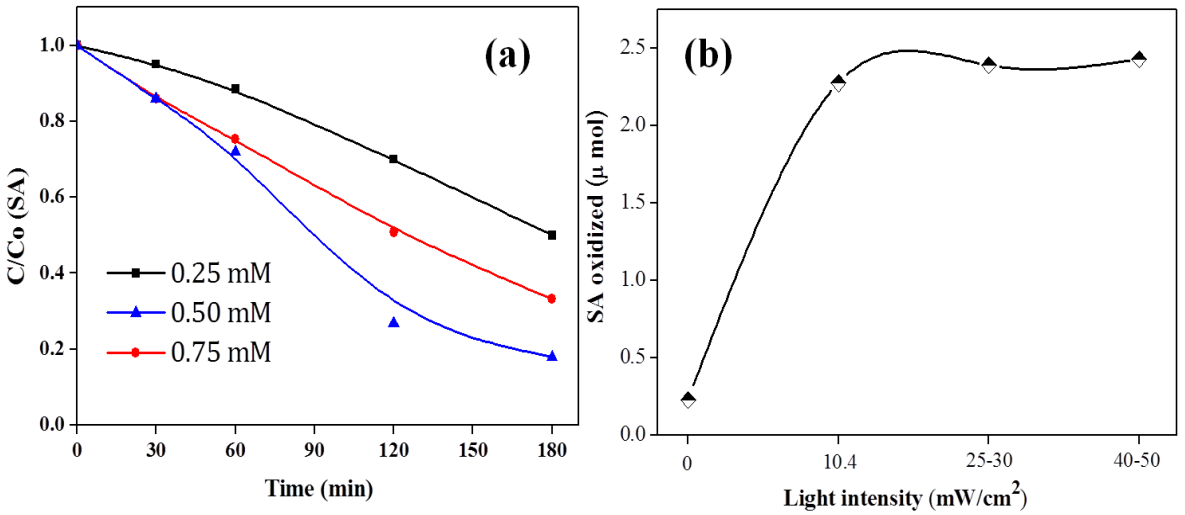

Fig 5. (a) Effect of (a) concentration and (b) light intensity on the photocatalytic degradation of salicylic acid

concentrations (0.25 to 0.75 mM) as shown in Fig. 5a *(reaction conditions: catalyst = CdS-NR (2.0 g/L); pH = 7.0; incident wavelength = 254 nm; absorbance measured at 298 nm).* With an increase in concentration from 0.25 to 0.5 mM, the rate of photodegradation of salicylic acid was found to be significantly increased. But a further increase in concentration to 0.75 mM resulted in a decrease in the SA degradation. This can be explained on the basis of their different adsorption rate at different concentrations. The more and more number of molecules of SA are adsorbed on the surface of CdS as initial concentration increases. This is due to large numbers of active sites available for the adsorption, which results in higher generation of hydroxyl radicals, for photooxidation of SA. On further, increase in concentration of the SA solution to 0.75 mM, extra number of SA molecules beyond their adsorption interrupted the photons that are reaching at the catalyst surface; consequently the degradation rate is reduced.

3.3.3.5. Effect of light intensity

Fig. 5b shows the effect of light intensity on the reaction rate of SA *(reaction conditions: catalyst = CdS-NR (2.0 g/L); pH = 7.0; Concentration = 0.5 mM; absorbance measured at 298 nm).* It has been noted that without irradiations of light or only in dark, insignificant change in reaction rate has been observed. Under UV light irradiations of 10.4 mW/cm^2 intensity, the rate of

formation of hydroxyl radicals increases, which result in the overall reaction rate of SA. As expected under similar conditions but under direct sunlight with intensity of 25-30 mW/cm^2 (*normal sunny day*) the number of oxidized moles of salicylic acid increased indicating the well matched band gap of CdS (2.45 eV) with the visible region of solar spectrum. The significant difference in the production of hydroxyl radicals and hence the reaction rate has been observed further under similar conditions but on an *intense day* having intensity 40-50 mW/cm^2.

3.3.3.6. Effect of nature of metal deposition

The Au deposition greatly improved the photocatalytic activity of CdS-NR as evident from the rapid decrease in absorbance of SA with irradiation time. The Au-CdS composites took 2 h light exposure to completely degrade 0.5 mM SA, in comparison to less reactive bare CdS-NR under identical conditions. In the absorption spectra, some low intense absorption bands at 250−270 nm are observed due to the formation of hydroxylated products that are gradually disappearing due to complete degradation of SA to CO_2 & H_2O by Au-CdS composites within 2 h sun exposure.

The photodegradation rate of SA displayed by CdS-NS, NR and Au deposited CdS-NR both under direct sunlight (40-50 mW/cm^2) are shown in Fig. 6a. It is observed that CdS-NS (~10 nm)

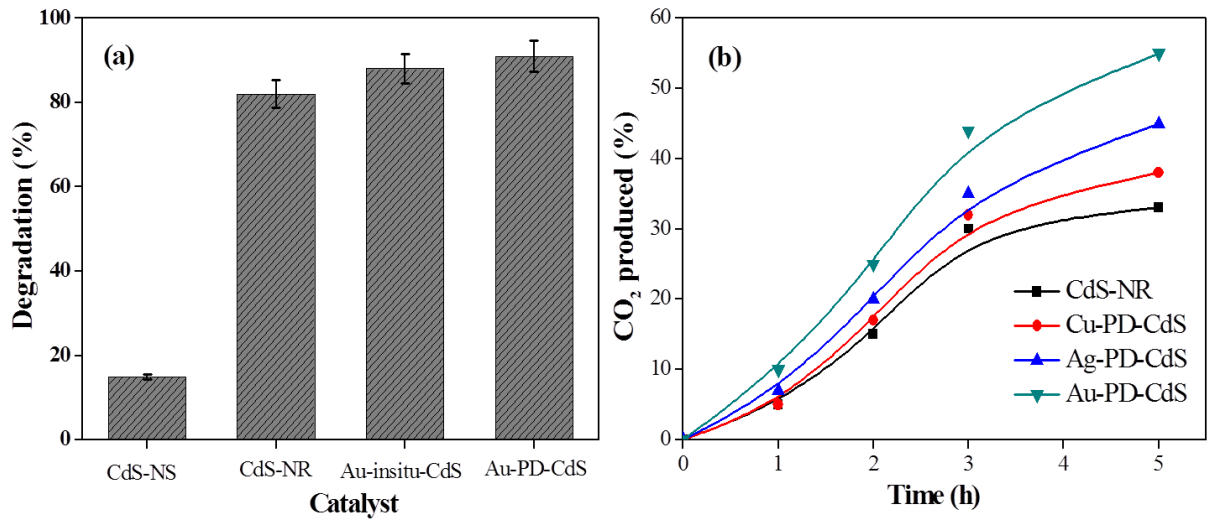

Fig. 6. (a) Histogram displaying degradation% of SA by various CdS and Au-CdS catalysts under 3 h of sunlight irradiations, and (b) corresponding production of CO_2 at different time intervals.

exhibits negligible photocatalytic activity as compared NR. Moreover, two different sizes of Au co-catalysts, namely, ~3.5 nm & 2 nm depositions onto CdS-NR (namely Au-in-situ-CdS &

Au-PD-CdS) highly improved the photocatalytic rate of SA in different extent as a function of the Au co-catalyst sizes. The photodeposited Au nanodeposits of smaller size (2 nm) imparted higher co-catalytic activity to CdS-NR than larger size (3.5 nm) of Au deposition by $NaBH_4$ reduction.

Fig. 6b showed the production of CO_2 by 1 wt% Au, Ag and Cu photodeposited CdS-NR for the photodegradation of SA at various time intervals. In all cases of metal photodeposition on to CdS-NR, photoactivity found to be enhanced as compared to bare CdS-NR. Au and Ag photodeposited CdS-NR was found to be highly efficient in terms of decomposition of SA and CO_2 production in comparison to less activity of Cu deposition. This enhanced rate of SA by M-CdS-NR can be explained on the basis of electrons capture by metal deposits from irradiated CdS surface that prevented the recombination of photoexcited electron-hole pairs and thereby, increased the degradation of SA by strongly oxidizing holes. The photo energetics and electronic properties of metal co-catalysts play a vital role in transferring the photoexcited charge carrier at the metal-CdS nanojunctions formed by the small metal NPs deposition whose Fermi energy is size dependent.

The dissimilar PCA of Au, Ag and Cu loaded CdS can be attributed to the variation in co-catalytic activity of the respective metals as a function of their Fermi energy level equilibrium, work functions, reduction potentials and electron affinities which controlling the electron accepting capacity from photoexcited CdS to surface bound metal deposits *(chapter 1, Fig. 2).* In Au–CdS nanocrystals; Au core can serve as an effective electron scavenger for CdS shell due to its lower Fermi energetic level (+0.5 V versus NHE) than the conduction band of CdS (−1.0 V versus NHE). As a result, the Fermi level equilibrium takes place quickly and rapid electron transfer from CdS to Au-NPs even than for both Ag and Cu that are located at around +0.15 V versus NHE lower in energy states [26-28] than the conduction bands of bulk CdS (-1.0 V versus NHE). Moreover, due to large variation in percentage of surface active atoms and surface-to-volume ratio of two unlike sizes of Au co-catalysts, might have altered the kinetics of electron transfer process at the Au-CdS interface resulted in the difference in PCA between two Au (3.5 & 2 nm)-CdS-NR composites as shown in Fig. 6a.

3.3.3.7. Kinetics study: The photocatalytic degradation of salicylic acid obeyed first order kinetics as shown in Fig. 7. A linear graph of 1/r versus $1/C_o$ is plot by using the modified form of Langmuir–Hinshelwood kinetics.

$$r = \frac{k_1 k_2 C_o}{1 + k_1 C_o}$$

$$\frac{1}{r} = \frac{1}{k_1 k_2 C_o} + \frac{1}{k_2}$$

where k_1, k_2 and C_o are adsorption constant, specific rate constant and initial concentration of salicylic acid respectively.

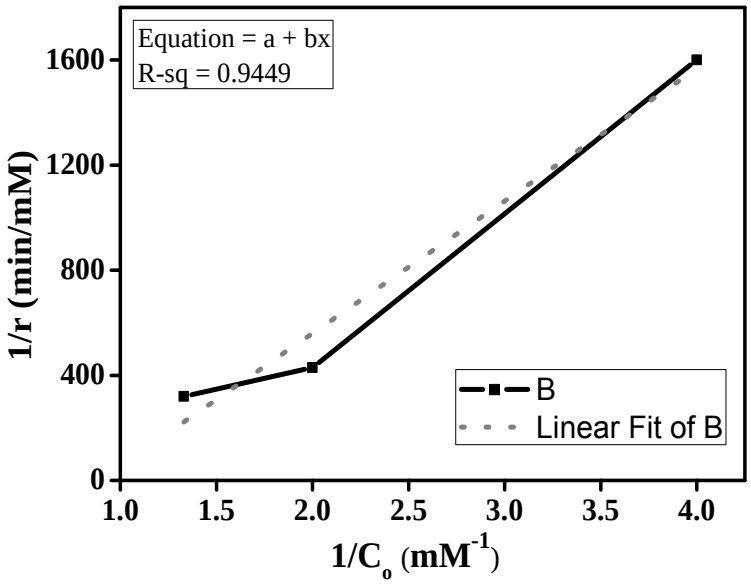

Fig. 7. Plot of 1/r versus 1/Co for observed change in SA.

Thus it is demonstrated that fluctuation of size, shape and nature of metal co-catalysts, pH and concentration of solution, catalyst loading, and light intensity could be beneficial in designing highly active photocatalyst for optimum reaction conditions for complete detoxification of organic pollutants.

3.4. References

[1] L. Brus, Acc. Chem. Res. 41 (2008) 1742–1749.

[2] J. Jiang, K. Bosnick, M. Maillard, L. Brus, L. J. Phys. Chem. B 107 (2003) 9964–9972.

[3] A.H. Gore, U.S. Mote, S.S. Tele, P.V. Anbhule, M.C. Rath, S.R. Patil, Analyst 136 (2011) 2606-2612

[4] S. Nie, S.R. Emory, Science 275 (1997) 1102–1106.

[5] M.B. Thathagar, J. Beckers, G. Rothenberg, Adv. Synth. Catal. 345 (2003) 979-985.

[6] L.D. Pachon, M.B. Thathagar, F. Harti, G. Rothenberg, Phys. Chem. Chem. Phys. 8 (2006) 151-157.

[7] E.J. Park, J. Yi, Y. Kim, K. Choi, K. Park, Toxicol. in Vitro. 24 (2010) 872-878.

[8] S. Kim, J.E. Choi, J. Choi, K.H. Chung, K. Park, J. Yi, D.Y. Ryu, Toxicol. in Vitro. 23 (2009) 1076-1084.

[9] E.J, Park, J. Yi, K.H. Chung , D.Y. Ryu, J. Choi, K. Park, Toxicol. Lett. 180 (2008) 222-229.

[10] B. Roldan Cuenya, Thin Solid Films 518 (2010) 3127–3150.

[11] C.T. Campbell, Science 306 (2004) 234–235.

[12] P.L. Hansen, J.B. Wagner, S. Helveg, J. R. Rostrup-Nielsen, B.S. Clausen, H. Topsoe, Science 295 (2002) 2053–2055.

[13] R. Narayanan, M. A. El-Sayed, Nano Lett. 4 (2004) 1343–1348.

[14] R. Xu, D. Wang, J. Zhang, Y. Li, Chem.; Asian J. 1 (2006) 888–893.

[15] I. Lee, F. Delbecq, R. Morales, M.A. Albiter, F. Zaera, Nat. Mater. 8 (2009) 132–138.

[16] K. Ramanathan, M.A. Contreras, C.L. Perkins, S. Asher, F.S. Hasoon, J. Keane, J, D. Young, M. Romero, W. Metzger, R. Noufi, Prog. Photovolt.: Res. Appl. 11 (2003) 225−230.

[17] T.Y. Zhai, X.S. Fang, Y. Bando, B. Dierre, B.D. Liu, H.B. Zeng, X.J. Xu, Y. Huang, X.L. Yuan, T. Sekiguchi, D. Golberg, Adv. Funct. Mater. 19 (2009) 2423 2430.

[18] M. Zhang, T.Y. Zhai, X. Wang, Q. Liao, Y. Ma, J.N. Yao, J. Solid State Chem. 182 (2009) 3188–3194.

[19] Y. Li, L. Tang, S. Peng, Z. Li, G. Lu, Cryst. Eng. Commun. 14 (2012) 6974–6982.

[20] M. Matsumura, Y. Saho, H. Tsubomura, J. Phys. Chem. 87 (1983) 3807-3808.

[21] B. Pal, T. Torimoto, K. Iwasaki, T. Shibayama, H. Takahashi, B. Ohtani, J. Phys. Chem. B 108 (2004) 18670-18674.

[22] N. Bao, L. Shen, T. Takata, K. Domen, Chem. Mater. 20 (2008) 110-117.

[23] W.T. Chen, T.T. Yang, Y.J. Hsu, Chem. Mater. 20 (2008) 7204-7206.

[24] X.Z. Peng, Y.J. Yu, C.M. Tang, J.H. Tan, Q.X. Huang, Z. Wang, Sci Total Environ. 397 (2008) 1–3.

[25] A.N. Rao, B. Sivasankar, V. Sadasivam, J. Hazard. Mater. 166 (2009) 1357–1361

[26] A. Wood, M. Giersig, P. Mulvaney, J. Phys. Chem. B 105 (2001) 8810.

[27] W.Y. Cheng, W.T. Chen, Y.J. Hsu, S.Y. Lu, J. Phys. Chem. C 113 (2009) 17342–17346.

[28] V. Subramanian, E.W. Eduardo, P.V. Kamat, J. Am. Chem. Soc. 126 (2004) 4943-4950.

Chapter 4: Fine-tuning the Photoluminescence and Photocatalytic Properties of CdS Nanorods of Varying Dimensions

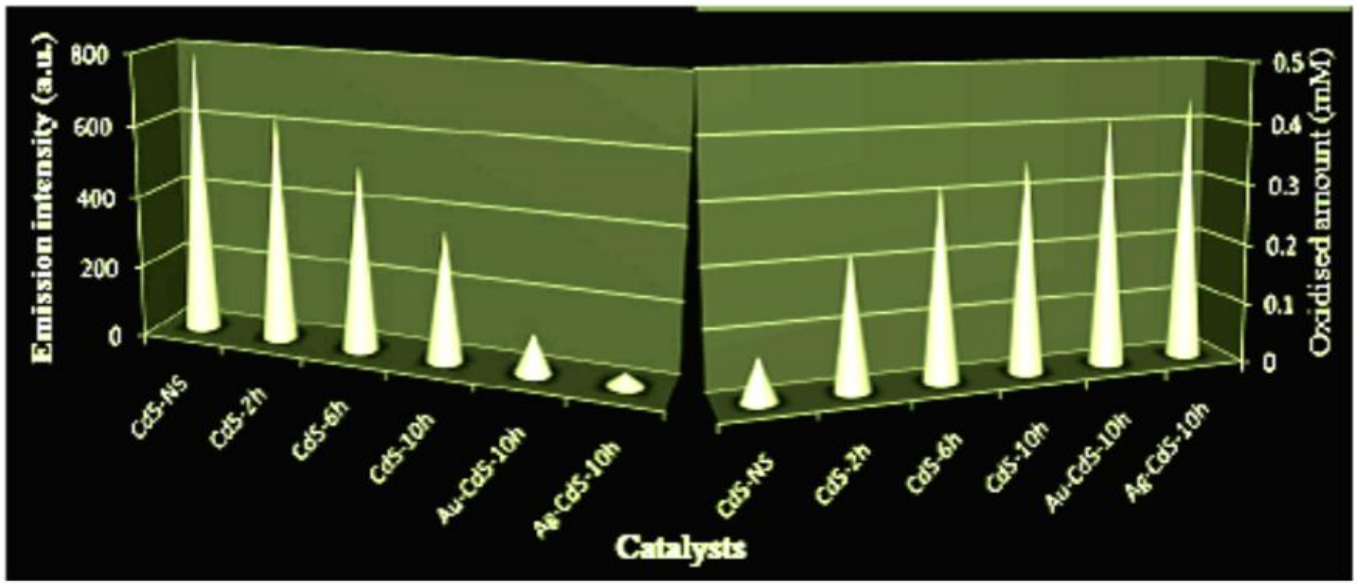

4.1. Introduction

To control the morphologies of materials at the nanoscale size has attracted considerable interest during the past few years. Among these morphologies, one dimensional (1D) nanostructures, such as nanowires, nanorods, nanobelts and nanotubes have drawn great attention because of their excellent physicochemical properties and practical applications in nanodevices [1-4]. An effective delocalization of charge species i.e., electrons and holes along the length of 1D-elongated nanostructures makes them a superior candidate in a variety of fields. In spherical crystals, benefits arising from higher surface-to-volume ratio with decreasing the particle size are significantly offset by the increased e^-/h^+ recombination probability at surface trapping sites. As a consequence, lower photocatalytic quantum yields are observed in spherical nanocrystals (NC) smaller than a certain dimension. The higher surface-to-volume ratio in NR in comparison to NS would guarantee a high density of active sites available for surface reactions as well as a high interfacial charge carrier transfer rate.

Cadmium chalcogenides; especially CdS having a relatively small band gap and thus are capable of harvesting photons in the visible region [chapter 1, ref. 38,39]. High aspect ratio CdS-NRs are particularly interesting as electrons are restrained in a specific direction which further influences their optical and electronic properties [5-7]. Currently, tailored and multifunctional nanostructured materials that comprise two or more different components such as Pt-CdS, PtNi-CdS, and PtCo-CdS hybrid nanostructures are at the forefront of research on nanomaterials [8-11]. It has been found that Pt deposition appears to occur preferentially on the tip of CdS-NR and the photo reactivity is higher at the tips than along the body of the CdS-NR due to the increased surface energy. Also surface modification of CdS-NR with coinage metals such as Au/Ag-CdS, Au-CdTe or Au-CdSe nanostructures and its composites like β-Fe_2O_3/CdS exhibited interesting optoelectronic properties because of better charge separation [12,13] has been reported.

Recently, hexagonal CdS-NR of different sizes are synthesized by many chemical routes and their visible light photoactivity for hydrogen production water splitting and dye degradation are studied by Au and Pt deposition [14,15]. However, the role of aspect ratio, band gap energy, surface area, crystallinity and metal co-catalysts deposits on the photoactivity of CdS-NR and their comparative variation has been not concisely investigated. Herein, we demonstrate the synthesis of CdS nanostructures of different aspect ratios and study the effects of above

mentioned physical parameters on the optical and photocatalytic properties of Au/Ag deposited CdS nanocomposites.

4.2. Experimental details

4.2.1. Synthesis of CdS-NR of different aspect ratios and Au and Ag (1-2 wt%) photodeposition:

CdS-NR with different aspect ratios were successfully prepared as mentioned in section- *2.2.2 of chapter 2*. Metal loading onto these particles was done by using a photodeposition technique as mentioned in *chapter- 2, section- 2.2.4.*

4.2.2. Photocatalytic activity

Photocatalytic efficiency of as prepared catalysts (10 mg) was carried out by degradation of 5 ml of 0.5 mM salicylic acid under UV light irradiations for different time intervals. The reaction sample was analyzed by UV–vis spectrophotometer (λ_{max} = 298 nm for salicylic acid) after filtration with 0.22 μm cellulose filter.

4.2.3. Characterizations

As synthesized bare CdS and M-CdS nanostructures with different dimensions were characterized by UV-vis, PL, XRD, TEM, EDX and SAED techniques. The specific surface area was determined by the N_2 adsorption method.

4.3. Results and discussion

4.3.1. Morphological analysis

The morphological study of synthesized CdS-NR has been carried out using transmission electron microscope (TEM) as shown in Fig. 1. It clearly reveals the formation of spongy glass wool/ or brush like CdS morphology when the precursor solution was heated only for 2 h (CdS−2 h). A close look at of same at higher magnification shows the grass leaf like morphology. This is in accordance with Ostwald ripening; mass transfer occurring from smaller particles to the largest NC [16]. Crystalline growth of CdS nanostructures observed with an increase in reaction time. Therefore to see the effect of reaction time on the morphology and crystallinity of CdS nanostructures, the precursors were heated for different time (2-10 h).

CdS-NR formed after autoclaving for 6 h (CdS−6 h) reveals the formation of some bunches of NW (at low resolution) which are found to be lengthy rod-shape particles of average length 140 ± 10 nm & width 5 nm (aspect ratio 28 ± 2, calculated by considering 20 individual particles) at high resolution. After 10 h autoclaving, aggregated sticks like CdS-NR (CdS−10 h) are seen (low magnification). The crystalline growth of a much longer (length 170 ± 10 nm) and wider (10 nm)

CdS-NR (aspect ratio 17 ± 1) having distinct lattice (inset) plane (002) than CdS−6 h samples are observed at high resolution. This obviously demonstrated that the length and width of CdS-NR is increased with reaction time, hence, the aspect ratio decreased and CdS become more crystalline in

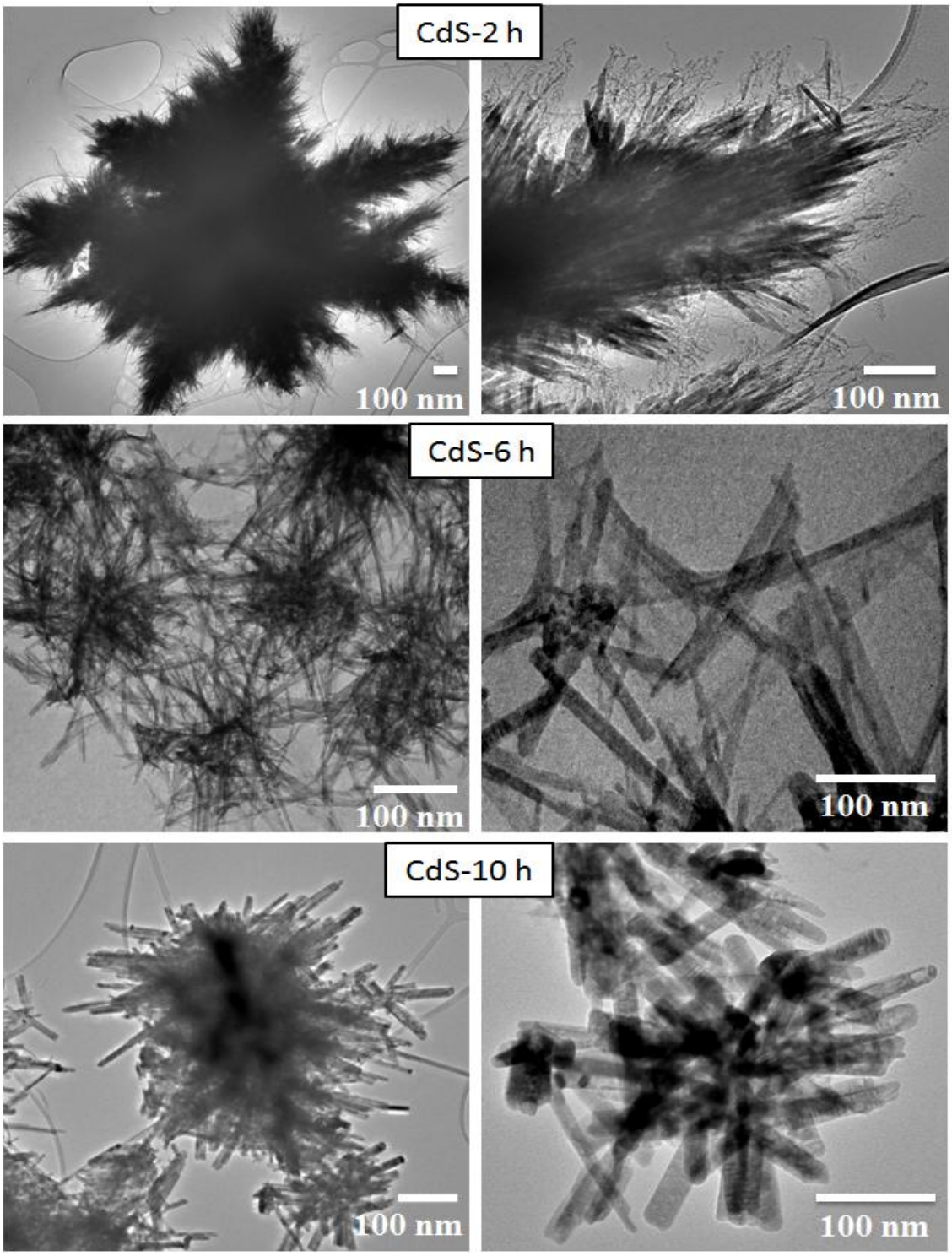

Fig. 1. TEM images of various CdS nanostructures synthesized during 2−10 h reaction at different magnifications.

nature. Selected area electron diffraction (SAED) pattern of above samples (Fig. 2) shows the more distinctive and prominent pattern for CdS−10 h NR. The concentric rings are more diffused and less intense because of the polycrystalline nature of CdS−2 h and CdS−6 h samples. In case of CdS−10 h sample, the diffraction rings are clearly separated and brighter individual ring/spots are visible due to high crystallinity of CdS nanorods which grow along the (002) direction. The calculated d_{hkl} values as per the respective diffraction rings are found to be 0.36 nm (100), 0.33 nm (002), 0.314 nm (101), 0.25 nm (102), 0.2 nm (110) and 0.17 nm (112). HRTEM image of a CdS−10 h sample further corroborate the high crystallinity; as the HRTEM of entire NR is found to compose of many (002) lattice planes orientation of spacing 0.33 nm confirms the hexagonal crystal structure of CdS.

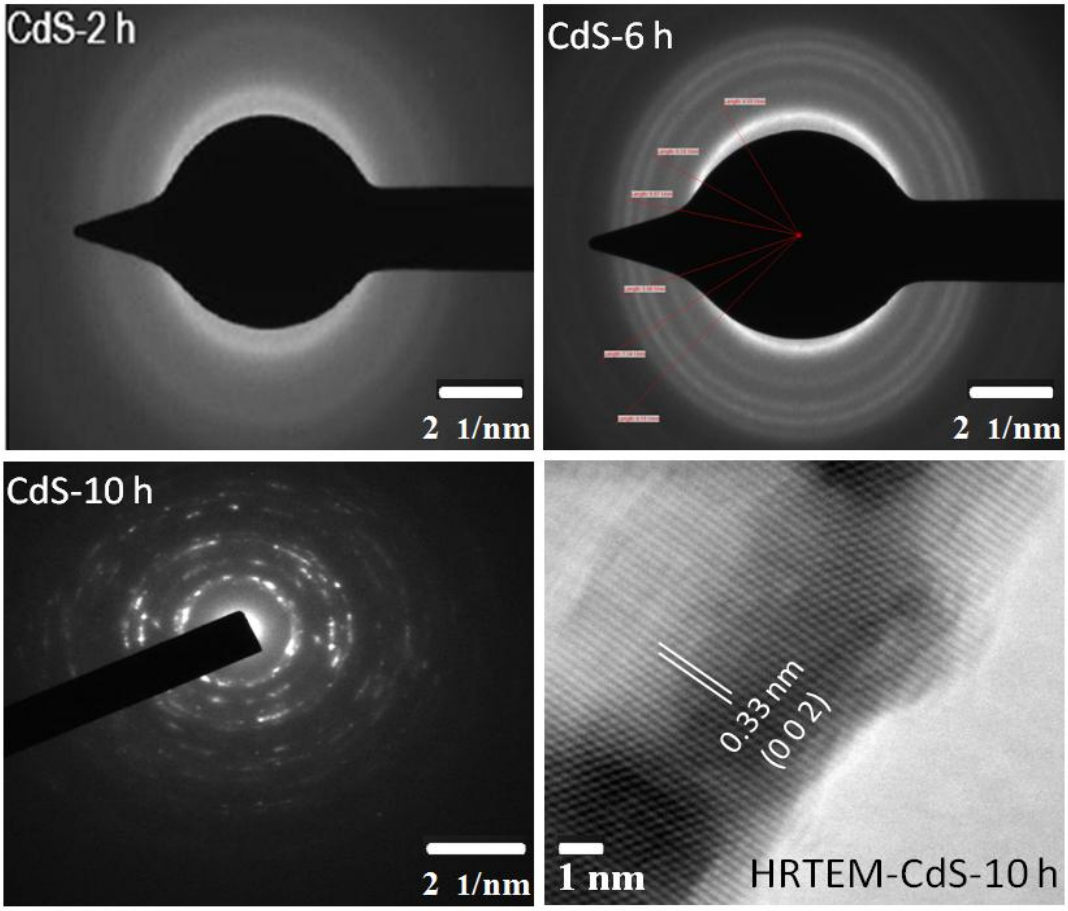

Fig. 2. Selected area electron diffraction (SAED) patterns of various CdS morphology and HRTEM image of a CdS-10 h nanorod.

Hence, the CdS-10 h sample was taken for the photo-catalytic study owing to their high

crystallinity, high length, fully grown with well defined morphology.

TEM images of 2 wt% Au and Ag photodeposited CdS−10 h NR are depicted in Fig. 3. Small spherical Au and Ag nanodeposits have been seen to be uniformly distributed throughout the surface of CdS-NR. Particle size histograms were built manually by measuring the diameter of 20 particles respectively, on TEM photographs.

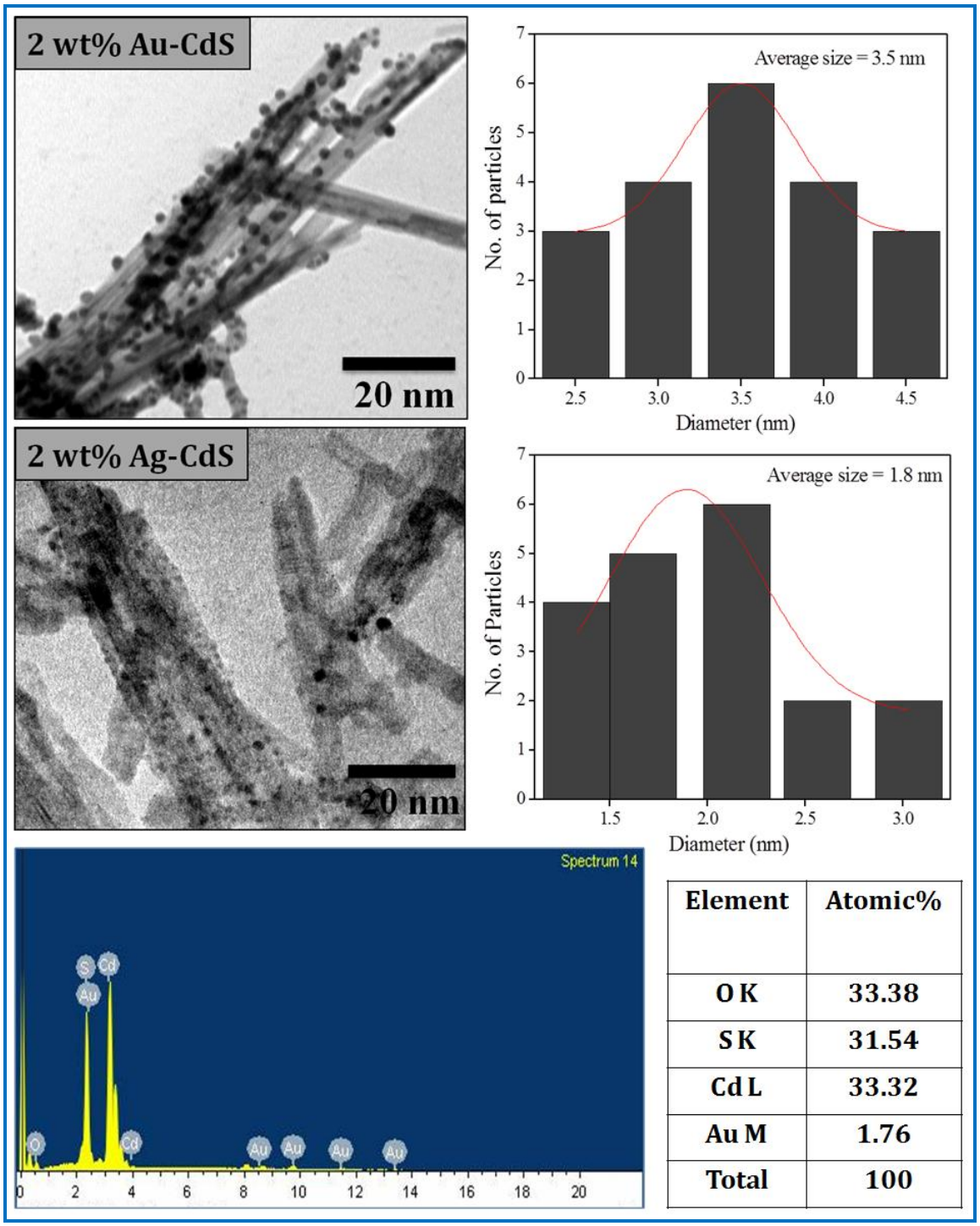

Element	Atomic%
O K	33.38
S K	31.54
Cd L	33.32
Au M	1.76
Total	100

Fig. 3. TEM images, EDX pattern and corresponding particle size distribution histograms of 2 wt% Au and Ag photodeposited CdS−10 h nanorods

The average size was determined by fitting the corresponding histogram with a Gaussian distribution function. The Au nanodeposits with an average size 3.5 nm and Ag-NPs of smaller size around 1.8 nm found to be deposited over a bunch of CdS-NR. However, the elemental analysis carried out using EDS confirmed the presence of 1.76 atomic weight% of Au on the surface of Au-CdS-NR.

4.3.2. Structural analysis

All the diffraction peaks (Fig. 4) of synthesized CdS-NR were strongly indexed to wurtzite structure having a hexagonal phase of CdS with lattice parameters (a = b = 4.042 Å, and c = 6.741 Å), which is in good agreement (JCPDS No. 41-1049). No additional peaks of impurities were detected, indicating the high purity of the synthesized product. In addition to this, strong intense and sharp diffraction peaks observed in CdS−10 h XRD patterns which suggest the obtained product possesses high crystallinity. The diffraction peak (002) becomes more intense and narrower in CdS−10 h than the peaks from other planes, which indicated its growth and higher crystallinity along the c-axis [17].

The diffraction planes consistently matched with the SAED pattern as discussed above. It is seen that the CdS become more crystalline with increased reaction time as confirmed by the XRD peak intensity variation. CdS−2 h diffraction peaks are very low intense due to the amorphous nature of smaller CdS nanostructure having no specific shape as shown in TEM images.

However, the enhancement of peak intensity with increasing reaction time from 6 to 10 h, evidencing the growth of more crystalline CdS-NR structure having different aspect ratios. As a result, the color intensity (Fig. 4 *inset*) of the different CdS nanostructures is also changed (greenish yellow to intense yellow) because of its varying dimensions and quantum size effect. Specific surface area (Fig. 4a *inset*) of CdS−2 h, CdS−6 h and CdS−10 h samples found to be 158, 122 and 76 m^2g^{-1}, respectively, which gradually decreased with the failing aspect ratio from 28 to 17 of CdS samples prepared at different reaction time. However, the calculated geometric surface area per particle is 2358 nm^2 for CdS−6 h and 5722 nm^2 for CdS−10 h samples.

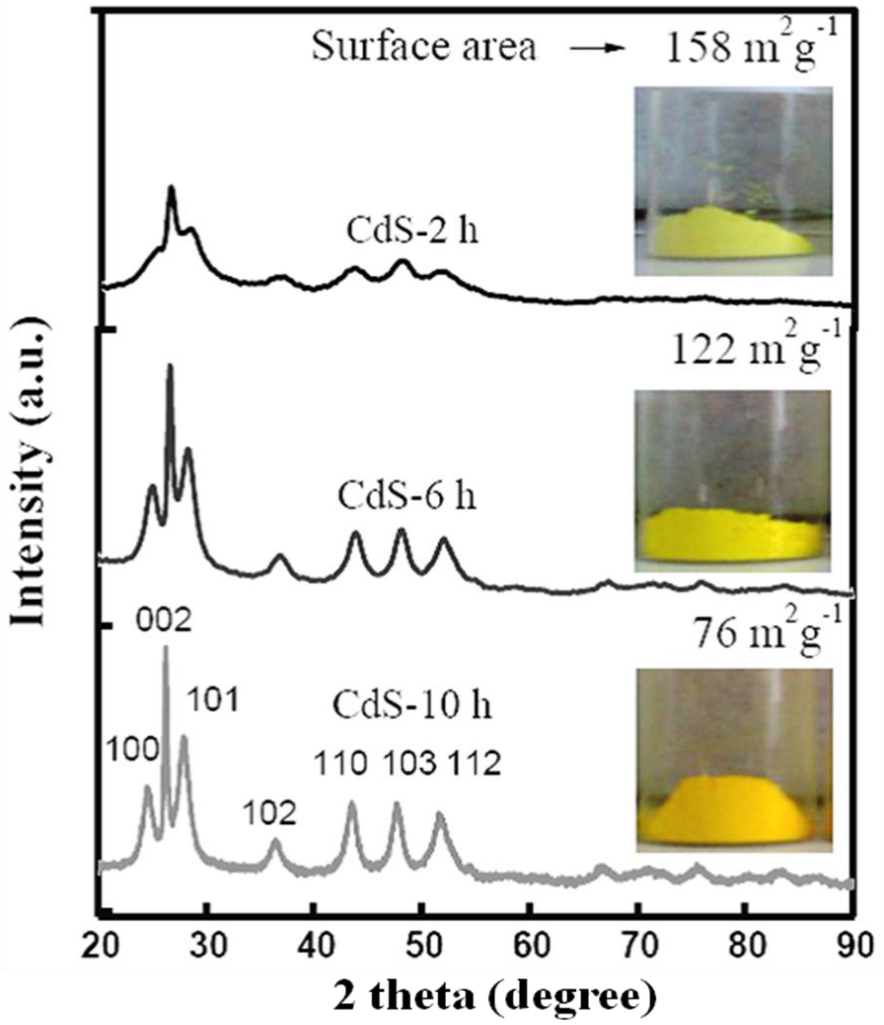

Fig. 4. XRD patterns, surface area and color of CdS powders having varying aspect ratio.

4.3.3. Optical properties

The absorption spectrum of as-prepared CdS-NR sample in comparison to CdS-NS is shown in Fig. 5a. The absorption onset of different CdS nanostructures synthesized at different reaction time clearly shows a blue-shift relative to ~540 nm for bulk CdS nanospheres (size > 10 nm) due to the quantum confinement effect. The measured absorption onset are dependent on the average sizes, i.e., ~485, 504 and 520 nm for CdS−2 h, CdS−6 h and CdS−10 h samples, respectively, that is increased with the decrease in aspect ratio. The corresponding band gap are 2.55, 2.41 and 2.35 eV for CdS-2 h, CdS-6 h and CdS-10 h samples, respectively, which are higher than 2.31 eV for bulk CdS-NS of size < 10 nm. This difference in band gap energies may change the energetic & location of conduction and valence band in varied extent. Hence, the photoexcited charge species

responsible for various photophysical processes may exhibit fascinating optoelectronic properties due to quantum confinement effect [17,18].

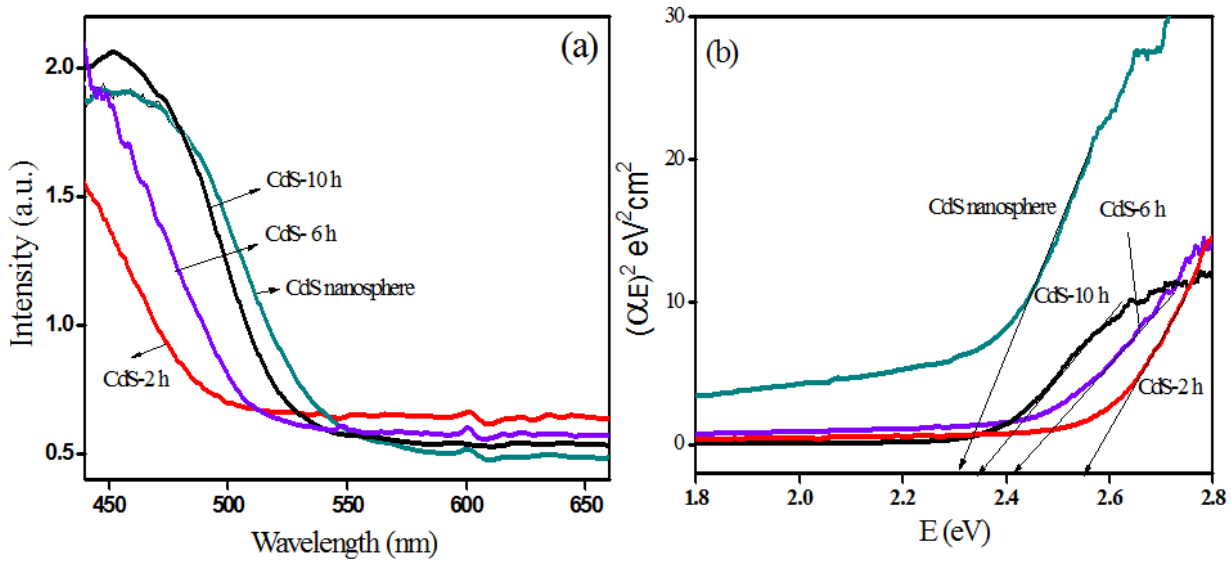

Fig. 5. (a) Diffuse absorbance spectra and (b) band gap energies of different CdS samples.

In fact, the CdS−2 h sample is found to be highly fluorescent in comparison to CdS−6 h and CdS−10 h NR as displayed in Fig. 6a. The photoluminescence (PL) spectra are measured at 380 nm excitation using 1 mg/ml of CdS in solvent acetone, diethyl ether and n-hexane in which acetone exhibits highly intense emission. Only trapped emission is observed [19] in case of protic solvents, whereas both excitonic and trapped fluorescence occur in aprotic solvents.

As shown in Fig. 6a, excited by the 380 nm UV light, all CdS nanostructures (acetone dispersion) of different aspect ratio, exhibit a wide green emission band from 460 nm to 570 nm. A strong PL emission peak at 485 nm (2.55 eV) for CdS-NS, 501 nm (2.47 eV) for CdS−2 h and 509 nm (2.43 eV) for CdS−6 h and 516 nm (2.40 eV) for CdS−10 h nanostructure is observed (Fig. 6a) along with a weak band at 527 nm. The intense PL peak of different CdS samples arises due to the excitonic fluorescence (band edge emission) most likely occurs from the radiative recombination of thermally detrapped electrons with valence band holes [19,20].

This is in well consistent with the respective CdS absorption onset value (2.55, 2.41 and 2.35 eV) as seen in Fig. 5a. In case of CdS-NS, the emission bands are quite intense and distinctly separated as compared to different aspect ratio CdS. This weak band at 527 nm can be ascribed to the radiative recombination of trapped charge carriers at the defect sites on the surface [20]. It is important to note

that the emission peak is gradually red-shifted from 485 to 516 nm and the luminescence intensity is also reduced by decreasing aspect ratio (increasing length) and increasing crystallinity of CdS-NPs having less surface defects. This blue-shifted absorption and red-shifted emission band as compared to bulk CdS arises due to quantum confinement effects that are in accordance with the previous works [21].

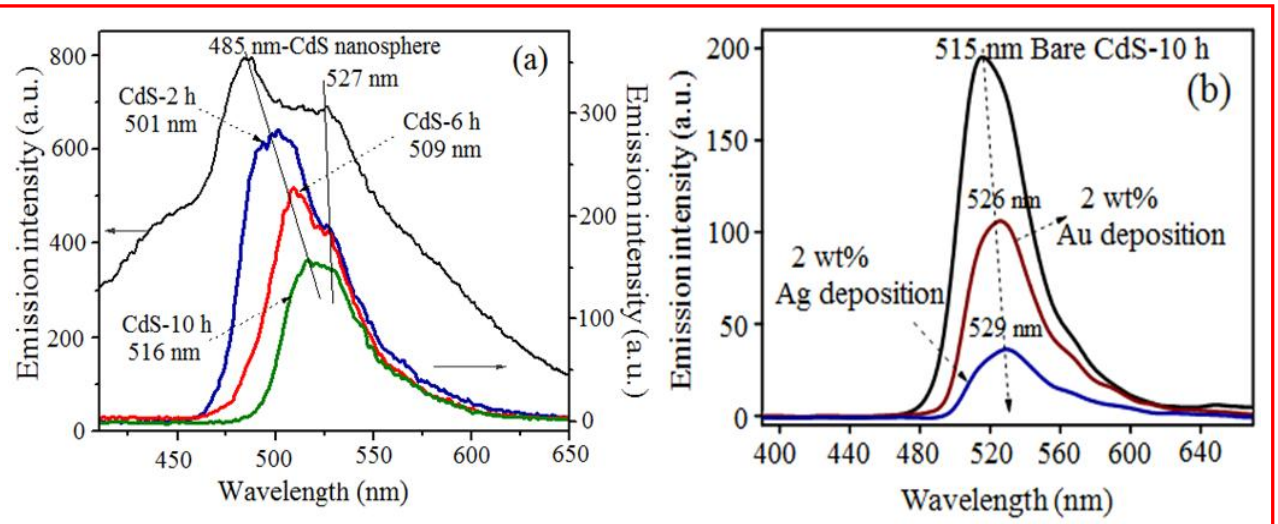

Fig. 6. Fluorescence emission (λ_{ext} = 380 nm) of different (a) bare and (b) 2 wt% Au & Ag photodeposited CdS samples.

One can observe that the PL intensity of CdS-NS and CdS−2 h nanostructure is stronger than CdS−6 h/10 h samples, which occur due to radiative emission by the recombination of trapped electrons/holes at the unreacted S^{-2} or Cd^{+2} trap sites on the grown-up CdS surfaces. Similar PL emission of CdS nanorods having a different aspect ratio is also reported by *Sun et al.* who observed strongest surface-trap emission at ~550 nm, with the 450 nm band-edge emission occurring only as a shoulder peak. Another crucial factor as reported is the superior delocalization of photoelectrons along the entire length of longer CdS-NR may retard the recombination rate. Hence, quench the radiative emission at 509 and 516 nm for lengthy CdS−6 h and CdS−10 h NR, respectively, as compared to CdS-NS and CdS−2 h morphology. The fluorescence excitation and absorption spectra of the CdS nanostructures are in good agreement indicating both a narrow particle size distribution and a contribution of all the particle sizes to the observed fluorescence [22,23].

The large extent of PL quenching of exciton emission by 2 wt% Au and Ag photodeposited CdS-10 h NR samples are shown in Fig. 6b. The intensity of the PL peak (band edge emission) of

the Au/Ag-CdS heterocomposites is significantly reduced as compared with bare CdS−10 h, this is due to the intimate contact of the CdS-NR with Au/Ag, facilitating the transfer of photogenerated electrons from the CdS to Au/Ag, and reducing the charge recombination [24]. The Ag deposition highly quenches the emission (526 nm) intensity than Au loading (529 nm) onto CdS−10 h surface. The PL peak position is red-shifted as compared to bare CdS−10 h (515 nm) NR because of the electronic interactions between the surface Plasmon band of Ag (~420 nm) and Au (540 nm) nanodeposits with CdS exciton. Moreover, the quenching ability is likewise dependent upon the size of Au (~3.5 nm) & Ag (~1.8 nm) nanodeposits formed on the CdS surface because the Fermi level equilibrium and charge transferability are size dependent.

4.3.4. Photochemical activity of CdS samples

It is well known that properties of CdS such as crystalline phase, size, morphology, specific surface area and defects can affect its PCA. Generally, hexagonal phase of CdS is preferred over cubic phase for better PCA . Matsumura et al. [25] found that 2% Pt-loaded CdS hexagonal crystal structure is much more efficient than that of cubic crystal structure. Fig. 7a showed the effect of aspect ratio for the photooxidation of salicylic acid by various bare and 2 wt% Au deposited CdS-NR under UV light irradiation.

It is observed that salicylic acid degradation rate gradually improved with the increasing length & crystallinity and decreasing aspect ratio of CdS-2 h to CdS-10 h NPs. Moreover, 2 wt% Au photodeposition on CdS-NR highly enhanced the photoactivity of respective bare samples. It is found that the CdS photoactivity is gradually increased with the decreasing surface area as 158 >122 >76 m^2 g^{-1} for the CdS−2 h, CdS−6 h and CdS−10 h nanostructures, respectively. However, the exposed geometrical surface area per particle is 2358 nm^2 for CdS−6 h and 5722 nm^2 for CdS−10 h samples may lead to increase the salicylic acid absorption for improved PCA of lengthy CdS-NR. Despite having highest surface area (158 m^2/g) and no shape specific morphology, the CdS-2 h catalyst exhibited lowest photoactivity.

It is known that sulfides with small surface areas of <10 m^2g^{-1} showed good photocatalytic efficiency because of their good crystallinity and less crystal defects that can largely reduce the bulk electron–hole recombination during the migration of electrons and holes to the surface of CdS. High yields of hydrogen could be obtained with CdS samples with very large (>> 100 m^2/g) or very low (< 6.7 m^2/g) specific surface areas. The diminishing surface to volume ratio from 0.82 nm^{-1} of CdS-6 h to 0.41 nm^{-1} of CdS-10 h, the sample would not be able to reasonably explain the

high activity of longer & wider CdS-NR. This relation of surface area and PCA suggests that the improved crystallinity and rapid delocalization of photogenerated charge carriers along the length of CdS-NR probably slowed down the electron-hole recombination and hence, increased the PCA.

Fig. 7b shows the effect of amount of Au and Ag deposits on the PCA of CdS−10 h NR. The deposition of noble metal promotes interfacial charge-transfer processes in composite systems because charge accumulation in the metal deposit led to Fermi-level equilibration [26,27] at the metal-semiconductor interface and thereby, enhances the PCA. The photoinduced holes and electrons in the CdS-NC migrate to the NPs surface easily, and they are effectively trapped at the

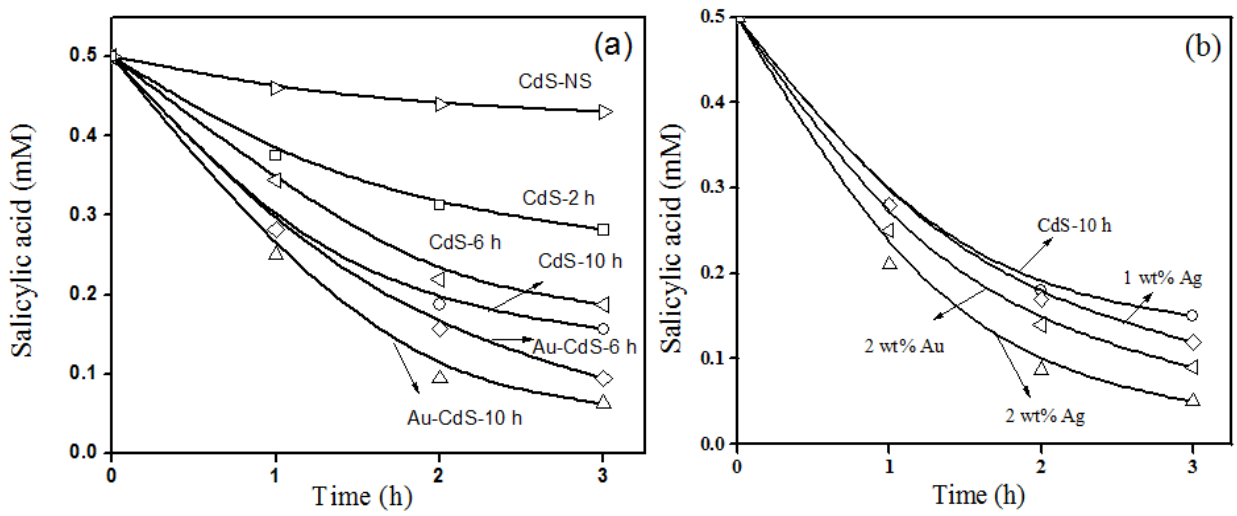

Fig. 7. Photocatalytic oxidation of 0.5 mM salicylic acid by (a) bare & 2 wt% Au photodeposited CdS samples and (b) effect of amount of metals loading on the photoactivity of CdS−10 h NR.

Au/Ag-CdS interface where they are captured by the reactants in the solution. As a result strongly oxidizing h^+ could be available for photooxidation of adsorbed salicylic acid effectively at a better rate. As the Fermi level of Ag metal is closer to the conduction band position of CdS, the electron transfer occurs from CdS to Ag more rapidly than Au, resulting in a uniform Fermi energy level in Ag-CdS composites. Furthermore, the difference in size of deposited Au (~3.5 nm) and Ag (~1.8 nm) co-catalysts also alter the co-catalytic activity because Fermi energy is size dependent. As the amount of Ag co-catalyst loading is increased from 1 to 2 wt%, the degradation efficiency (Fig. 7b) is also improved due to active participation of optimum number of Ag-CdS composites in photoinduced charge transfer processes.

Fig. 8 displayed the relationship between PCA (salicylic acid oxidation) and PL ($\lambda_{ext.}$ = 380 nm in acetone dispersion) of various CdS nanostructures as described above. It is verified that the PCA increases while photoemission decreases with the crystallinity, length, BET surface area, surface

to volume ratio, molecular area and after Au and Ag deposition.

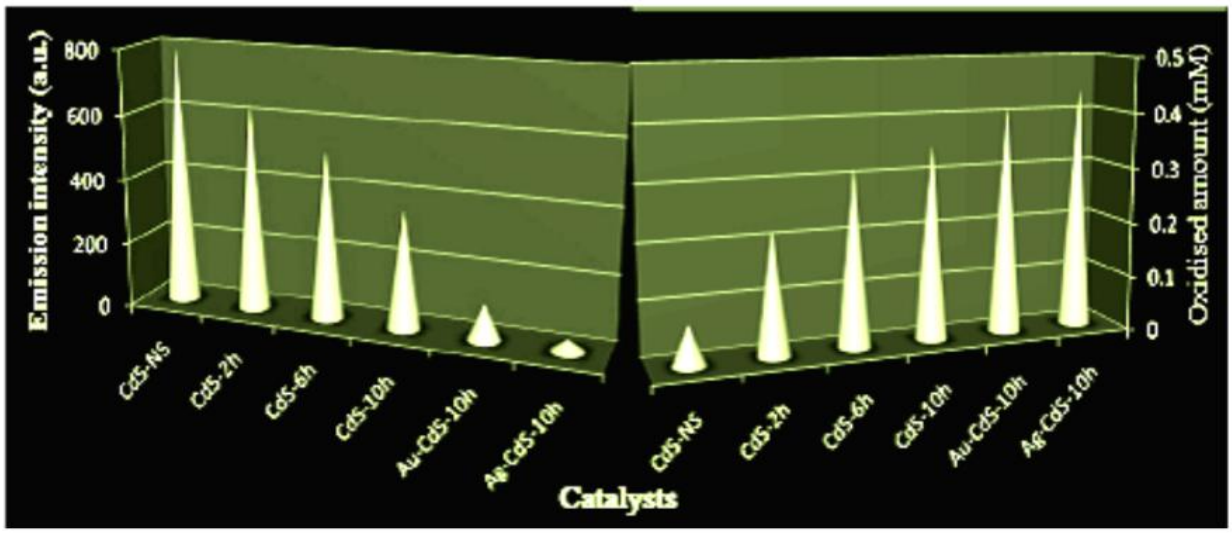

Fig. 8. Correlation of photooxidation of salicylic acid (0.5 mM) and photoluminescence of various CdS and Au/Ag-CdS nanostructures.

The Ag (2 wt%) photodeposition onto CdS-10 h NR exhibit lowest luminescent property and highest photoactivity. The correlation between PL and PCA can be well explained on the basis of size-, shape- of CdS and also on the nature and size of co-catalyst. By tuning the morphology from spherical to CdS-NR, lifetime of photogenerated charge carriers (e^-/h^+) is expected to be increased by their delocalization along elongated (longitudinal) side, which was further improved by increasing the length. Additionally, coinage metals such as Au and Ag in contact with CdS serves as a reservoir of photoactivated electrons, thus improving the interface charge-transfer process and hence retards the recombination rate. Consequently, the long term separation of the charge carriers leads to reduction in fluorescence quenching and avail the number of holes for superior photooxidation of salicylic acid.

The growth of CdS nanostructures of tunable aspect ratio can be controlled by controlling the reaction time at a particular temperature of autoclaving. The effect of surface area, surface to volume ratio, crystallinity and aspect ratio and nature of co-catalyst was well correlated with photoluminescence and photoactivity.

4.4. References

[1] Z.W. Pan, Z.R. Dai, Z.L. Wang, Science 291 (2001) 1947.

[2] Z. Zhang, W. Guo, Phys. Rev. B 77 (2008) 075403-07540.

[3] X. Han, L. Kou, X. Lang, J. Xia, N. Wang, R. Qin, J. Lu, J. Xu, Z. Liao, X. Zhang, X. Shan, X. Song, J. Gao, W. Guo, D. Yu, Adv. Mater. Commun. 21 (2009) 4937-4941

[4] C.N.R. Rao, R. Voggu, A. Govindaraj, Nanoscale 1 (2009) 96.

[5] A.E. Saunders, A. Ghezelbash, P. Sood, B.A. Korgel, Langmuir 24 (2008) 9043-9049.

[6] I. Gur, N.A. Fromer, M.L. Geier, A.P. Alivisatos, Science, 310 (2005) 462−465.

[7] X. Sun, X. Ma, L. Bai, J. Liu, Z. Chang, D.G. Evans, X. Duan, J. Wang, J.F. Chiang, Nano Res. 4 (2011) 226-232.

[8] S.E. Habas, P. Yang, T. Mokari, J. Am. Chem. Soc. 130 (2008) 3294-3295.

[9] B.D. Yuhas, S.E. Habas, S.C. Fakra, T. Mokari, ACS Nano 3 (2009) 3369-3376.

[10] M.G. Alemseghed, T.P.A. Ruberu, J. Vela, Chem. Mater. 23 (2011) 3571-3579.

[11] R. Costi, A.E. Saunders, E. Elmalem, A. Salant, U. Banin, Nano Lett. 8 (2008) 637-641.

[12] A. Kumar, A. Singhal, J. Mater. Chem. 21 (2011) 481–496.

[13] T. Shanmugapriya, P. Ramamurthy, J. Phys. Chem. C 117 (2013) 12272−12278

[14] Y. Li, J. Du, S. Peng, D. Xie, G. Lu, S. Li, Int. J. Hydrogen Energy 33 (2008) 2007-2013.

[15] N. Gupta, B. Pal, J. Nanosci. Nanotechnol. 13 (2013) 1-11.

[16] M. Berr, A. Vaneski, A.S. Susha, J.R. Fernández, M. Doblinger, F. Jackel, A.L. Rogach, J. Feldmann, Appl. Phys. Lett. 97 (2010) 1-3.

[17] W. Cai, Z. Li, J. Sui, Nanotechnology 19 (2008) 1-6.

[18] S. Chen, X. Zhang, Q. Zhang, W. Tan, Nanoscale Res Lett. 4 (2009) 1159-1165.

[19] U. Resch, A. Eychmiiller, M. Haase, H. Weller, Langmuir 8 (1992) 2215-2218.

[20] H. Zhang, S. Delikanli, Y. Qin, S. He, M. Swihart, H. Zeng, Nano Res. 1 (2008) 314-320.

[21] K.T. Yong, Y. Sahoo, M.T. Swihart, P.N. Prasad, J. Phys. Chem. C 111 (2007) 2447-2458.

[22] Z. Li, J. Sui, X. Li, W. Cai, Langmuir 27 (2011) 2258-2264.

[23] A. Pan, X. Lin, R. Liu, C. Li, X. He, H. Gao, B. Zou, Nanotechnology 16 (2005) 2402-2406.

[24] T.T. Yang, W.T. Chen, Y.J. Hsu, K.H. Wei, T.Y. Lin, T.W. Lin, J. Phys. Chem. C 114 (2011) 11414-11420.

[25] M. Matsumura, S. Furukawa, Y. Saho, H. Tsubomura, J. Phys. Chem. 89 (1985) 1327-1329.

[26] P.V. Kamat, Pure Appl. Chem. 74 (2002) 1693-1706.

[27] M.I. Litter, Appl. Catal., B. Environ. 23 (1991) 89-114.

Chapter 5: Study of Excited Charge Carrier's Lifetime for the Observed Photoluminescence and Photocatalytic activity of CdS Nanostructures of Different Shapes

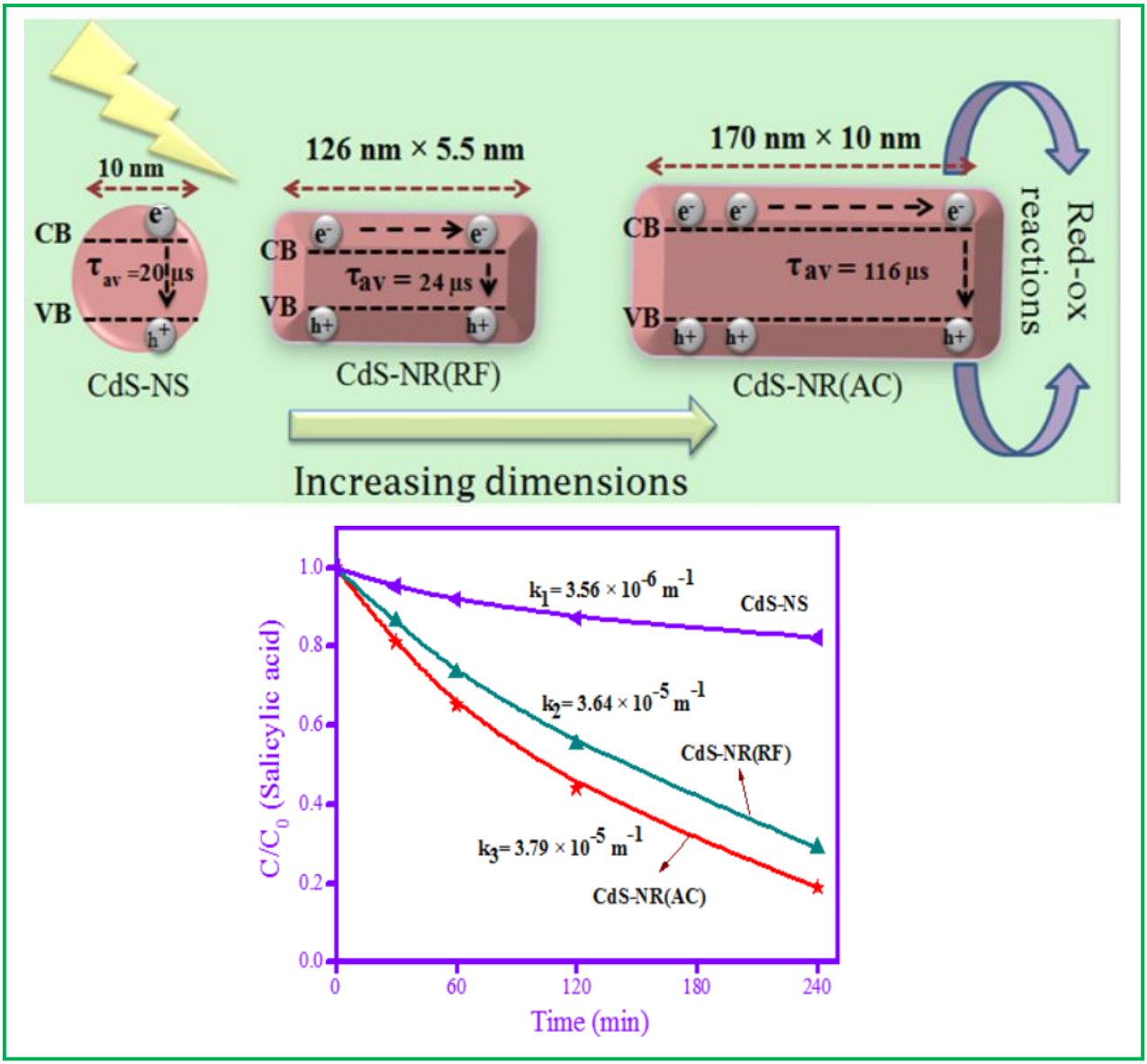

5.1. Introduction

The fascinating properties of nanomaterials are strongly influenced by their particle size, shape and surface modifications [1–3] as already discussed in the above chapters. Numerous efforts have been devoted to understanding the charge carrier relaxation dynamics in semiconductor nanostructures as a function of their size, shape, composition and surface properties [4-6]. The time-resolved photoluminescence (PL) spectroscopy has been set up to be a quantitative tool for the analysis of charge carrier dynamics in NCs in the recent research. As the CB and VB positions of a given crystallite depending upon the particle shape and size, it would therefore be possible to control the redox ability of NPs by changing their dimensions [7], which are very sensitive to the preparation techniques.

The direct band gap of CdS (2.42 eV), ease of crystallization, anisotropic growth, and higher electron mobility and facile tailoring of structures gives it an edge over other semiconductors. Several techniques have been used to synthesize CdS nanostructures such as sol–gel, multiple injection process and hydrothermal approach. But precise control over the size, shape and crystallinity of nanostructures made solvothermal and wet chemical routes more feasible to the others. The recombination of photoexcited electron–holes are slowed down in case of cylindrical symmetry of the rod-shaped morphology, thereby, improved the photophysical processes. Size dependent time-resolved PL decay of colloidal CdSe NCs and their correlation with the fluorescence lifetime have been discussed by Zhang et al. [8]. Mohamed et al. [9] have reported the shape-dependent relaxation dynamics of CdSe nanocrystals including NR and nanodots and found faster carrier relaxation dynamics in nanorods than nanodots due to the lowering of symmetry. Furthermore, the Mclaren group reported the influence of the size and shape of ZnO nanocrystals on photocatalytic activity and clearly suggests that the terminal polar faces are more active surfaces for photocatalysis than the nonpolar surfaces perpendicular to them [3].

Another approach to modifying the CdS-NR surface is the deposition of noble metal that improves photocatalytic efficiency by enhancing the interfacial charge transfer process as already discussed in chapter 4. Therefore, nanostructures composed of both Au and CdS would expect to be show much more interesting results than the individual constituents.

In this context, CdS-NS and NR of varying length and width have been deviced to measure the photoexcited charge carrier’s lifetime by time resolved fluorescence spectroscopy and studied its effect on the luminescence property and photocatalytic activity for the oxidation–reduction

reactions. The role of Au deposition onto CdS nanocrystals has been also investigated for the electron–hole recombination time in correlation with their photoactivity.

5.2. Experimental details

5.2.1. Synthesis of CdS nanostructures and their surface modifications

CdS-NS and two different CdS-NR (CdS-NR(RF) & CdS-NR(AC)) were prepared as discussed in the *section- 2.2.1 and 2.2.2 of chapter 2.* 1 wt% Au nanoparticles were loaded on CdS-NR by photodeposited method *(section-2.2.4).*

5.2.2. Preparation of silica coated CdS (SiO_2@CdS) nanorods

A thin layer of silica was coated onto CdS-NR surface as described in *chapter 2, section-2.2.5*

5.2.3. Photocatalytic activity

The catalytic activity was tested for the photooxidation of 5 ml (0.5 mM) salicylic acid and photoreduction of (0.2 mM) p-nitrophenol with 10 mg catalyst (bare CdS, Au–CdS, SiO_2@CdS-nanostructures) in a test tube under UV light irradiation with constant magnetic stirring for different time periods. The reaction sample was analyzed by UV–vis spectrophotometer after filtration with 0.22 μm cellulose filter. The alcoholic suspensions (5 ml, 50%, v/v) containing 0.2 mM of 4-nitrophenol along with catalyst were thoroughly purged with nitrogen before irradiation. The reductions of p-nitrophenol to p-aminophenol were determined using high performance liquid chromatography using C-18 column, 220 nm wavelength and MeOH: H_2O (50:50) as the mobile phase with a flow rate of 1 ml/min.

5.2.4. Characterizations

Synthesized catalysts were characterized by UV-vis, PL, XRD, FE-SEM, TEM, and SAED techniques. The specific surface area was determined by the N_2 adsorption method. Time resolved luminescence spectra have been recorded using N_2-laser excitation wavelength 490 nm.

5.3. Results and discussion

5.3.1. Morphological and structural characterization

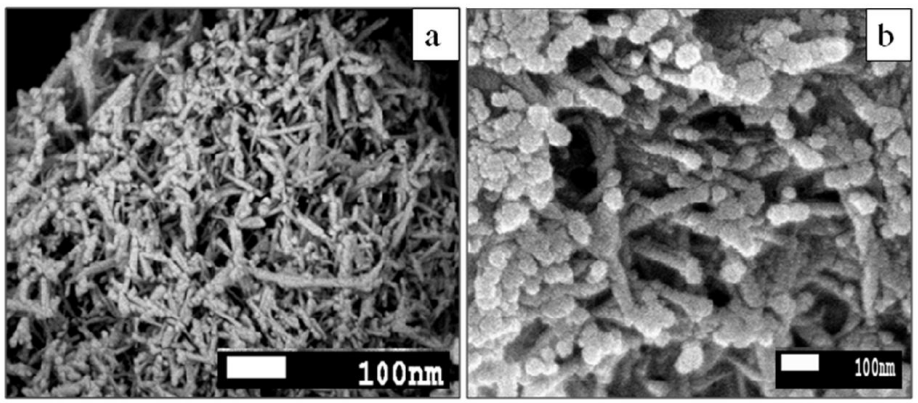

Fig. 1. FE-SEM images of (a) CdS-NR(RF) and (b) CdS-NR(AC) particles.

The FE-SEM surface morphology of CdS-NR prepared by two different techniques is shown in Fig. 1. CdS-NR fabricated under refluxing (Fig. 1a) conditions, and under controlled pressure in an autoclave (Fig. 1b) at 120 °C achieved the uniform growth along radial as well as longitudinal facets. The aspect ratio of as synthesized CdS-NR under SEM analysis consistently well matched with TEM photographs.

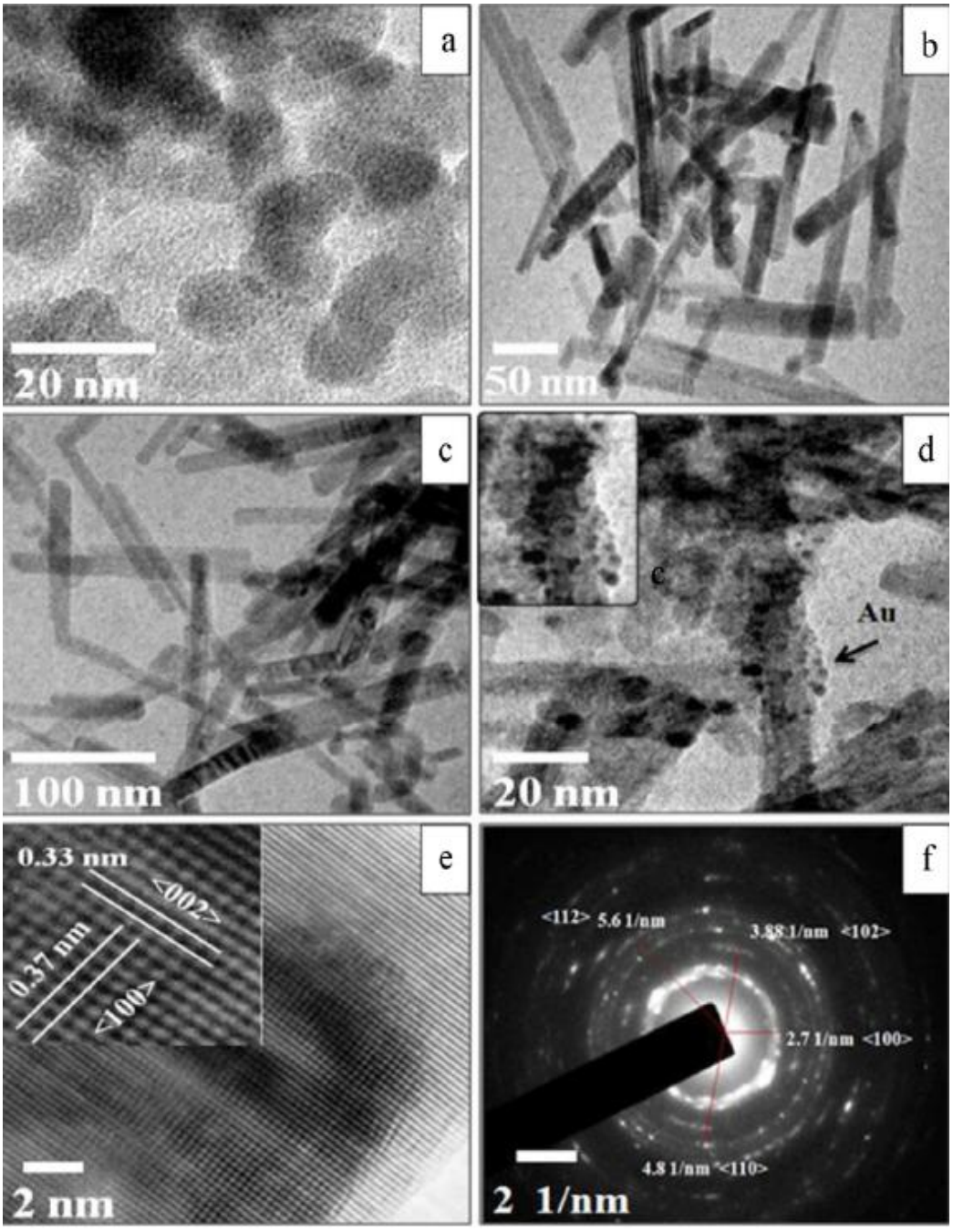

Fig. 2. TEM images of (a) CdS-NS, (b and c) CdS-NR(AC), (d) 1 wt% Au photodeposited CdS-NR(AC), (e) lattice fringes and (f) SAED pattern.

The CdS-NRs prepared by autoclave (CdS-NR(AC)) are found to be longer in length and width as compared to that those are prepared by the refluxed method (CdS-NR(RF)). Fig. 2a shows the TEM images of CdS-NS of uniform size ca. 10–12 nm and shape and the size of CdS-NR having an average length ∼170 nm and width ∼10 nm corresponding to an aspect ratio = 17 are obtained by autoclaving as seen in Fig. 2b and 2c. Fig. 2d represents the TEM images of 1 wt% Au photodeposited CdS-NR(AC) which shows that spherical Au-NP of size ∼3.5 nm are randomly deposited over some of the CdS surface along with few aggregated Au deposits are also formed. However, the number of Au islands and their distribution is not same for each CdS particle. An enlarged view (inset) from the marked area clearly evidencing Au-NP deposition onto CdS-NR. The HRTEM image in Fig. 2e shows two overlapped CdS-NR having characteristic lattice fringes of ca. 0.33 and 0.37 nm for (002) and (100) lattice planes, respectively, for hexagonal crystal structure. The SAED pattern in Fig. 2f consists of many concentric bright rings and spots, further confirming the high crystallinity and presence of distinctive lattice planes of hexagonal CdS of polycrystalline in nature.

The HR-TEM images in Fig. 3a revealed that a bunch of CdS-NR(RF) and a clear distinct surface morphology of many lengthy CdS-NR having an average length ∼126 nm and width ∼5.5 corresponding to an aspect ratio ∼23 were obtained by refluxing method as seen in Fig. 3b and 3c. The Au (1 wt%) deposited CdS-NR in Fig. 3d revealed that many small Au nanodots of size ∼2–3 nm are deposited throughout the CdS nanorods. The HRTEM image in Fig. 3e also shows lattice fringes having inter planner distance of 0.33 nm corresponds to the growth of (0 0 2) plane of CdS-NR crystals along the crystallographic c-axis.

The SAED pattern in Fig. 3f consists of relatively broad diffuse diffraction rings of CdS-NR(RF) as compared to well resolved bright rings (Fig. 2d) of CdS-NR(AC), indicating higher crystallinity of CdS-NR(AC) formed due to a high pressure condition in an autoclave.The circular diffraction rings can be indexed to (1 0 0), (0 0 2), (1 0 2), (1 1 0) and (1 0 3) planes corresponding to their measured d_{hkl} values of 0.37 nm, 0.33 nm, 0.25 nm and 0.21 nm, respectively, for hexagonal CdS morphology in accordance with the XRD patterns.

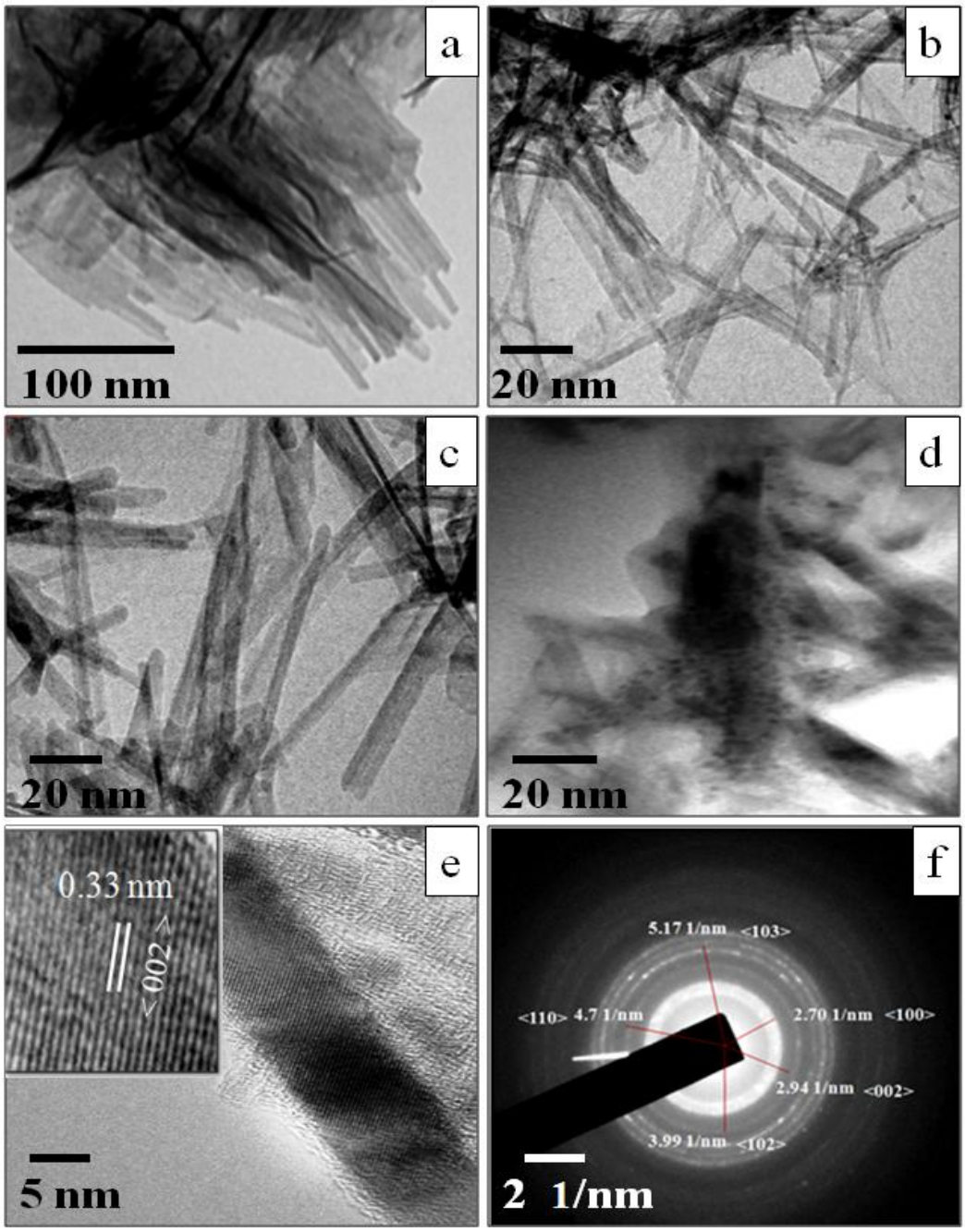

Fig. 3. TEM images of (a-c) CdS-NR(RF), (d) 1 wt% Au photodeposited CdS-NR(RF), (e) lattice fringes and (f) SAED pattern.

However, the specific surface area of these two CdS-NR are an almost same ca. 76 m^2g^{-1} (CdS-NR(AC)) and 81 m^2g^{-1} (CdS-NR(RF)), despite having a notable difference in their aspect ratio. The structural analysis of the synthesized CdS-NR has been carried out using XRD as shown in Fig. 4.

The diffraction peaks suggest that CdS-NR possess a wurtzite structure having lattice parameters a = b = 4.042 A˚, and c = 6.741 ˚A which are in good agreement with JCPDS No. 41-1049 data card. It could be notice that all the diffraction peaks of CdS-NR(AC) are more intense and sharper than CdS-NR(RF) having relatively broader XRD peaks. The Au photodeposition, substantially diminishing the intensity of CdS-NR(AC) diffraction peaks, probably, due to the suppression of electron scattering of CdS by heavier Au metal attached to the CdS surface. The measured d_{hkl} values of the respective diffraction planes: 0.36 nm (100), 0.33 nm (002), 0.314 nm (101), 0.25 nm (102), 0.2 nm (110) and 0.17 nm (112) has consistently matched with the SAED patterns (Fig. 2f and 3f) and TEM images. A little variation in the growth of lattice planes and crystallinity between two CdS-NRs is evident to the broadness and the peak intensity difference. Especially, the more intense and stronger (002) diffraction peaks of CdS-NR(AC) indicates preferential growth [7] along the crystallographic c axis and seems to be more crystalline than CdS-NR(RF) as found in XRD data and TEM shape analysis.

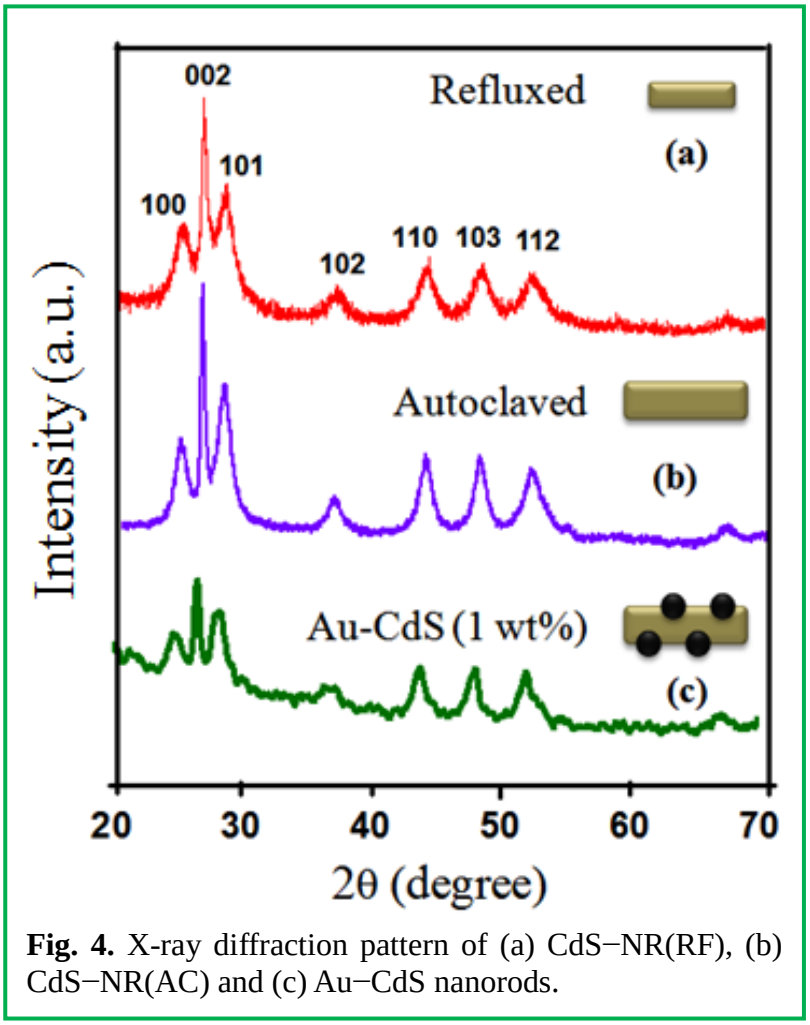

Fig. 4. X-ray diffraction pattern of (a) CdS−NR(RF), (b) CdS−NR(AC) and (c) Au−CdS nanorods.

5.3.2. Optical spectroscopy

It is well-known that semiconductors exhibit quantum size effects, when the size of the particle is smaller than the bulk exciton radius as a result of the spatial confinement of the charge carriers. The change in the absorption of CdS samples with respect to their size and shape and surface modification with 1 wt% Au co-catalyst is shown in Fig. 5a.

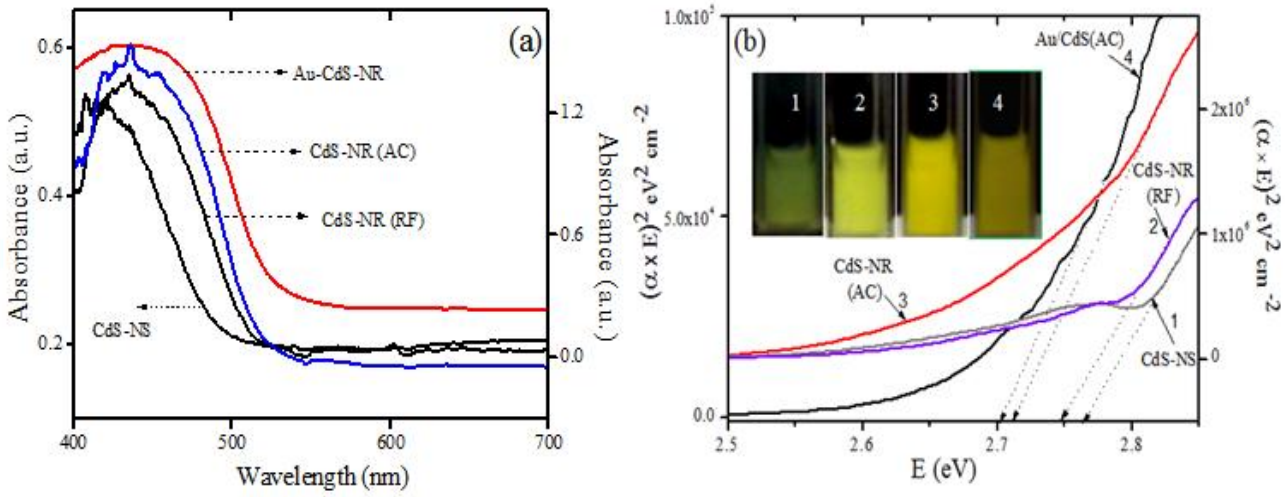

Fig. 5. (a) Solid state absorption spectra and (b) band gap energy of various CdS & Au−CdS nanostructures (inset−colour changes).

CdS-NS displayed absorption onset at 480 nm while both CdS-NR(AC) and CdS-NR(RF) exhibited onset around 518 nm with exciton bands at 417 nm and 437 nm, respectively. However, after Au deposition onto CdS-NR(AC) surface, the CdS exciton band disappeared and does not show the evolution of any characteristic surface Plasmon band due to Au nanodeposits as already discussed in chapter 4. As compared with that of the bulk band gap of CdS (2.42 eV), the calculated band gap values 2.77, 2.75, 2.73 and 2.71 eV for CdS-NS, CdS-NR(RF), CdS-NR(AC) and Au–CdS-NR(AC), respectively, clearly indicate the significant change in the band energies that may display quantum-size effects in the prepared CdS nanostructures. The variation in color intensity (Fig. 5b – inset) of various CdS nanostructures reflects their observed optical absorption at different wavelengths owing to their variation in dimensional morphology.

The fluorescence emission (λ_{ext} = 380 nm) spectra of different bare and Au loaded CdS nanostructures dispersed in acetone (1 mg/ml) at room temperature are shown in Fig. 6a. Generally, the photoluminescence originates either from band edge or recombination of surface

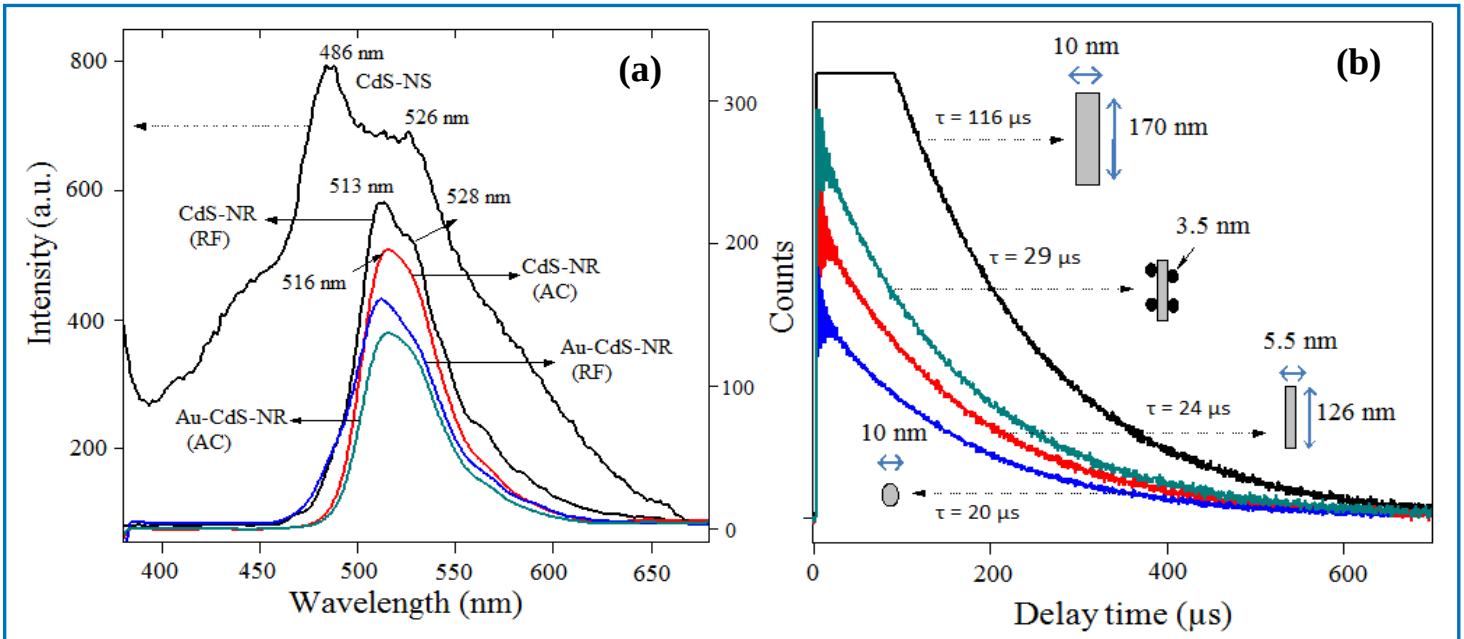

Fig. 6. (a) Photoemission spectra of CdS and Au-CdS nanostructures in acetone dispersion at excitation 380 nm and (b) Time resolved fluorescence decay curves of different bare and Au-CdS nanostructures.

state energy levels. In our case, emission bands in CdS-NS are highly intense and distinctly separated as compared to CdS-NRs synthesized by autoclaving and refluxing techniques. CdS-NS exhibited one strong band at 487 nm arises due to recombination of thermally de-trapped electrons with holes (band edge emission) and the other weak band at 527 nm ascribed to the radiative recombination of trapped charge carriers at the defect sites on the CdS surface. However, in case of CdS-NR, the band gap emission appeared around 512–516 nm and very weak surface traps at 525–528 nm occur due to the defect's site is not distinctive as compared to CdS-NS luminescence, which leads to its crystalline structure.

With the decrease in an aspect ratio of CdS-NR from 23 to 17, or increase in length/width of NR (126 nm/5.5 – 170 nm/10 nm), the luminescence intensity is gradually decreased owing to the de(localization) of charge carriers along the elongated side as well as the reduction in crystal defects. Au deposition onto CdS surface significantly quenched the luminescence intensity; seemingly, an electron-transfer from the CdS to the Au metal dots reduced the surface defect sites. The small Au deposits actually blocking the shallow surface traps that prevent the electron–hole pair recombination rates. In other words, low PL intensity suggests a low density of recombination centers and consequently, long lifetime of photogenerated carriers. Moreover, CdS excitons–Au Plasmon interactions are suppressed as a result of ultrafast carrier trapping by the interfacial states and hence, quenched the emission intensity.

To understand the luminescence dynamics of photogenerated charge carriers in terms of their residence time and recombination time with respect to the size and shape, ***time-resolved emission*** was measured and compared. Though, some reports are available regarding the luminescence study of cysteine-mediated Ag@CdS nanocolloids [10] and $Cd_{(1-x)-y}Zn_xMn_yS$ [11] nanocrystals, still the influence of size and shape onto the band edge and trapping states still remains a challenge. The luminescence is found to arise from two distinct and parallel channels such as band edge excitonic emission and trapping state emission. The charge carrier's relaxation dynamics of these spheres, rods-like and Au photodeposited CdS-NPs are shown in Fig. 6b, which is measured by pulse excitation method. Samples are exposed to nitrogen laser (wavelength = 490 nm) and time resolved decay curves are obtained from where lifetime values of the various excited states have been calculated. It is worth pointing out that the average lifetime τ_{av}, is related to band edge lifetime τ_1 and trapping or defect states given by the following equation

$$\tau_{av} = a_1\tau_1 + a_2\tau_2 / a_1 + a_2$$

where a_1 and a_2 denote the amplitude of band edge and trapping state emission, respectively. The estimated average lifetimes are in the range of few hundreds of nanoseconds, i.e., 20, 24, 29 μs for CdS-NS, CdS-NR of length 126 nm and width 5.5 nm, and Au–CdS-NR(RF), respectively. An increase in relaxation time of photoexcited electron–hole pairs is observed with the shape change from spherical CdS-NPs to lengthy rod like cylindrical symmetry, manifested to retardation of recombination time, which was further improved by depositing Au-nanodots. Furthermore, when the dimensions (length 170 nm and width 10 nm) of CdS nanorods (CdS-NR(AC)) is increased as compared (length 126 nm and width 5.5 nm) to CdS-NR(RF), lifetime of charge carriers is highly enhanced to 116 μs.

The average lifetime of order picoseconds and nanoseconds is attributed to band edge emission only. In our case, lifetime of CdS nanostructures is observed in the range of microseconds, thus, it is very difficult to conclude the luminescence originated due to band edge excitonic emission only. Hence, non-radiative trap state emission is another possibility [chapter 4, ref. 18,19]. Although having crystalline structure, CdS-NR(AC) exhibited much longer lifetime may be due to deeper/deepest traps, where excited electrons and holes trap prior to recombination. Our results are in accordance with few previous reports [12] that exhibited longer

lifetimes in case of Eu^{3+} doped $Cd_{1-x}Zn_xS$ NC. Similarly, decay times in microseconds for polyphosphate stabilized CdS nanoparticles have been also reported by Lakowicz group [13]. This delay in recombination of charge species may lead to exhibition of weak luminescence and as a result, higher photocatalytic activity by the photogenerated electrons and holes for oxidation and reduction reactions, respectively, could be expected.

5.3.3. Photocatalytic activity study

As investigated by time resolve spectroscopy and fluorescence emission study, that the recombination time of photogenerated charge carriers (e^-/h^+) are strongly influenced by their size, shape and crystallinity. Hence, electrons and holes can be effectively utilized for desire photoreduction and photooxidation processes by tuning the dimensional morphology of the catalyst. In this context, first oxidizing power of the valence band hole is comparatively studied for salicylic acid (SA) photooxidation by various CdS-NPs under UV light irradiation.

The time course of SA photooxidation curves in Fig. 8 shows that the concentration of SA decreases exponentially with irradiation time, indicating the apparent first-order kinetic law. The SA degradation rate gradually increases by the change in CdS morphology from spherical to rod shape NPs with increasing length and width of CdS-NR. Increased delocalization of electrons of rod shaped particles can lead to a remarkable decrease in e^-/h+ recombination probability [6,7] and hence, rapid oxidation of salicylic acid as compared with the rate of oxidation for spherical nanoparticles. Also, Au (1 wt%) photodeposition further improved the SA degradation rate because the photo induced electrons in the CdS NC migrate to the Au-NPs surface and effectively trapped at the Au–CdS interface and as a result strongly oxidizing h^+ could be available for photooxidation of salicylic acid effectively at a better rate.

Several photocatalytic degradation rates of many organics over illuminated TiO_2 fitted the Langmuir–Hinshelwood (L–H) kinetic [14,15] model: $r = -dC/dt = k(KC)/(1 + KC)$ where r is the initial rate of photocatalytic degradation (mol $l^{-1}min^{-1}$), C is the concentration of the reactant after the adsorption step (mol l^{-1}), t is the irradiation time (min), k is the rate constant and K the Langmuir–Hinshelwood adsorption constant. At low concentration, KC can be neglected with respect to 1 and one gets the simplified equation: $r = -dC/dt = kKC$ or $C/C_o = e^{-kKt} = e^{-kt}$ where k is the apparent rate constant of the pseudo-first order (min^{-1}) reaction. The rate constants of SA degradation after fitting into the curve have been found to be 3.56×10^{-6}, 3.64×10^{-5}, 3.79×10^{-5}, 8.63×10^{-4} and 11×10^{-4} min^{-1} for CdS-NS, CdS-NR(RF),CdS-NR(AC), Au deposited

CdS-NR(RF) and Au deposited CdS-NR(AC), respectively.

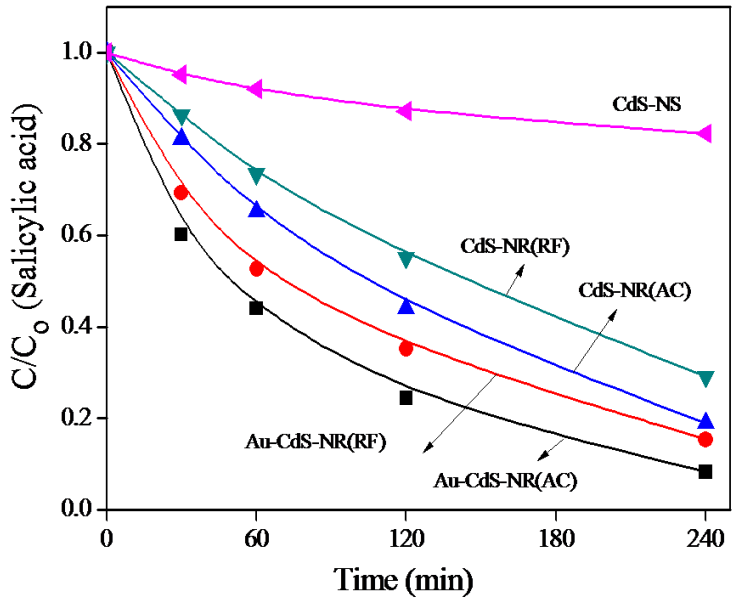

Fig. 8. Photooxidation of salicylic acid (0.5 mM) by different bare and 1 wt% Au loaded CdS nanorods.

The % conversion for spherical, high and low aspect ratio CdS-NPs has been found to be 17.8%, 71%, 81.2% for photooxidation of salicylic acid (0.5 mM). Generally, wurtzite phase of CdS is preferred over cubic phase for better PCA as reported for degradation dyes [16], benzaldehyde [chapter 1, ref. 68] and many other oxidation reactions [17,18] Hence, higher surface area, better surface structure and crystallinity and efficient delocalization of charge species to prevent e−/h+ recombination and longer lifetime seem to be responsible for superior photooxidation of salicylic acid by lengthy NR crystals.

The charge transfer at the Au–CdS interface was further investigated by fluorescence emission and photoactivity study as shown in Fig. 8. It has been found that fluorescence emission (Fig. 9a) and photoactivity for SA oxidation (Fig. 9b) with the CdS-NR(AC) gradually decreased and increased, respectively, with increasing amounts of Au-NS (separately prepared whose size is ~3.5 nm and Plasmon band = 540 nm) from 25 µl to 200 µl addition due to the formation of a large number of Au–CdS interface.

The 1 wt% Au (13×10^{19} atoms) deposited CdS-NR (dotted line) display almost same fluorescence emission and photoactivity as exhibited by 200 µl Au-NSs addition. It is interesting to know that effective amount of Au atoms (200 µl = 6×10^{16} = 0.04 wt% of CdS) required for

maximum photoactivity of CdS is *25 times less than 1 wt% Au deposited CdS photocatalyst*.

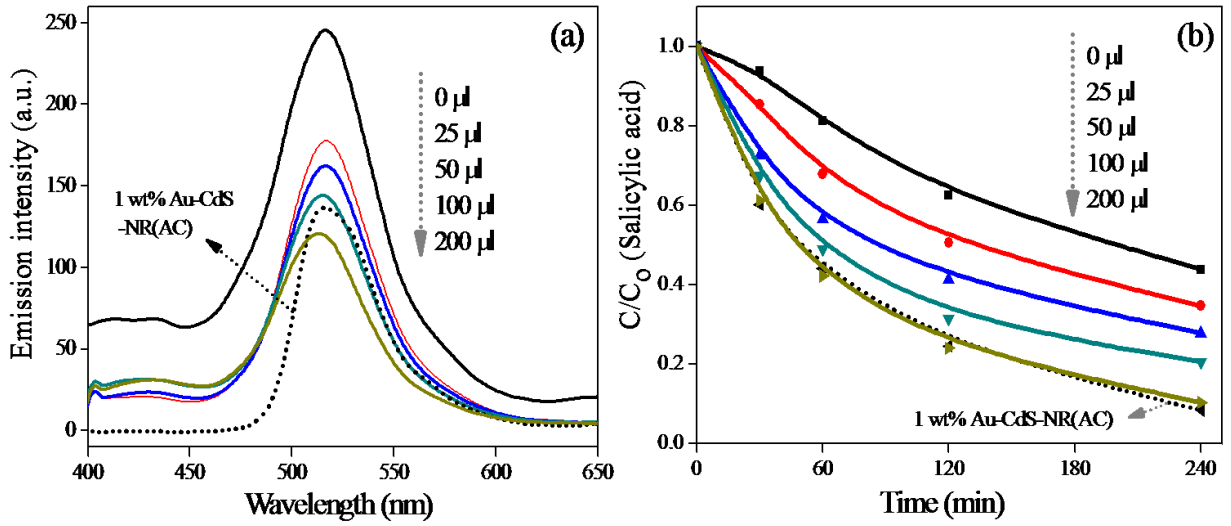

Fig. 9. Effect of amount of Au−nanospheres addition on the (a) emission intensity and (b) photocatalytic activity for salicylic acid degradation by CdS−NR(AC).

The efficiency of conduction band electron as a function of its relaxation time or stability is tested first time by the photoreduction of p-nitrophenol (PNP) to p-aminophenol (PAP) by CdS nanostructures under 2 h UV light irradiation (Fig. 10a). CdS-NS with cubic phase proved to be poor photocatalyst in comparison with hexagonal CdS-NR for photoreduction of PNP. The p-nitrophenol conversion was found to be notably enhanced as: 43.7% for CdS-NR(RF), 50% for CdS-NR(AC) nanorods and 62.5% after Au (1 wt%) loading as compared to 6.25% conversion by CdS-NS.

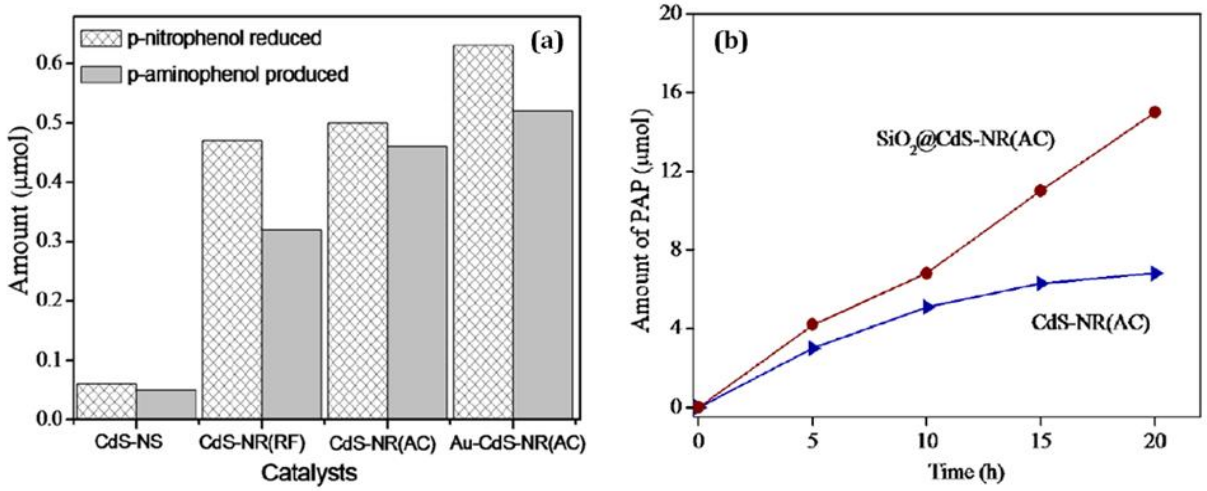

Fig. 10 (a) Photoreduction of p-nitrophenol by various catalyst, (b) stability test of CdS and SiO_2@CdS−NR(AC) by p−aminophenol formation on prolonged irradiation.

This enhancement can be reasonably explained on the basis of longer lifetime of photoexcited electrons, good crystallinity and better delocalization along the radial and longitudinal dimensions of CdS-NR nanostructures because the numbers of electrons are available for photoreduction of p-nitrophenol to p-aminophenol The similar photoreduction ability of nitrophenols (2-nitrophenol and 4-nitrophenol) on the modified-TiO_2 surface has also been found in several reports [19,20]. This result is also in good agreement with the enhanced photoactivity of CdS-NR for H_2 photoproduction.

It is well known that CdS undergoes photochemical dissolution and hence, the photoactivity deteriorates with light irradiation. A thin layer of silica over the CdS surface may prevent their photocorrosion and coalescence into larger particles, and increased the surface area of CdS for better adsorption and reactivity. Recently, Gupta and Pal [chapter 1, ref. 68] synthesized highly stable CdS-NR coated with a thin layer of silica (1–1.3 nm) for photooxidation of benzaldehyde.
In this context, stable photoactivity of SiO_2@CdS-NR(AC) relative to bare CdS-NR(AC) has been tested by reduction of p-nitrophenol (5 mM) under UV light (10.4 mW/cm^2) irradiation as shown in Fig. 10b. It has been observed that SiO_2 coating onto CdS-NR surface proved to be highly efficient to overcome the photodissolution of CdS. A linear increase in the p-aminophenol production (PAP) up to 10 h and thereafter the formation of PAP start decreasing by bare CdS, whereas SiO_2 coated CdS showed a steady increase in PAP production even up to 20 h irradiation light exposure because of the impairment of photostability of CdS-NPs by silica deposition.
The particle size, PL, surface area, %oxidation ability of salicylic acid and PNP of various CdS nanostructures are summarized in Table 1.

Catalyst	Particle size (nm)	Band gap (eV)	Fluorescence		Surface area (m^2/g)	Oxidation ability (%)	Reduction ability (%)
			Emission (λ_{ext} at 380 nm)	Decay time (μs)			
CdS-NS	D =10	2.77	486 (b) 526 (s)	20	19	17.8	6.25
CdS-NR (RF)	L =126 D =5.5	2.75	513 (b) 528 (s)	24	81	71	43.7
CdS-NR (AC)	L =170 D =10	2.73	516 (b) 528 (s)	116	76	81.2	50

In summary, the change in photoluminescence and photoredox ability of CdS nanostructures has been observed by correlation with a relaxation lifetime of photoexcited charge species.

5.4. References

[1] P.S. Chowdhury, P.Sen, A. Patra, Chem. Phys. Lett. 413 (2005) 311-314.

[2] A. Mclaren, T.V. Solis, G. Li, S.C. Tsang, J. Am. Chem. Soc. 131 (2009) 12540–12541.

[3] H.J. Yun, H. Lee, J.B. Joo, W. Kim, J. Yi, J. Phys. Chem. C 113 (2009) 3050–3055.

[4] J. Zhang, X. Zhang, J.Y. Zhang, J. Phys. Chem. C 113 (2009) 9512-9515.

[5] X. Wang, L. Qu, J. Zhang, X. Peng, M. Xiao, Nano Lett. 3 (2003) 1103-1106.

[6] S. Sadhu, A. Patra, J. Chem. Sci. 120 (2008) 1–8.

[7] R. Singh, B. Pal, Mater. Res. Bull. 48 (2013) 1403–1410.

[8] J. Zhang, X. Zhang, J.Y. Zhang, J. Phys. Chem. C 113 (2009) 9512–9515.

[9] M.B. Mohamed, C. Burda, M.A. El-Sayed, Nano Lett. 1 (2001) 589–593.

[10] P. Thakur, S.S. Joshi, S. Kapoor, T. Mukherjee, Langmuir 25 (2009) 6377–6384.

[11] H.S. Bhatti, K. Singh, N.K. Verma, J. Mater. Sci. Mater. Electron. 20 (2009) 255–259.

[12] K. Singh, S. Kumar, N.K. Verma, H.S. Bhatti, J. Nanopart. Res. 11 (2009) 1017–1021.

[13] J.R. Lakowicz, I. Gryczynski, Z. Gryczynski, C.J. Murphy, J. Phys. Chem. B 103 (1999) 7613–7620.

[14] D.G. Hela, D.A. Lambropoulov, I.K. Konstantinou, T.A. Albanis, Environ. Toxicol. Chem. 24 (2005) 1548-1556.

[15] I. Konstantinou, T. Sakellarides, V. Sakkas, T. Albanis, Environ. Sci. Technol. 35 (2001) 398–405.

[16] G. Lin, J. Zheng, R. Xu, J. Phys. Chem. C 112 (2008) 7363–7370.

[17] W.S. Chae, J.H. Ko, K.H. Choi, J.S. Jung, Y.R. Kim, J. Anal. Sci. Technol. 1 (2010) 25–29.

[18] M.Y. Han, W. Huang, C.H. Quek, L.M. Gan, C.H. Chew, G.Q. Xu, S.C. Ng, J. Mater. Res. 14 (1999) 2092–2095.

[19] S. Li, Fy. Zheng, Xl. Liu, F. Wu, Ns. Deng, Jh. Yang, Chemosphere 61 (2005) 589–594.

[20] X. Shen, L. Zhu, G. Liu, H. Yu, H. Tang, Environ. Sci. Technol. 42 (2008) 1687–1692.

Chapter 6: Highly Enhanced Photocatalytic Activity of Au Nanorod–CdS Nanorod Heterocomposites

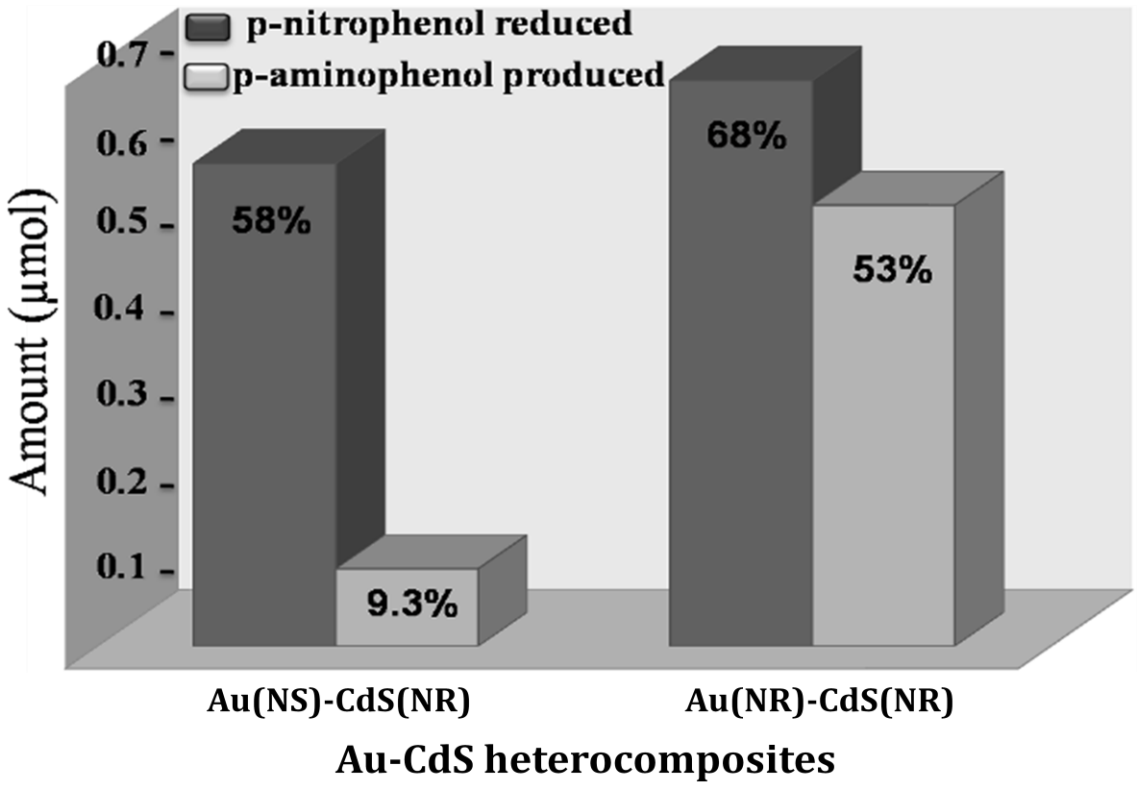

6.1. Introduction

Chapter 1 discussed the importance of metal (M)–semiconductor (SC) interface, which provides a unique pathway for transfer of photogenerated electrons in numerous applications [1-5]. Charge transport at the M–SC interfaces strongly depends upon the contact area, work functions (ϕ), Fermi level positions and their reduction potential values [6,7]. It is well known that electrons will flow from SC to M side through a barrier called the Schottky barrier until Fermi levels of M and SC are energetically aligned at the same level [8]. Consequently, interfacial properties can be modulated by tuning the size and shape of M and SC, and adsorbed electrolyte, the shift in band edge, barrier height and space charge layer, are strongly depended the energetics of M–SC interfacial area.

Various techniques such as photodeposition, spin-coating, impregnation and co-precipitation have been employed to deposit M islands onto SC surface for making M–SC composites [9,10]. The uncontrolled distribution of M-NPs during metal photodeposition technique can limit their efficiency because most of them get aggregated onto the SC surface [11] and results in improper alignment of M–SC arrays. On the other hand, separately prepared NPs of different shapes of M and SC can also be self-assembled by surface linking agent or by impregnation–deposition. Quantification of the rate and degree of delocalization across the M–SC and SC–SC interface is an essential factor in terms of rapid charge separation. For better charge rectification, rod-shaped morphology of Au, Ag, Pt, TiO_2, CdS, and ZnS, etc. NPs have been extensively investigated in recent years as it is already proved, delocalization along the elongated side of cylindrical symmetry, makes it much more photoresponsive against recombination [12,13] of charge carriers (e^-/h^+).

Regarding this, several SC–SC composites of CdSe–ZnSe, ZnSe–CdS, CdSe–CdS, CdSe–CdTe have been demonstrated [13-15] in recent years as potential candidates for benign energy conversions. The ability to selectively build metal–semiconductor heterostructure with several morphologies and spatial relationships between their individual components could be used for direct energy flows at the nanoscale interface. The noble M–SC composites are also studied by considering M-NS–SC-NS [5,16] and M-NS–SC-NR alignment [17,18] for the improved photochemical activity in many instances. However, the photosensitivity of irradiated M-NR–SC-NS and M-NR–SC-NR junctions are rarely investigated despite of longer lifetime and better delocalization of photoexcited charge species along the length of both NR and some

other beneficial advantages. As the Fermi level equilibrium takes place quickly and rapid in Au-CdS composites (lower Fermi energetic level (+0.5 V versus NHE) than the conduction band of CdS (−1.0 V versus NHE)), hence the instant electron transfer from CdS to Au-NPs occurs. It is expected that the double rectification (lengthy CdS-NR + lengthy Au-NR) of charge species at the Au-NR–CdS-NR nanojunctions with the larger interface area may yield optimum PCA.

Herein, various M–SC heterojunctions are prepared either by simple mixing or impregnation of spherical and rod-shaped Au and CdS-NPs and demonstrated the effects of different M–SC interfaces namely, Au-NS–CdS-NS, Au-NR–CdS-NS, Au-NR–CdS-NS and Au-NR–CdS-NR onto the photoluminescence, electrical and photocatalytic properties.

6.2. Experimental details

6.2.1. Preparation of CdS and Au nanoparticles of different shapes

CdS-NPs with spherical and rod-like morphologies, were detailed in *section- 2.2.1 and 2.2.2 of chapter 2*. Au-NPs with spherical and rod-like shape were synthesized as *mentioned in chapter 2, section- 2.2.7*.

6.2.2. Preparation of Au–CdS junctions

As synthesized Au and CdS NPs having spherical as well as nanorod shape is assembled by mixing of their aqueous suspension and or by the impregnation method as given in detailed in *section- 2.2.8 of chapter 2.*

6.2.3. Photocatalytic reaction

The photocatalytic activity of various M–SC composite sample was evaluated for the photooxidation of 5 ml salicylic acid (0.5 mM) and reduction of p-nitrophenol (0.2 mM) in a test tube containing 10 mg CdS and varying amount of Au nanoparticles {10 (2.99×10^{15} atoms) – 200 µl Au (5.99×10^{16} atoms} assembled by direct addition or pre-impregnated under UV light (125 W Hg arc, 10.4 mW/cm^2) and sunlight (intensity 40 mW/cm^2) irradiation. The suspensions were magnetically stirred in the dark for 30 min to ensure the establishment of an adsorption/desorption equilibrium. The reaction samples were analyzed by UV–vis spectrophotometer after filtration with 0.22 µm cellulose filter. Photoreduction of p-nitrophenol (5 ml, 0.2 mM) with impregnated samples has been carried out under UV light irradiation for 1 h and analyzed by HPLC, 220 nm, using C-18 column and MeOH: H_2O (35:65) as mobile phase at a flow rate of 1 ml min^{-1}.

6.2.4. Characterizations

Sophisticated instruments such as UV-vis, PL, XRD, TEM, and SAED were employed to characterize these Au-CdS assembled samples. Time resolved luminescence spectra and current-voltage (I-V) characteristics were also investigated.

6.3. Results and discussion

6.3.1. Absorption study of Au–CdS nanocomposites

Fig.1 shows the surface Plasmon (SP) band at 530 nm for Au-NS (9.1 nm), transverse (TSP) and longitudinal SP band (LSP) at 535 and 657 nm, respectively, for Au-NR (20 nm × 8.6 nm), the absorption onset at 470 nm for CdS-NS and 518 nm for CdS-NR.

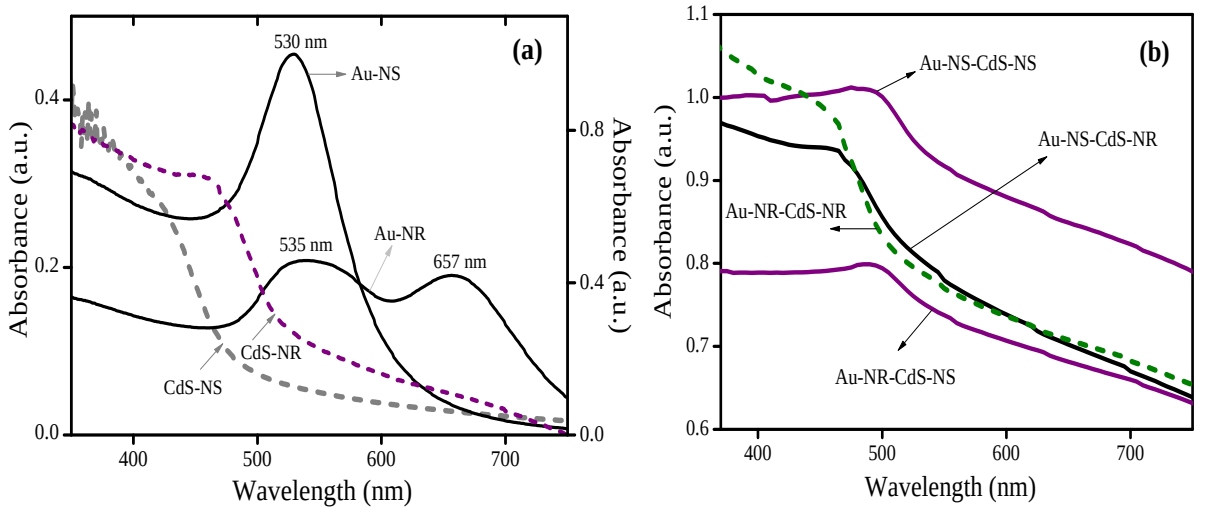

Fig. 1. Absorption spectra of (a) aqueous suspension of Au (solid line) and CdS (powder, dotted line) nanoparticles, and (b) Au loaded CdS nanoparticles (powder) of different shapes.

However, after impregnation of Au and CdS NPs of different shapes, the absorption bands of Au-NS–CdS-NS, Au-NR–CdS-NS, Au-NS–CdS-NR and Au-NR–CdS-NR heterocomposites did not exhibit any SP band due to Au deposition because of the strong CdS exciton–Au plasma interactions or coupling at the mixed phase junction [19,20]. Associated mixing of electronic states through the overlapping of electronic wave functions of Au and CdS led to a change in the density of states in both the components resulted to form a new energetic interface. Consequently, suppression in the quantum confinement of CdS-NR and SP of Au have been observed due to the lattice matching of impregnated (Au-NS–CdS-NR, Au-NR–CdS-NR) samples.

In order to minutely distinguish the changes in absorption processes, second derivatives of the absorption spectra's of Au–CdS impregnated heterocomposites was taken for precise calculations of band gap energy as shown in Fig. 2.

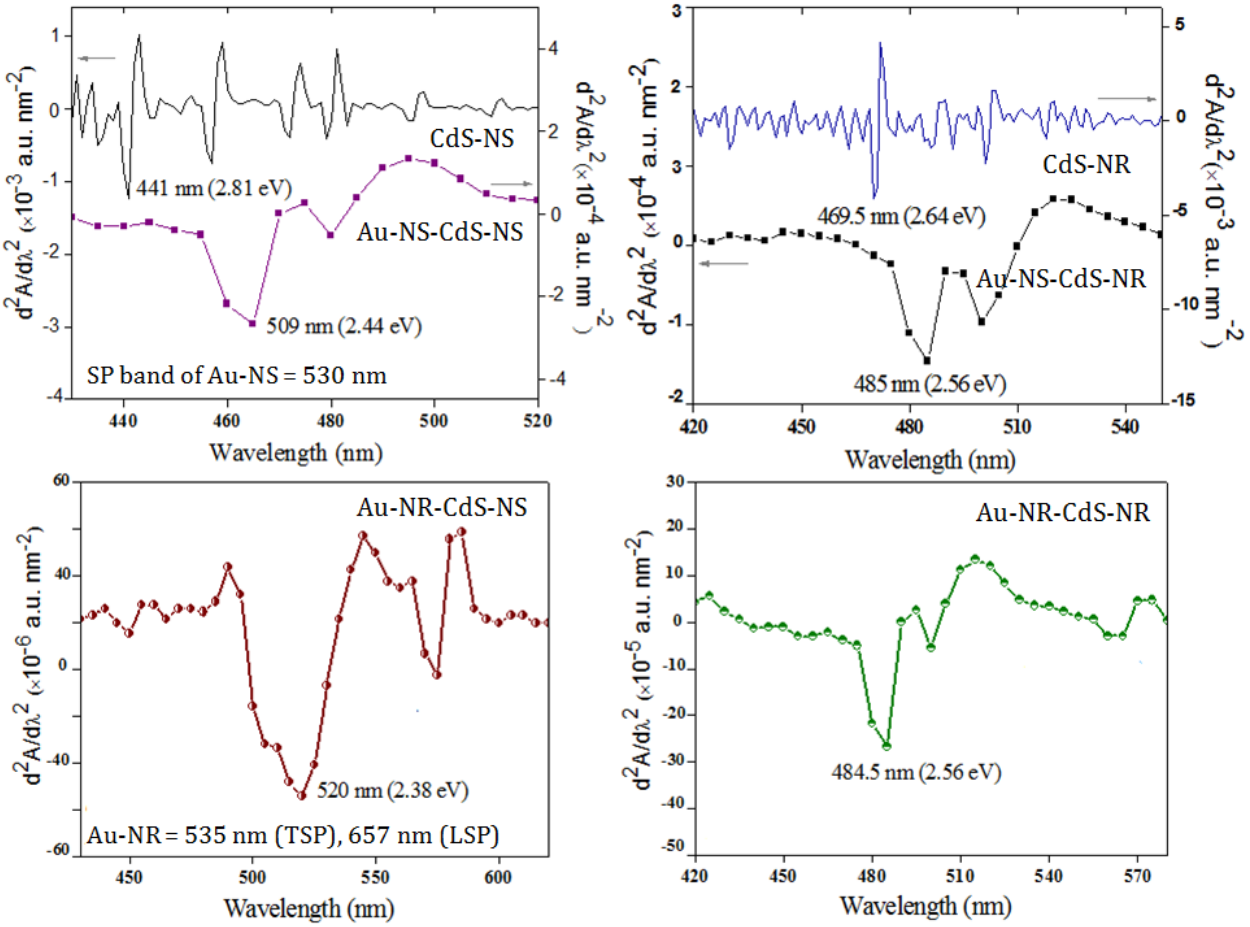

Fig. 2. Second derivatives of absorption spectra of various bare CdS and impregnated Au–CdS nanocomposites. *Inset:* surface plasmon bands of Au nanosphere and nanorods are written.

The absorption at 441 nm (2.81 eV) for CdS-NS and at 469.5 nm (2.64 eV) for CdS-NR was found to be significantly red-shifted to 509 nm (2.44 eV) and 485 nm (2.56 eV), respectively, after impregnation with Au nanospheres, i.e., for Au-NS–CdS-NS, Au-NS–CdS-NR composites. Similar red-shifted absorption bands at 520 nm (2.38 eV) for Au-NR–CdS-NS and 485.5 nm (2.56 eV) for Au-NR–CdS-NR hybrid junctions as compared to respective bare components have been also noticed after Au-NR impregnation because of the mixing of delocalized Plasma electrons into a large portion of CdS nanostructures.

Spherical CdS-NPs of size 10–12 nm and crystalline CdS-NR of dimensions 115–130 nm in length and 5–7 nm in width is shown in the TEM images of Fig. 2a and b–c. Fig. 2d

representing the selected area diffraction pattern with bright concentric diffraction rings characteristic of the hexagonal crystal phase of CdS nanorod having superior crystallinity.

6.3.2. Morphological study

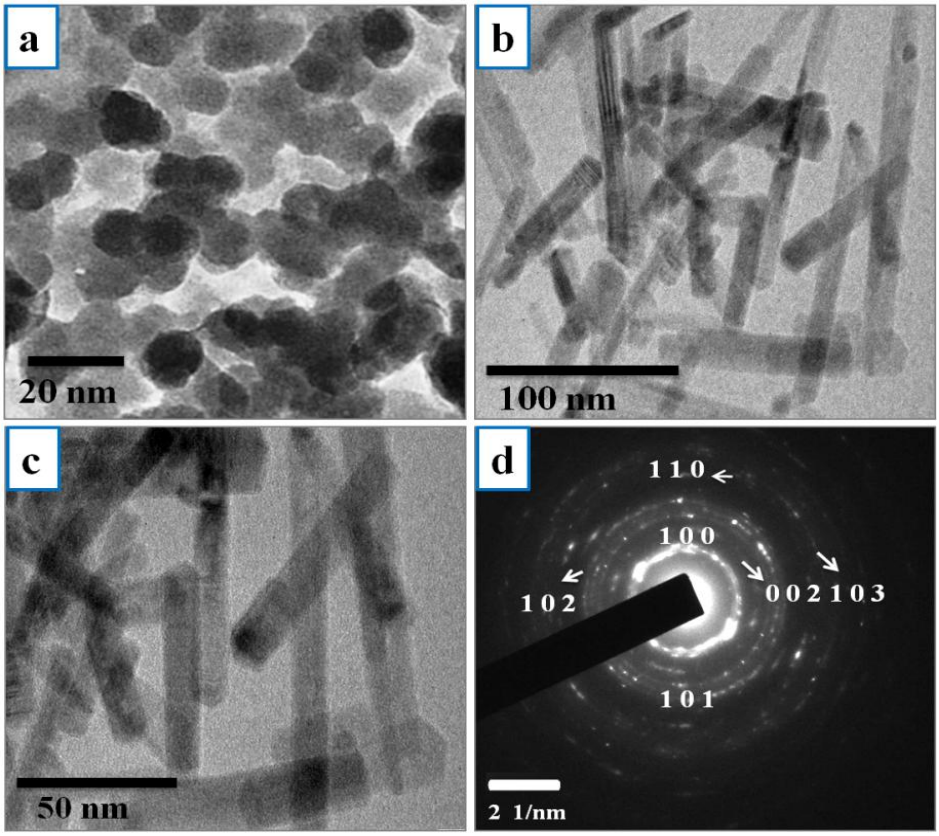

Fig. 3. TEM images of CdS (a) nanospheres, (b and c) nanorods and corresponding (d) SAED pattern.

As-synthesized spherical and rod like Au-NPs of sizes around 9.1 nm and 20 nm × 8.6 nm (L × W), respectively, have also seen in Fig. 4a and b. The obtained dimensions of Au NPs are in good conformity with their observed SP bands in Fig. 1a. In Au and CdS impregnated samples; parallel attachment of relatively lengthy CdS-NR with a smaller Au-NR with a better contrast (more black color Au than CdS) are observed in the TEM images of Fig. 4c. As shown in Fig. 5a, many Au-NR like particles are attached to CdS-NR (back to back) as indicated by red arrows. Pictorial representation of the plausible attachments (light blue; CdS-NR and black; Au-NR) has been drawn to better illustrate the TEM images. Au-NR decorated on the tip of the CdS surface (Fig. 5b) was also found, probably due to one S^{2-} rich end of NR (other end is Cd^{2+} rich) allows the Au-NR to access the surface.

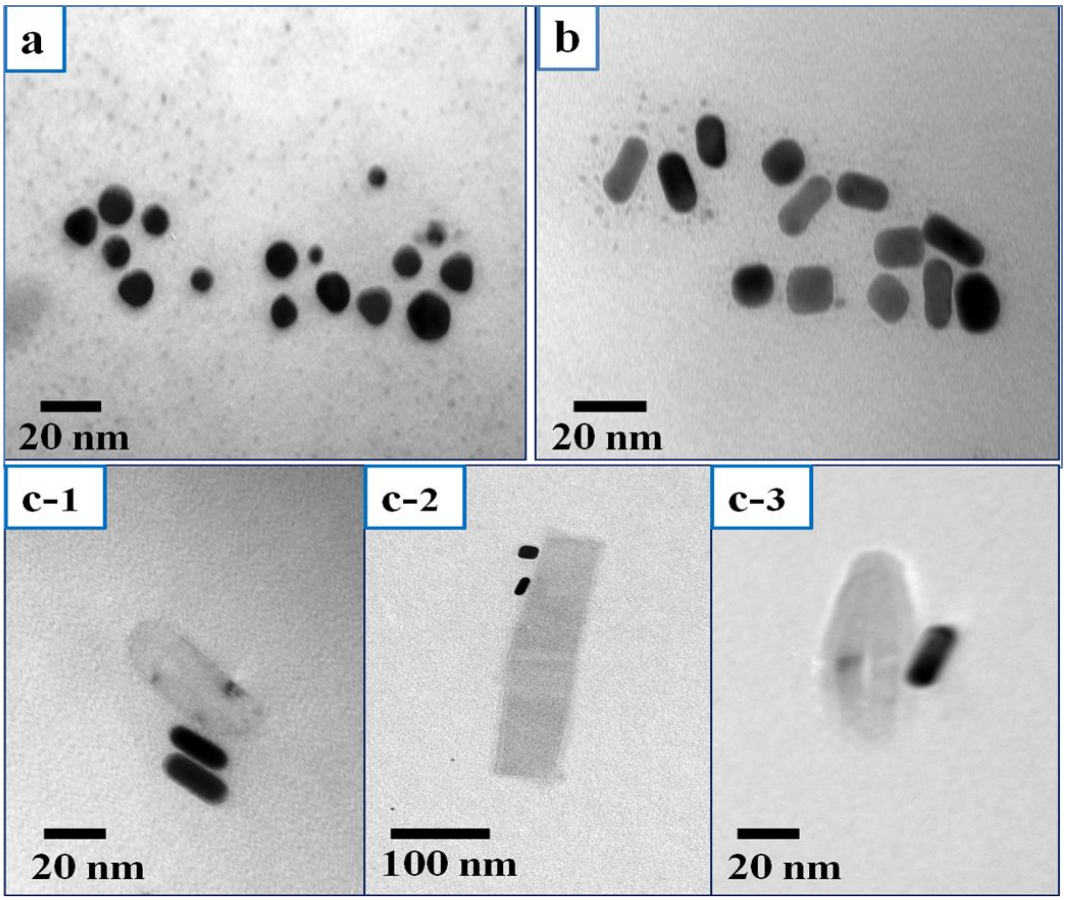

Fig. 4. TEM images of (a) Au nanospheres, (b) Au nanorods, c (1–3) parallel attachments of Au nanorod and CdS nanorod arrays.

Similarly, Au–CdS attachments have been also observed as shown in TEM Images Fig. 5(c-f). Briefly, S^{2-}, rich CdS-NR surface with many negative dangling bonds [21,22] actively and effectively initiate nucleation from the cationic gold precursor to form Au-S bonds, which have very high bond enthalpies (a diatomic bond enthalpy of 418 kJ/mol) and a very high affinity, which seems to be a cause for the attachment of Au nanostructures with the CdS surface.

Yang et al. reported that the strong chemisorptions between thiolate and Au enable the nucleation of Au NC directly onto the CdS-NR. As our synthesis route carried out without the use of any surface modifier, probably Vander Waals forces exist between positively charged CdS surface and negatively charged $AuCl^{4-}$ ions as suggested by Zhao Hui et al [23].

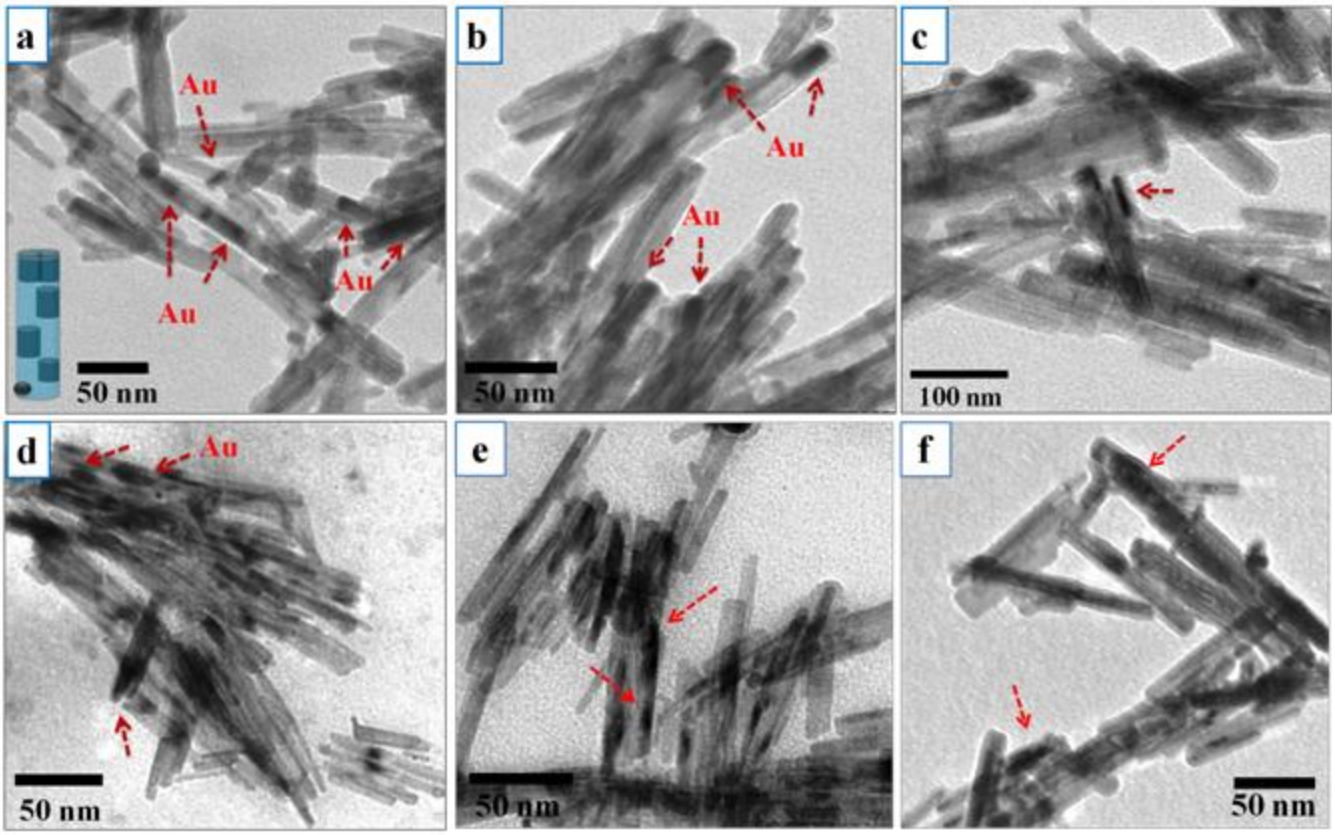

Fig. 5. Overlook of (a) back-to-back, (b) tip, and (c-f) sidewise attachment of Au nanorods and CdS nanorods (inset in 5a is pictorial representation of possible attachments of Au nanorod (black) to CdS nanorod (light blue)).

6.3.3. Photoluminescence spectroscopy

Photoluminescence (PL) (λ_{ext} = 380 nm) of CdS-NR dispersed in acetone (1 mg/ml) was gradually quenched in a different extent by the addition of 10–200 µl of both Au-NS and NR as seen in Fig. 6a and b. The change in behavior of PL by CdS-NR by the addition of both Au-NS and NR is depicted in the scheme.

With the increasing amount of Au-NPs loading over CdS-NR surface, a large number of Au–CdS interfaces led to quick charge transfer from CdS (SC) to Au (M) side and thereby, quenched the PL intensity of CdS-NR. Bare CdS-NR displayed band edge emission at 520 nm due to thermally de-trapped electrons with holes and the addition of the same amount (10 and 200 µl) of Au-NR aqueous dispersion to CdS-NR suspension, notably quenched the luminescence intensity as compared to Au-NS loading onto the same amount of CdS-NR. The difference in luminescence intensity by 10 µl (2.99×10^{15} atoms ~0.002%) to 200 µl (5.99 ×

10^{16} atoms ~0.04%) of Au-NS and Au-NR with an increased number of Au atoms are shown in Fig. 6c.

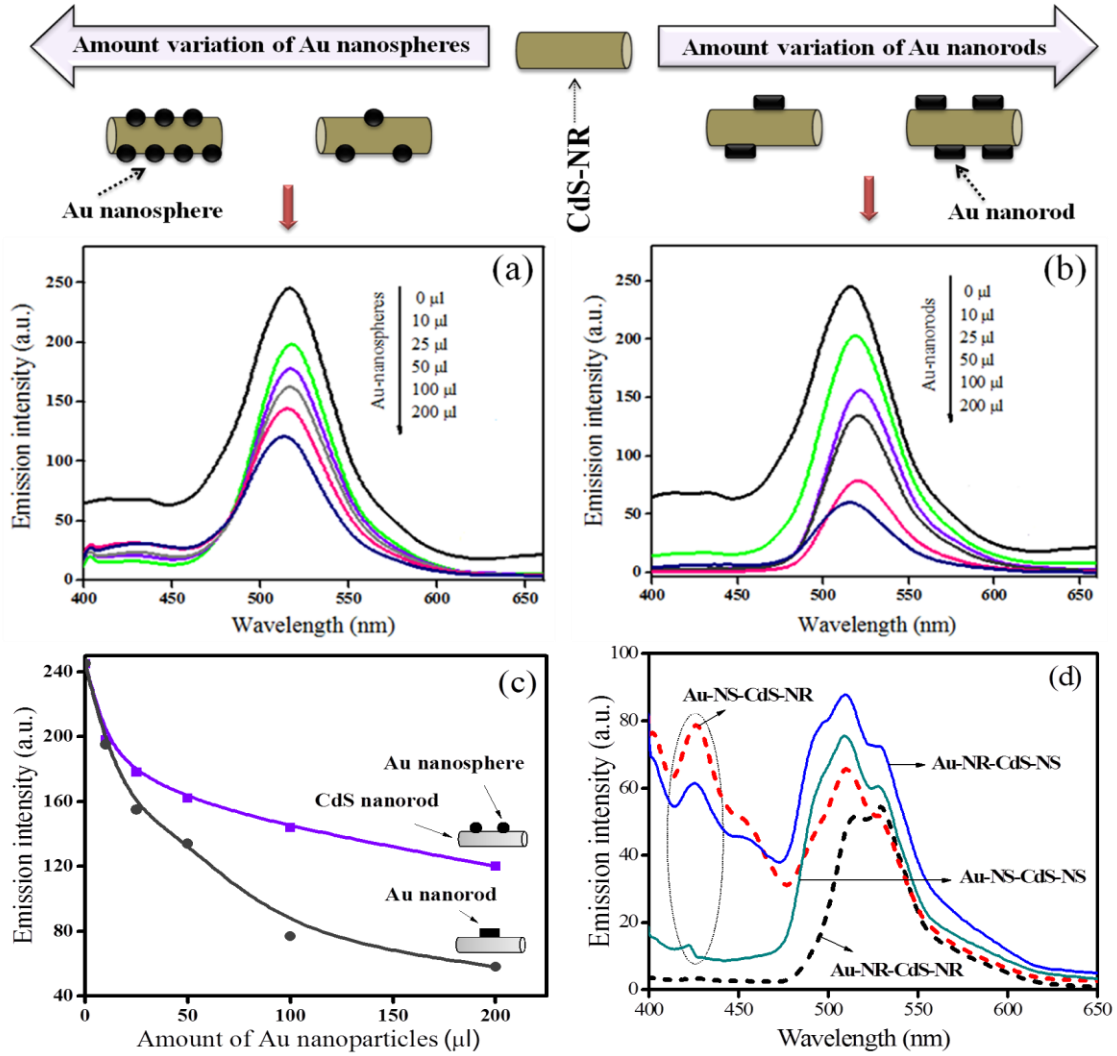

Fig. 6. (a) Changes in photoluminescence of CdS nanorods during loading of varying amount of Au (a) nanospheres, (b) nanorods as depicted in the above *scheme*, (c) relative changes in the luminescence intensity of CdS nanorods, and (d) change in photoluminescence after impregnation of Au–CdS samples

512 µl Au solution (0.01M, $HAuCl_4$) contains	0.98 mg Au
10 ml (10,000 µl) of Au NPs solution contains	0.98 mg Au
1 µl Au NPs contains	0.98×10^{-4} mg Au
1 µl Au NPs contains	2.996×10^{14} atoms
10 µl Au NPs contains	2.996×10^{15} atoms
25 µl Au NPs contains	7.489×10^{15} atoms
50 µl Au NPs contains	1.497×10^{16} atoms
100 µl Au NPs contains	2.996×10^{16} atoms

The Au-NR–CdS-NR interfaces always quenched the CdS emission to a larger extent than Au-NS–CdS-NR junction, despite having the same amount of Au loading. The larger contact area developed by Au-NR and CdS-NR (as shown on the schematic), results in rapid delocalization of photoexcited charge carriers who helps in the retardation of recombination rate. The same behavior of PL quenching is also observed in case of Au-NS–CdS-NS, Au-NR–CdS-NS, Au-NS–CdS-NR and Au-NR–CdS-NR composites obtained by impregnation of 10 µl Au-NPs and 10 mg CdS-NPs of different shapes. Fig. 6d evidencing that PL intensity (~75 a.u.) is notably reduced in each Au–CdS impregnated nanostructures compared to bare CdS-NR (PL intensity ca. 250 a.u.). It is important to note that PL quenching is observed to be higher in impregnated samples than the direct addition of Au atoms to the CdS suspension. A relatively intense characteristic PL band at 430 nm for Au-NS–CdS-NR and Au-NR–CdS-NS interfaces corresponding to the presence of Au, almost disappeared in case of Au-NR–CdS-NR heterocomposites. Again, the Au-NR–CdS-NR impregnated sample exhibited least PL intensity with a red shift of 6 nm in band edge emission relative to other three different Au–CdS interfaces. This fact confirms that photoexcited charge transfer process between CdS and Au NR is much more sensitive due to larger per particle surface area, interfacial area and better delocalization of charge species along the length of both the M and SC NR [24].

6.3.4. Time resolved spectroscopy

The observed asymmetry in absorption and PL behavior due to the charge separation and a recombination lifetime of four different Au–CdS interfaces has been further investigated by Time Resolved Luminescence Decay spectra. Emission decay curves are obtained by exposing samples (50 mg – solid paste) by N_2 laser at 490 nm excitation as shown in Fig. 7a. The average lifetime τ_{av}, of photogenerated e^-/h^+ pairs are found to be 2.7 µs, 12.5 µs and 34 µs for CdS-NR, Au-NS–CdS-NR and Au-NR–CdS-NR interface, respectively. Thus, Au loading notably prolonging the lifetime of charge carriers and thereby, increased the relaxation time of charge

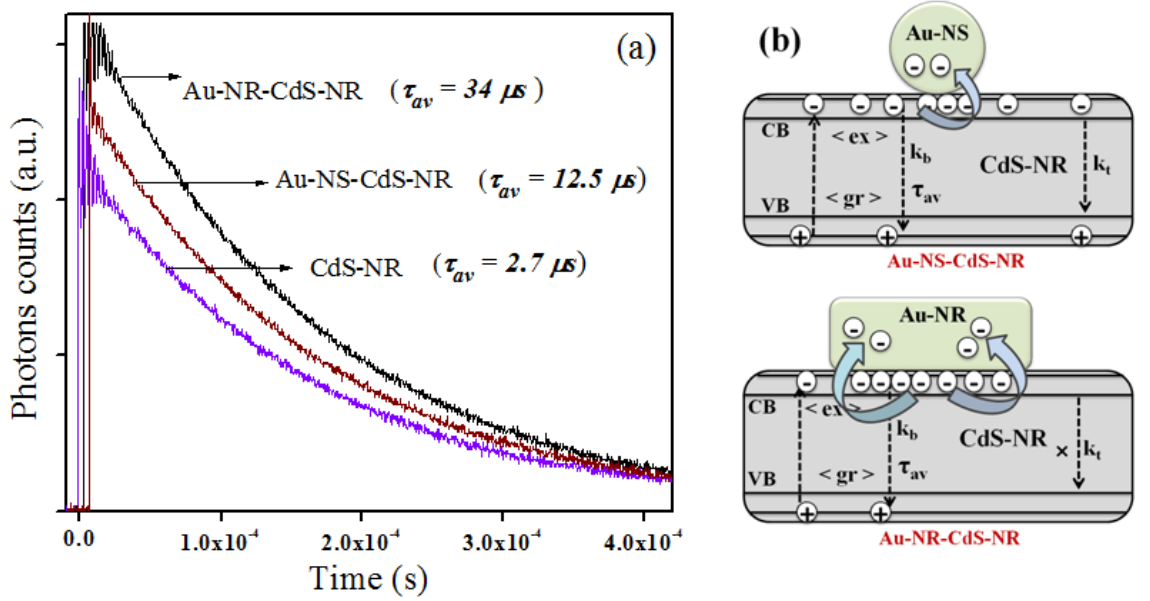

Fig. 7. (a) Time resolved emission decay curves of different Au–CdS interfaces, and (b) a *Schematic* of carrier relaxation processes in Au–CdS nanocomposites as a function of their interface contact area (where <ex>, <gr>, k_b, and k_t represent the excited state, ground state, rate due to radiative recombination, and rate due to trapping state).

species of CdS-NR. Larger interfacial contact area of Au-NR–CdS-NR than Au-NS–CdS-NR interface, effectively sink out a large number of electrons from the photoirradiated CdS surface significantly retard the electron–hole recombination, hence, reducing the PL intensity as per the scheme of Fig. 7b.

6.3.5. Structural properties of Au–CdS nanocomposites

The XRD patterns of CdS and Au–CdS samples are shown in Fig. 8. All of these diffraction patterns are similar and strongly indexed to hexagonal (wurtzite) crystal structure of CdS with lattice parameters (a = b = 4.042˚A, and c = 6.741˚A) which are in good agreement with JCPDS No. 41-1049 data card.

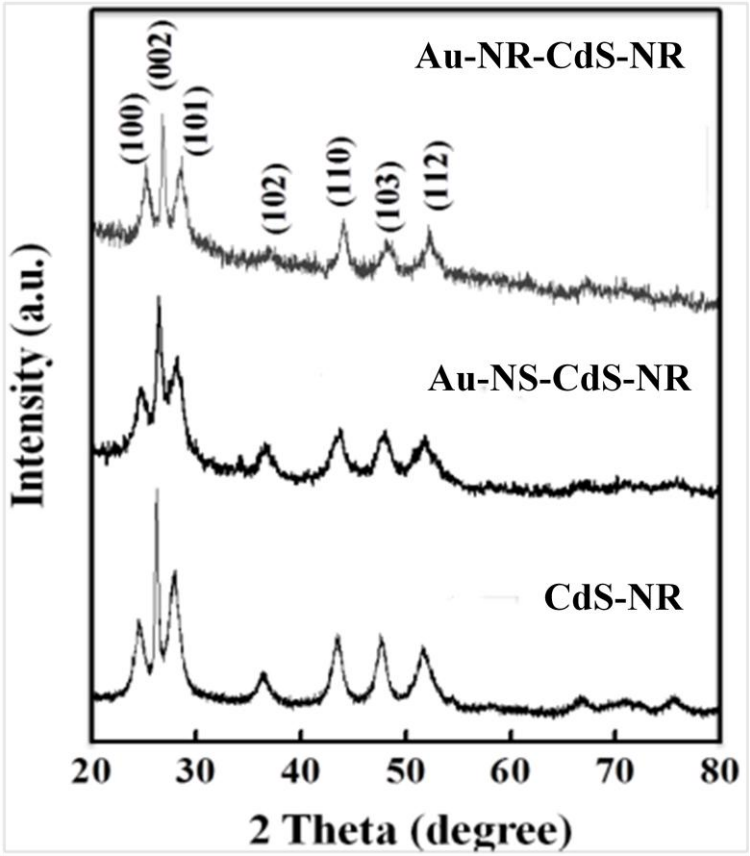

Fig. 8. X-ray diffraction patterns and various colors of CdS and impregnated Au-CdS samples.

No additional peaks of impurities were detected, indicating the high purity of synthesized products. Notably, the peak intensity of Au/CdS composites samples decreased slightly, probably due to the suppression of electron scattering of CdS by heavier Au metal attached to the CdS surface. The sharpening of the (002) diffraction peak in the XRD pattern indicates that the NR have grown along the crystallographic c-direction [25]. The measured d_{hkl} values of the respective diffraction planes; 0.36 nm (100), 0.33 nm (002), 0.314 nm (101), 0.25 nm (102), 0.2 nm (110) and 0.17 nm (112) have consistently been matched with the SAED pattern shown above in Fig. 3d.

6.3.6. Current–voltage characteristics

The collective nonlinear current–voltage (I–V) characteristics of the bare and Au–CdS heterojunctions are shown in Fig. 9.

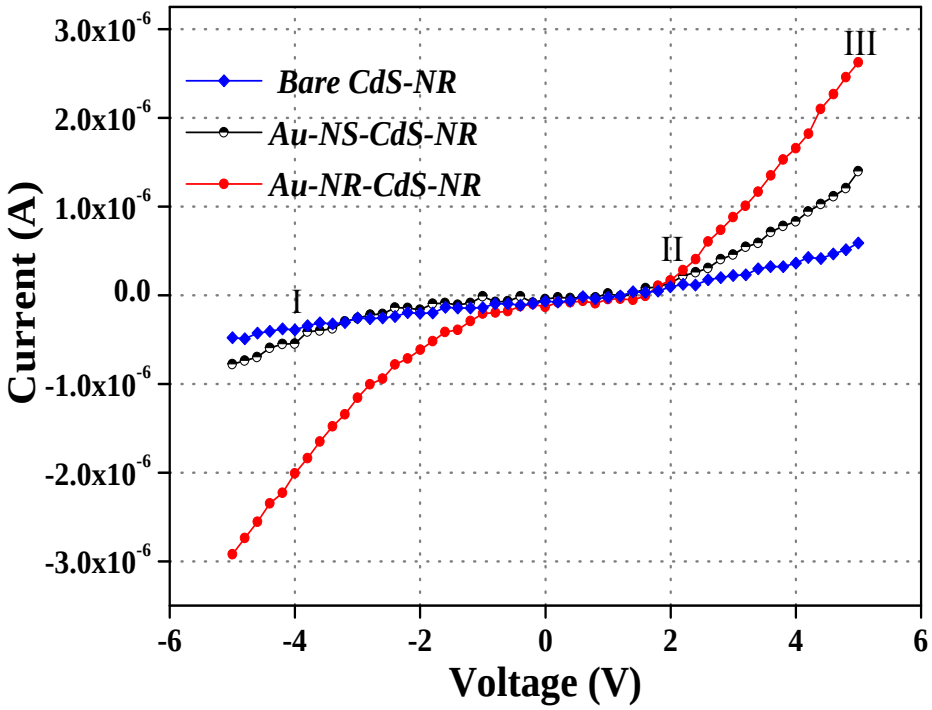

Fig. 9. Collective two terminal I–V characteristic curves of bare CdS and Au-CdS nanojunctions at room temperature.

The observed nonlinearity in I–V characteristics are caused by the Schottky barriers formed between the M and SC at the metal/semiconductor interface [28]. As shown in the figure, bare CdS-NR, Au-NS–CdS-NR, and Au-NR–CdS-NR, respectively, show rectifying and asymmetric behavior with respect to zero bias (do not obey the Ohm's law) and Au-NR–CdS-NR composite interface displayed a significant change in current–voltage (I–V) properties as compared to other Au–CdS arrays.

On applying a large voltage the current flowing through the heterojunctions are sufficiently large and, therefore, corresponding I–V curve approaches a straight line with a slope equal to the resistance of the heterojunctions. This resistance was determined using the differential voltage method at large bias I–V curve as R = dV/dI where R is resistance, dV/dI differential voltage, this procedure gives resistances as 8.4, 3.6 and 1.89 MΩ (at voltage = 5.0 V) and corresponding conductance values 1.2×10^{-7}, 2.8×10^{-7} and 5.3×10^{-7} S for bare, Au-NS–CdS-NR, and Au-

NR–CdS-NR nanocomposites, respectively. I–V curve can be divided into three different segments, i.e., I, II, and III and corresponding to these three segments, the voltage (V), current (I), resistance (R) and conductance (S) are calculated. The increase in conductance in Au-NR–CdS-NR composites in comparison to Au-NS–CdS-NR and bare CdS well justified the role of interface area for conduction developed by formation of Schottky barriers between Au–CdS components.

Table 1. The measurement of voltage (V), current (I), resistance (R), and conductance (S), corresponding to segments I, II, III of I–V characteristics.

Sample	Region	Voltage (V)	Current (nA)	Resistance (MΩ)	Conductance (S) × 10^{-7}
CdS-NR	I	-4.0	-354	11.3	0.88
	II	2.0	92.1	21.7	0.45
	III	5.0	598	8.4	1.2
Au-NS-CdS-NR	I	-4.0	-535	7.5	1.3
	II	2.0	170	12.0	0.83
	III	5.0	1400	3.6	2.8
Au-NR-CdS-NR	I	-4.0	-2000	2.0	5.0
	II	2.0	196	10.0	1.0
	III	5.0	264	1.89	5.3

6.3.7. Photocatalytic activity

The observed variation in recombination time of photoexcited charge species of the different Au–CdS interface is further reflected by the photoinduced reactions such as photocatalytic oxidation of salicylic acid and reduction of p-nitrophenol (PNP). The photooxidation of SA by bare and Au nanosphere (10 µl = 2.99×10^{15} atoms) loaded CdS (10 mg) nanospheres, i.e., Au-NS–CdS-NS do not show any notable changes in the SA concentration and bare CdS-NR displayed high (62%) degradation efficiency during 4 h of UV irradiation.

However, the same amount of Au-NS loading onto CdS-NR; Au-NS–CdS-NR, highly improved the SA degradation rate ca. 76% relative to 12% by Au-NS–CdS-NS interface. SA degradation is found to be highest ca. 86% in case of Au-NR–CdS-NR heterocomposites because of the rapid charge transfer process at their interface.

Several experimental results have indicated that photocatalytic degradation of pollutant/pesticides over illuminated TiO_2 follow the pseudo first order kinetics, a simplified form of Langmuir–Hinshelwood (L–H) kinetic model at low concentration. A linear relation

between $-\ln C/C_o$ and irradiation time (t), i.e., $-\ln C/C_o = k_{obs}$ indicating the pseudo first order reaction of SA photodegradation as found in Fig. 10a, where Co is the initial concentration, C is the concentration after irradiation time t and k is the observed rate constant.

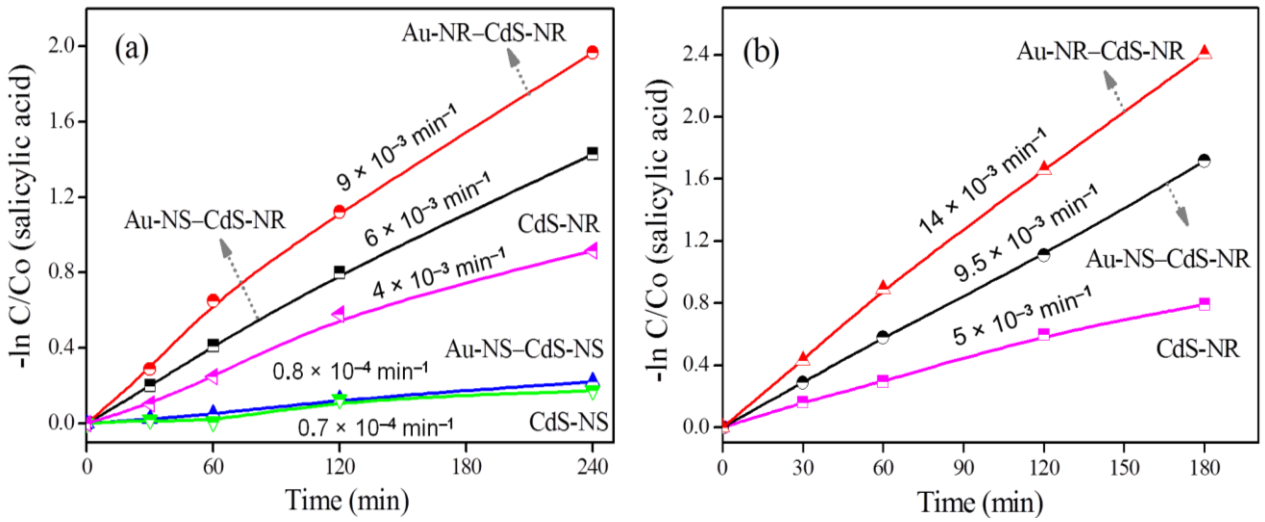

Fig. 10. Change in concentration of salicylic acid (-ln C/Co) as a function of time (t) for various bare and Au–CdS nanojunctions under (a) UV light and (b) direct sunlight irradiation.

The rate constants of SA degradation have been found (Fig. 10a) to be 0.7×10^{-4}, 0.8×10^{-4}, 4×10^{-3}, 6×10^{-3} and 9×10^{-3} min^{-1} for bare CdS-NS, Au-NS–CdS-NS, bare CdS-NR, Au-NS–CdS-NR and Au-NR–CdS-NR, respectively. As the band gap (2.5–2.8 eV) of CdS lies in the visible region, CdS-NR exhibits high photoactivity (66% and $k = 5 \times 10^{-3} min^{-1}$) and Au-NR–CdS-NR interface further significantly improved (88% and $k = 14 \times 10^{-3}$ min^{-1}) the SA photooxidation as compared to 78% by Au-NS–CdS-NR composite ($k = 9.5 \times 10^{-3}$ min^{-1}) under direct sunlight (40 mW/cm^2) illumination for 3 h. The corresponding rate constants have been found (Fig. 10b) to be gradually increased in the order: 5×10^{-3}, 9.5×10^{-3} and 14×10^{-3} min^{-1} for bare CdS-NR, Au-NS–CdS-NR and Au-NR–CdS-NR, respectively.

6.3.7.1. Recyclability test

The stability of Au–CdS impregnated catalysts (25 mg) com-pared to bare CdS-NR was tested by photodegradation of salicylic acid (5 ml, 0.5 mM) for the three recycles under UV light irradiation of 2 h as shown in Fig. 11. CdS, being photocorrosive in nature, deteriorate the SA photoactivity up to 21.7% after 3 cycles due to its photochemical dissolution with light irradiation. In contrast, Au-NS–CdS-NR and Au-NR–CdS-NR catalysts decompose SA

effectively without significant deactivation even after three times recycling. The slight decrease (1–4%) in the efficiency of Au/CdS composites after 3 recycles may come from the residual contamination on the surface of the catalyst.

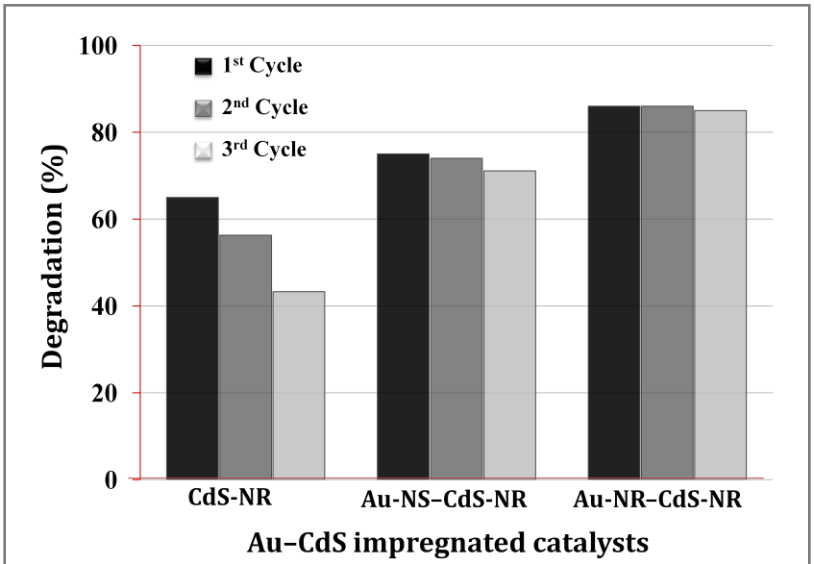

Fig. 11. (a) Degradation (%) of salicylic acid (0.5 mM, 5 mL) after recycling with bare CdS and Au-CdS composites (25 mg) under UV light irradiation of 2 h.

Hence, Au–CdS heterocomposites (especially Au-NR–CdS-NR; only 1% loss) interface facilitates the promotion of charge carriers, thus improved the activity and stability of CdS.

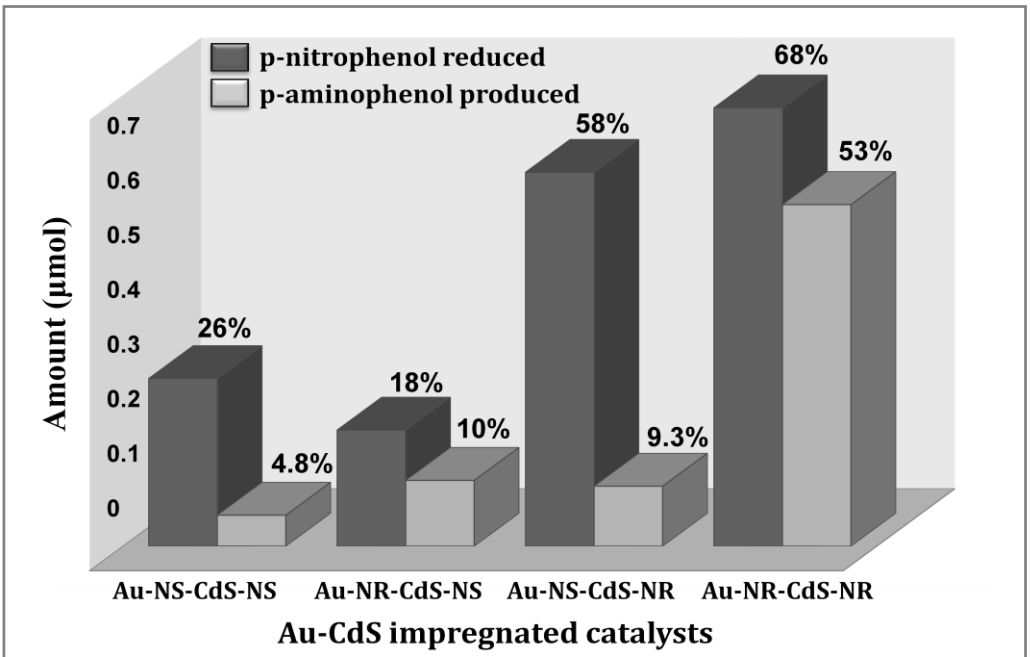

Fig. 12. Photocatalytic reduction of p–nitrophenol (0.2 mM) to p–aminophenol by various Au–CdS impregnated catalysts.

Similarly photocatalytic reduction of p-nitrophenol (0.2 mM) to p-aminophenol by various Au–CdS impregnated composites during1 h UV irradiation is seen in Fig. 12.

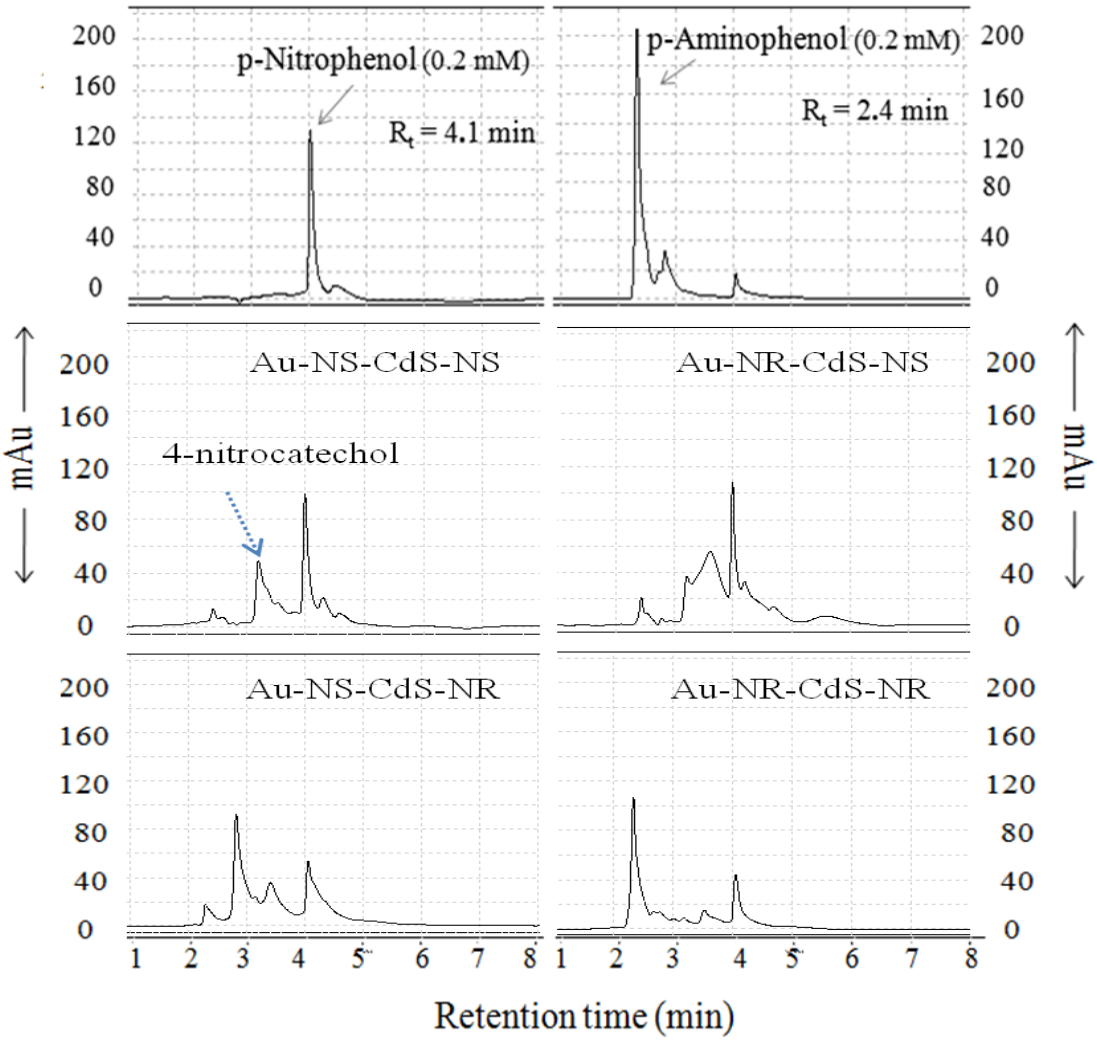

Fig. 13. HPLC chromatograms of p–nitrophenol solution (0.2 mM) after 1 h irradiation with UV light using various impregnated Au–CdS catalysts.

The amount of PNP reduced is quite higher (58% and 68%) in case of Au-NS–CdS-NR and Au-NR–CdS-NR arrays relative to 26% and 18%for Au-NS–CdS-NS and Au-NR–CdS-NS impregnated samples respectively. The PAP yield (~53%) and selectivity (~85%) are also found to be considerably higher for Au-NR–CdS-NR composites among the other studied Au–CdS composites (Fig. 13). The better delocalization of charge carriers along the length of elongated NCs facilitates quick e^-–h^+ pair separation and reduced the recombination time.

Nanorods volume is larger than nanospheres and therefore, they have been significantly larger per particle absorbance cross sections and surface exposure for adsorption of target

species. Large surface area of nanorods may allow a better contact and hence, improve the interfacial space between them and help in the adsorption of target species in surrounding electrolyte. Large aspect ratio semiconductors such as nanorods are of particular interest because of their ability to generate multiple excitons.

The metal can serve as a charge-collecting material where carriers localize after exciton quenching. The advantage of forming Au-NS–CdS-NR and Au-NR–CdS-NR junctions over other possible arrays, facilitates double rectification; first by the delocalization of charge carriers along the longitudinal and radial side, which may guarantee to be further rectified in Au noble metal plasma due to its larger volume and secondly by sensitizing photonic flux toward the more visible region owing to the presence of an Au surface Plasmon band. Higher residence time of photoexcited charge species for Au-NR–CdS-NR nanocomposites can be explained on the basis of higher interfacial contact for charge transfer, which directly hindered the e^{-}/h^{+} pair recombination rate and prolonged the carrier's lifetime. Accumulation of the charge by the Au NPs will lead eventually to Fermi level equilibration (which is size dependent) with the CdS–SC and thus leads to better charge transfer at the junction.

Therefore, interfacial properties (photoluminescence, electrical and photocatalytic) can be modulated as a function of the size and shape of Au and CdS nanocrystals, their suitable spatial alignments and adsorbed electrolyte because, the shift in band edge position and space charge barrier can alter the energetics and charge transfer kinetics at Au–CdS interface. Moreover, the different atomic planes available at the surface of shapes other than spheres can also trans-late into materials that catalyze different reactions based on their shape. Thus, it is evident that the right orientation of Au and CdS NPs is an important parameter for exhibiting optimum photoactivity of any M–SC heterojunctions. The best selectivity and yield of PAP formation and highest SA degradation could be justified upon the basis of beneficial advantages of the lengthy Au-NR–CdS-NR interface.

It is experimented that the Au-NR–CdS-NR interface proved to be highest photoactive than conventional metal–semiconductor junctions as a function of better contact area, higher delocalization and charge carriers lifetime .

6.4. References

[1] A A. Takai, P.V. Kamat, ACS Nano 4 (2011) 7369–7376.

[2] G.L. Puma, A. Bono, D. Krishnaiah, J.G. Collin, J. Hazard. Mater. 157 (2008) 209-219.

[3] B. Gao, C. Peng, G.Z. Chen, G.L. Puma, Appl. Catal. B; Environ. 85 (2008) 17-23.

[4] M.R. Bayati, F. Golestani-Fard, A.Z. Moshfegh, Mater. Chem. Phys. 120 (2010) 582-589.

[5] A. Wood, M. Giersig, P. Mulvaney, J. Phys. Chem. B 105 (2001) 8810–8815.

[6] N. Zhang, S. Liu, X. Fu, Y.J. Xu, J. Phys. Chem. C 115 (2011) 9136–9145.

[7] T. O'Connor, M.S. Panov, A. Mereshchenko, A.N. Tarnovsky, R. Lorek, D. Perera,G. Diederich, S. Lambright, P. Moroz, M. Zamkov, ACS Nano 6 (2012) 8156–8165.

[8] Q. Zhang, C.H. Moran, X. Xia, M. Rycenga, N. Li, Y. Xia, Langmuir 28 (2012) 9047–9054.

[9] R. Tung, Mater. Sci. Eng., R 35 (2001) 1.

[10] J. Ohyama, A. Yamamoto, K. Teramura, T. Shishido, T. Tanaka, ACS Catal. 1 (2011) 187–192.

[11] M. Haruta, M. Date, Appl. Catal. A: Gen. 222 (2001) 427–437.

[12] A. Salant, M. Shalom, Z. Tachan, S. Buhbut, A. Zaban, U. Banin, Nano Lett. 12(2012) 2095–2100.

[13] H.J. Yun, H. Lee, J.B. Joo, W. Kim, J. Yi, J. Phys. Chem. C 113 (2009) 3050–3055.

[14] E.R. Smith, J.M. Luther, J.C. Johnson, Nano Lett. 11 (2011) 4923–4931.

[15] D.R. Pernik, K. Tvrdy, J.G. Radich, P.V. Kamat, J. Phys. Chem. C 115 (2011) 13511–13519.

[16] D.O. Demchenko, R.D. Robinson, B. Sadtler, C.K. Erdonmez, A.P. Alivisatos, L.W.Wang, ACS Nano 4 (2008) 627–636.

[17] P.K. Santra, P.V. Kamat, J. Am. Chem. Soc. 134 (2012) 2508–2511.

[18] K. Wu, H. Zhu, Z. Liu, W.R. Co'rdoba, T. Lian, J. Am. Chem. Soc. 134 (2012) 10337–10340.

[19] Y. Xie, K. Ding, Z. Liu, R. Tao, Z. Sun, H. Zhang, G. An, J. Am. Chem. Soc. 131 (2009) 6648–6649.

[20] P.V. Kamat, B. Shanghavi, Phys. Chem B. 101 (1997) 7675-7679.

[21] K. Easawi, M. Nabil, T. Abdallah, S. Negm, H. Talaat, World Academy of Science, Engineering and Technology 61 (2012) 642-645.

[22] R.D. Paiva, R.D. Felice, J. Phys. Chem. C 114 (2010) 3998–4007.

[23] G. Menagen, J.E. Macdonald, Y. Shemesh, I. Popov, U. Banin, J. Am. Chem. Soc. 131 (2009) 17406–17411.

[24] Y. ZhaoHui, C. HaiBin, J. Zhong, Z. WeiWei, L. Yan, Chin. Sci. Bull. 55 (2010) 921–926.

[25] F. Petronella, E. Fanizza, G. Mascolo, V. Locaputo, L. Bertinetti, G. Martra, S.Coluccia, A. Agostiano, M.L. Curri, R. Comparelli, J. Phys. Chem. C 115 (2011)12033–12040.

[26] R. Singh, B. Pal, J. Mol. Catal. A: Chem. 371 (2013) 77–85.

[27] G.S. Lotey, N.K. Verma, J. Nanopart. Res. 13 (2011) 5397–5405.

[28] E. Rothenberg, M. Kazes, E. Shaviv, U. Banin, Nano Lett. 5 (2005) 1581–1586.

[29] J. Mu1ller, J.M. Lupton, P.G. Lagoudakis, F. Schindler, R. Koeppe, A.L. Rogach, J. Feldmann, Nano Lett., 5 (2005) 2044.

Chapter 7: Woollen Bun like CdS Microspheres Wrapped with Lengthy Nanowires Exhibit Superior Photoactivity for Dye Degradation under Sunlight

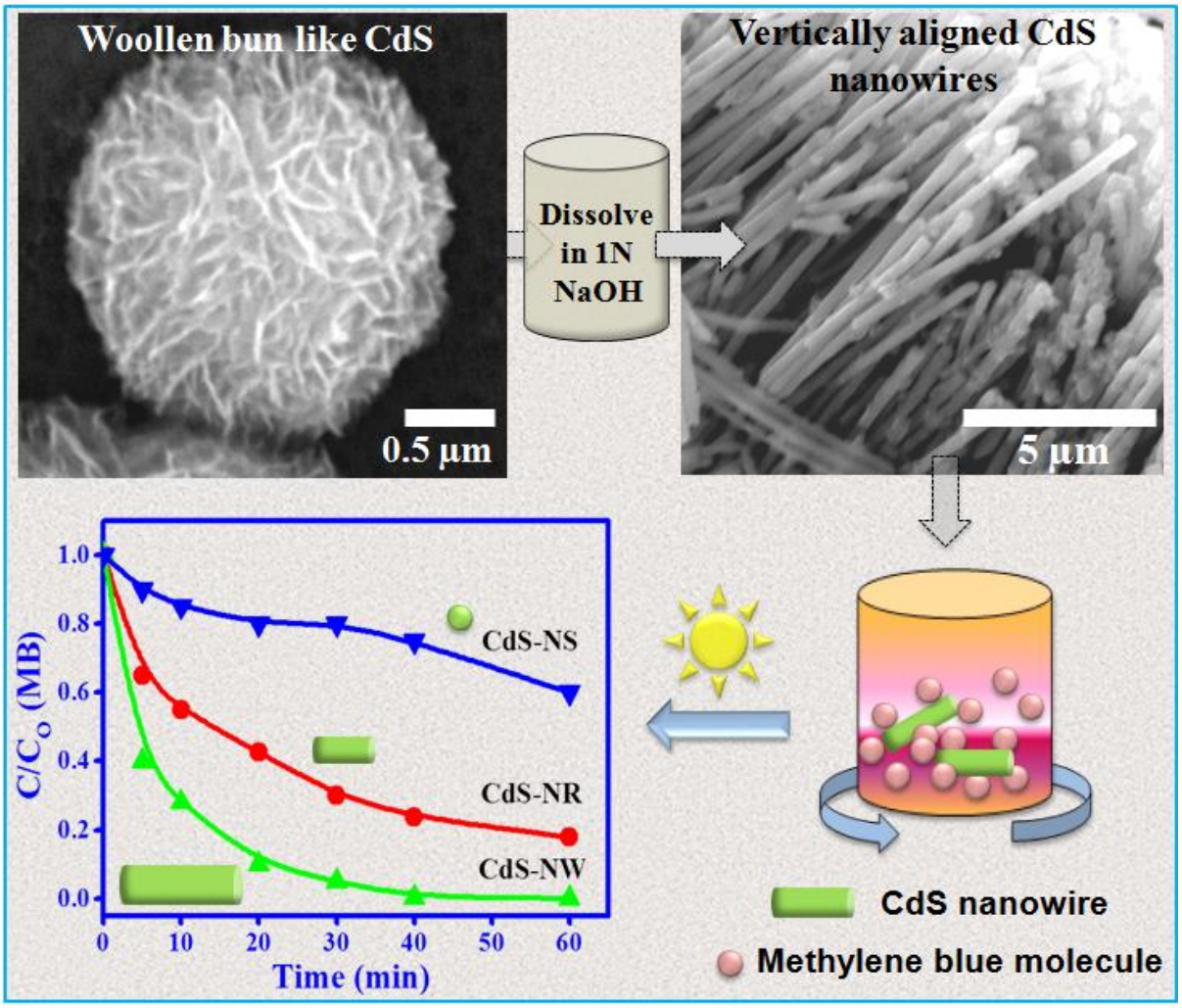

7.1. Introduction

Previous chapters already have discussed the importance of one dimensional metal and semiconductor nanocrystals (NCs) such as NR, NT and NW relative to NS having poor quantum efficiency. The properties of such anisotropic 1 D materials lie between the *nano- and micro-scale*, that are blessed with larger per–particle surface area, higher surface exposed molecules/atoms, superior adsorption of reacting substrates and better separation of photoexcited charge carriers along the longitudinal and radial directions [1–3]. Their electronic and optical properties are governed by the decrease in the confinement of charge carriers by the cylindrical symmetry of the particles [4–7]. Sufficient control over the morphology (size & shape) of nanomaterials is an important issue in the current research in controlling their overall photophysical and photochemical properties.

As already discussed in chapter 1, CdS nanostructures proved to be a potential candidate to drive several important applications ranging from optical to photovoltaic. Nevertheless, the photocatalytic efficiency of CdS is seriously restricted by the immediate recombination of e^-/h^+ pairs. As a result, the ability to control the geometric morphology of NCs has been a significant objective to extend the scope of lifetime of charge carriers for achieving the optimum photoactivity. Specially, cylindrical shape materials such as NR, NT and NW have great potential for understanding the roles of dimensionality on the physical properties as a function of the atomic/molecular arrangements, surface exposed atomic planes, sharp edge and corner etc.

Herein, we prepared woollen bun (spinning wool) like CdS microspheres (2–5 μm) wrapped with lengthy and crystalline CdS-NW to achieve best photocatalytic activity for the rhodamine B (RhB) and methylene blue (MB) dyes degradation under direct sunlight illumination. The use of anodic alumina membrane (AAM) with fixed pore size as a hard template was used to facilitate better control over the size and shape of NWs.

7.2. Experimental Section

7.2.1. Synthesis of CdS nanowires

CdS nanowires (CdS-NWs) were successfully synthesized as discussed in *chapter 2, section-2.2.3.* CdS-NS with cubic (c) and hexagonal (h) phase were prepared for comparison as mentioned in *section 2.2.1 of chapter 2*.

7.2.2. Photocatalytic reactions

The photoactivity of the CdS-NW (2 mg) was evaluated by the photodegradation of 10 ml RhB (5×10^{-5} mol L^{-1}) and MB (2×10^{-5} mol L^{-1}) dyes in a 25 ml beaker under continuous magnetic stirring and sunlight (intensity = 50 mW/cm^2) irradiation and analyzed by UV-vis spectrophotometer (λ_{max} = 554 nm for RhB & λ_{max} = 665 nm for MB). The reaction mixture was kept in the dark under stirring for 1 h to attain the adsorption/desorption equilibrium.

7.2.3. Characterizations

Techniques; SEM, TEM, XRD, UV-vis, PL were used to get an information of size, shape, crystal structure, absorbance, and defects. Residue thus obtained of RhB sample was re-dissolved in methanol and analyzed by GC-MS. The CO_2 evolution was determined by injecting 1 ml of the gaseous mixture from the reaction vessel into the gas chromatography using a Propak–Q column with nitrogen as a carrier gas (30 ml/min) and Thermal Conductivity Detector (TCD).

7.3. Results and discussion

7.3.1. Structural analysis of CdS nanostructures

X-ray diffraction (Fig. 1) pattern shows strong intense sharp peaks for highly crystalline hexagonal (wurtzite) crystal structure of CdS–NW with lattice parameters, a = b = 4.042 Å, and c = 6.64 Å, which is in good agreement with the JCPDS card No. 41–1049. The {002}, {110} and {112} lattice planes are found to be more intense and narrower relative to other crystal planes indicating its preferential growth along these planes [8]. Spherical (15 ± 8 nm) and rod (170 × 10 nm) shaped hexagonal CdS–NS displayed relatively broad, low intense and less crystalline phases. The grain size calculated by Scherer's equation [9] has been found to be 18, 21.3 and 37.8 nm for NS, NR and NW, respectively.

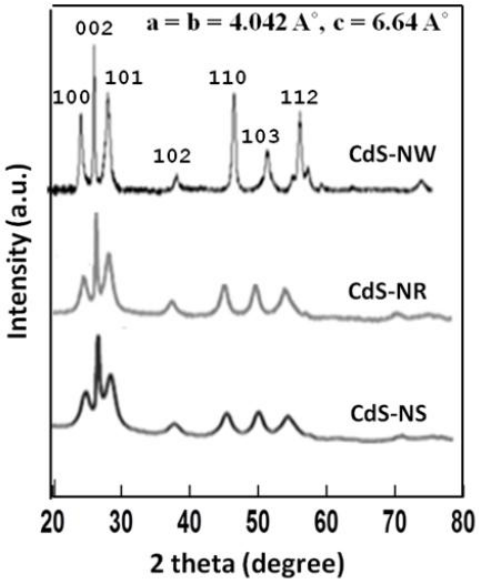

Fig. 1. X-ray diffraction patterns of as-prepared various CdS nanostructures.

7.3.2. SEM/TEM analysis of CdS nanostructures:

Monodisperse CdS–NS has a size of 2–5 μm entrapped in AAM are seen in the SEM image of Fig. 2a. An enlarge view (Fig. 2b to 2d) shows that this microstructure is composed of several haphazard CdS-NWs arranged like spinning wool with coarse surface morphology. Dissolution of AAM with 1N NaOH resulted in uniform fashion of CdS nanowires with length in the range of 8–10 μm and diameter of 50–80 nm as shown in Fig. 2e. Dense grass like vertically or parallel aligned bunches of many CdS nanowires are also observed in Fig. 2f and 2g.

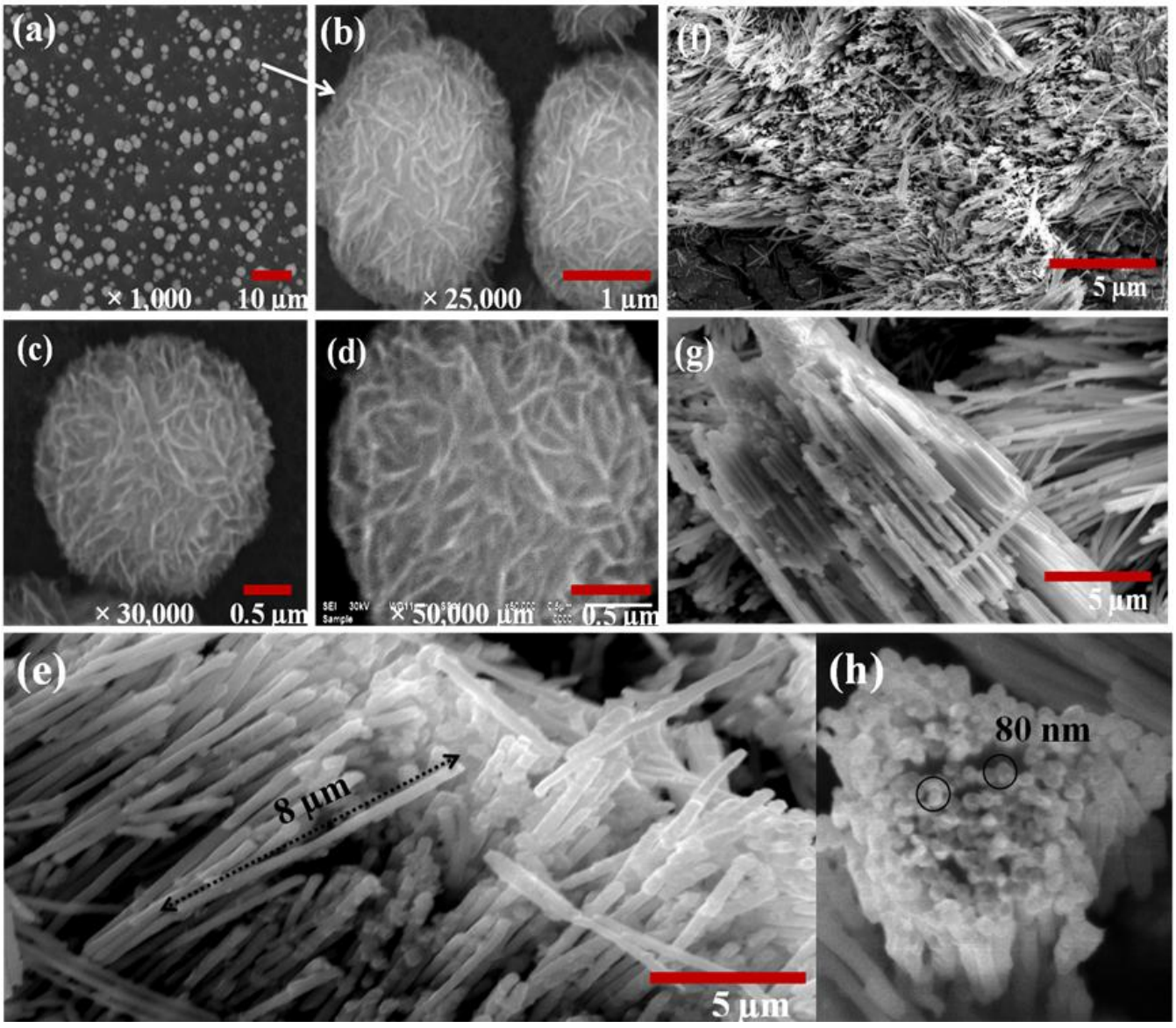

Fig. 2 SEM images of CdS microspheres composed of haphazard nanowires at different resolution (a–d) and (e–h) CdS 1D-nanowires aligned at various directions.

Nanowires with much uniformity in diameter are clearly distinctive in the image 2h. Nanowires orientations with different resolutions are also clearly shown in additional SEM images (Fig. 3 (a-f)).

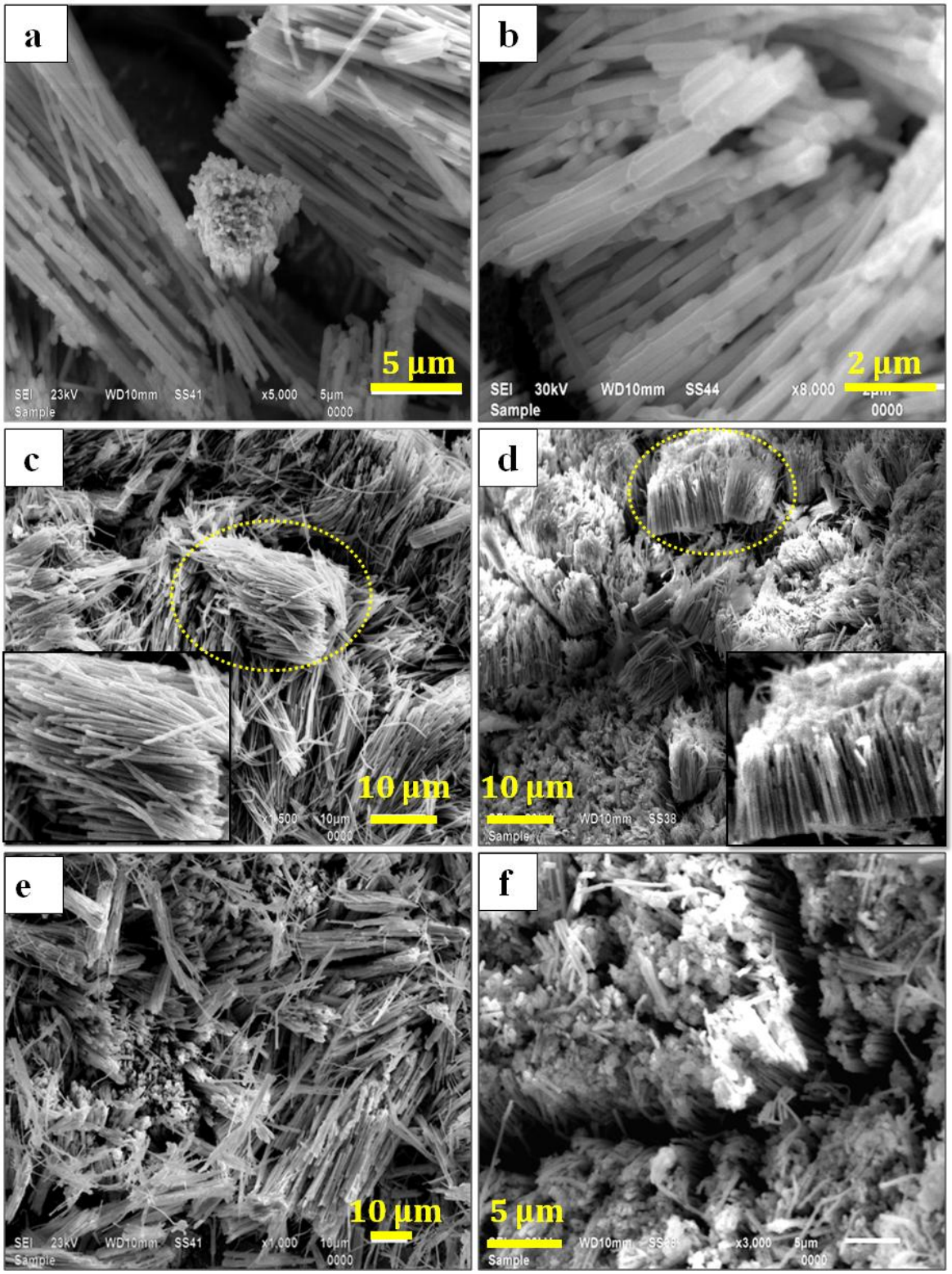

Fig. 3. (a-f) SEM images of CdS nanowires at different resolution.

TEM photographs elucidate the spherical morphology of CdS with size lies in the range of 10–12 nm (cubic phase) and 15 ± 8 nm (hexagonal phase) and 170 nm × 10 nm (hexagonal-NR) that were prepared for comparison.

7.3.3. Optical study

As shown in Fig. 4, the absorption edge appears at 490 nm for hexagonal NS and at 525 nm for NW that is similar to bulk CdS particles.

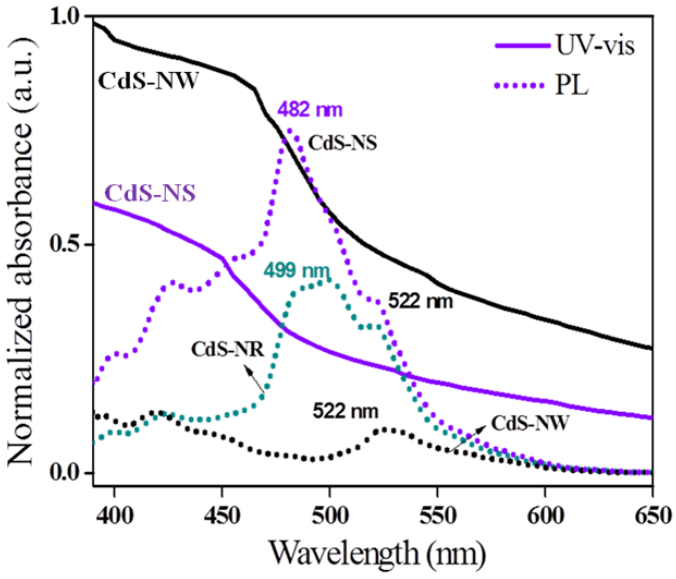

Fig. 4. UV–vis and PL–spectra of CdS-NW in comparison to NR and NS.

Photoexcitation of NS, NR and NW (1mg/ml-acetone) suspension at 380 nm led to photoluminescence (PL) at 490, 506 and 520 nm, respectively due to respective CdS band edge absorption, and a weak emission band centered at 530 nm is observed due to the existence of surface defects in poor crystalline NS and NR. Confinement of both the carriers and emitted photons in the CdS-NW radial direction is expected to suppress surface state mediated nonradiative recombination and to decrease thermal quenching of emission intensity. Notably, PL of NW is almost completely quenched in compared with NS and NR, because of better crystallinity (less surface defects) and radial confined improved delocalization.

The average lifetime [10] of photoexcited e^-/h^+ pairs calculated by time resolved fluorescence decays (Fig. 5) has been found to be gradually increased as 2.2 2.4 and 3.6 ns for

NS, NR and NW, respectively, confirming better delocalization of e^-–h^+ pairs in the lengthy crystalline NW.

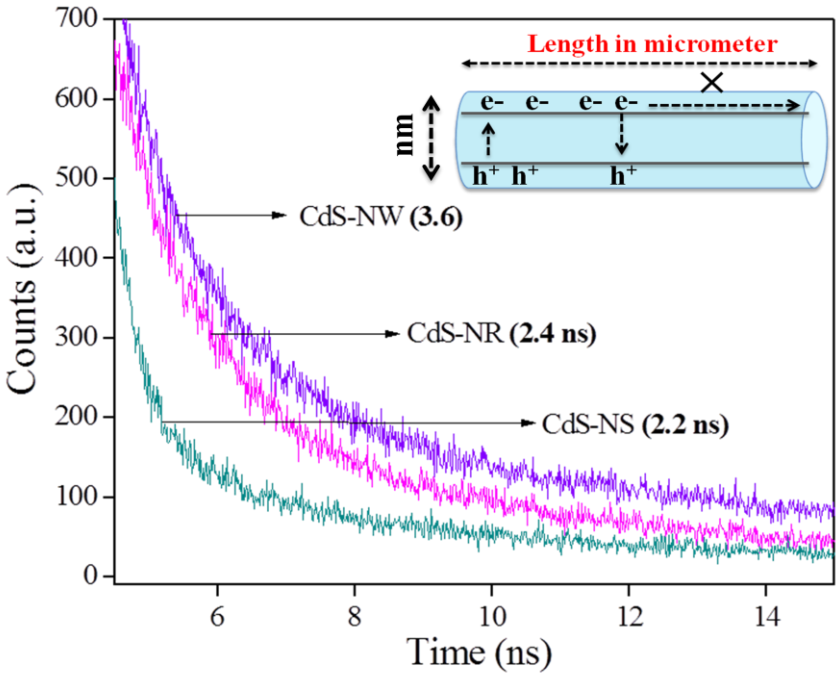

Fig. 5. Time resolved decay curves of CdS nanowires, nanorods and nanospheres with proposed pathway of photoexcited charge carriers.

7.3.4. Photocatalytic study

The photocatalytic activity of as prepared CdS nanowires was evaluated by monitoring the optical behavior of rhodamine B (RhB) and methylene blue (MB) dyes as shown in Fig. 6. Photooxidation of RhB was merely affected in direct photolysis and dark adsorption even after a longer period of time. A gradual change in colors of RhB and MB dyes has also been noticed with increasing degradation/or irradiation time. It has been observed that the absorbance of the RhB solution shifts gradually from the initial 554 nm to shorter wavelength and finally reach at 498 nm. This hypsochromic shift in λ_{max} corresponds to a de-ethylation of RhB, and the peak centered at 498 nm is assigned to the absorbance of rhodamine.

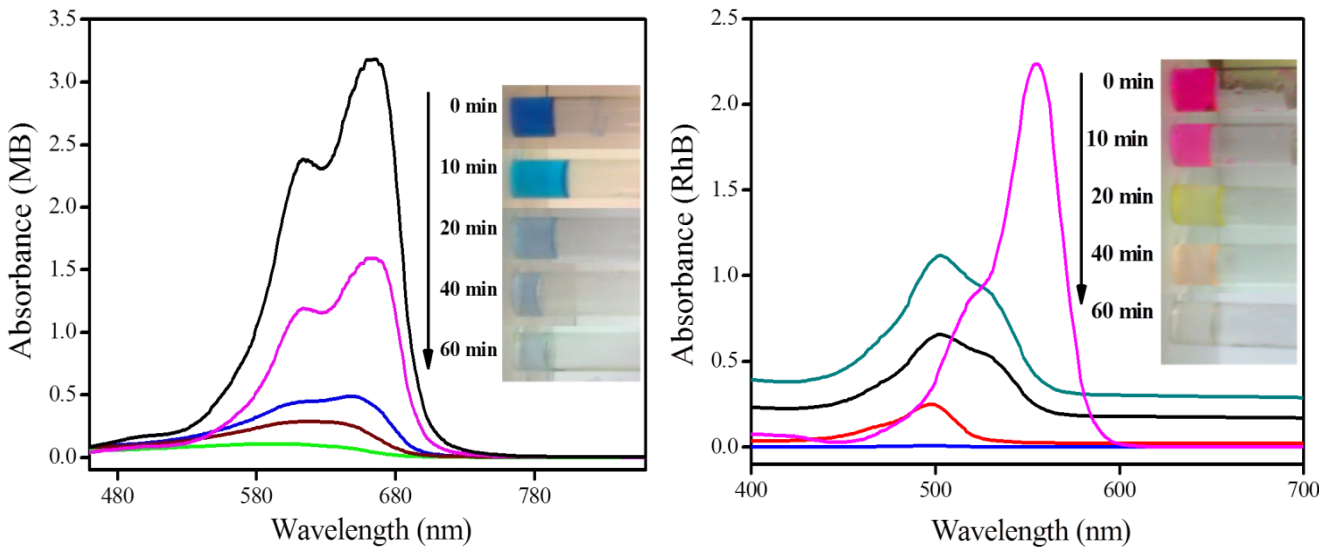

Fig. 6. Change in absorbance spectra of MB (left) and RhB (right) dye photodecomposition under sunlight illumination with CdS NWs.

The comparative photocatalytic activity for the RhB and MB degradation under solar irradiation (Fig. 7) showed that a linear decrease by cubic–NS (c–NS) and hexagonal–NS (h–NS) and exponential decrease ($C = C_o e^{-kt}$) of dye concentration by NR and NW, follows the 1st order reaction kinetics like many other photochemical reactions. An observed rate constant (k_{obs}) for RhB degradation after 30 min sunlight exposure were found to be greatly enhanced as 2×10^{-2}, 3×10^{-2}, 5.5×10^{-2}, 8×10^{-2} and 9.2×10^{-2} min^{-1} and 25, 50, 76.4 and 90.9% (degradation%) for c–NS, h–NS, NR and NW.

The GC-MS analysis confirmed many intermediate product formation (peaks A, B, C and D at retention time 7.5, 11.85, 12.75 and 14.22 min and their mass spectra are (Fig. 8) during 1 h RhB degradation. Two competitive processes, namely, N-deethylation and destruction of a dye chromophore structure [13-15] are occurring where some primary oxidation products such as butane 1,3-diol, oxalic acid, propane-1,2,3-triol, phenol, benzoic acid and pyrocatechol are observed before its complete mineralization to CO_2 formation as listed in the table of Fig. 7. A linear increase in CO_2 evolution with irradiation time (Fig. 7c) has been observed depending on CdS morphology. Lengthy CdS NW exhibit maximum rate of CO_2 production due to rapid decomposition of RhB dye in accordance [16] with 90% degradation by 0.5 g/L of CdS nanowires (L = 2.1 to 4.6 μm) during 4 h UV irradiation.

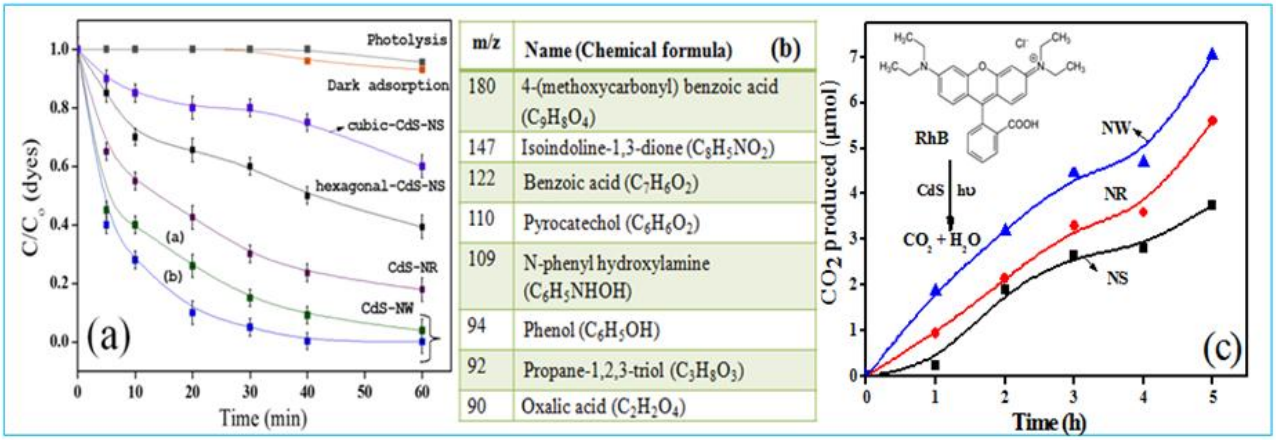

Fig. 7. (a) C/C_o Plots versus irradiation time of (a) RhB and (b) MB (10 ml, 5×10^{-5} mol L^{-1}) degradation (b) identified intermediates of RhB decomposition by GC-MS analysis and (c) time course of CO_2 evolution during RhB degradation with various CdS nanostructures (2 mg) under sunlight exposure.

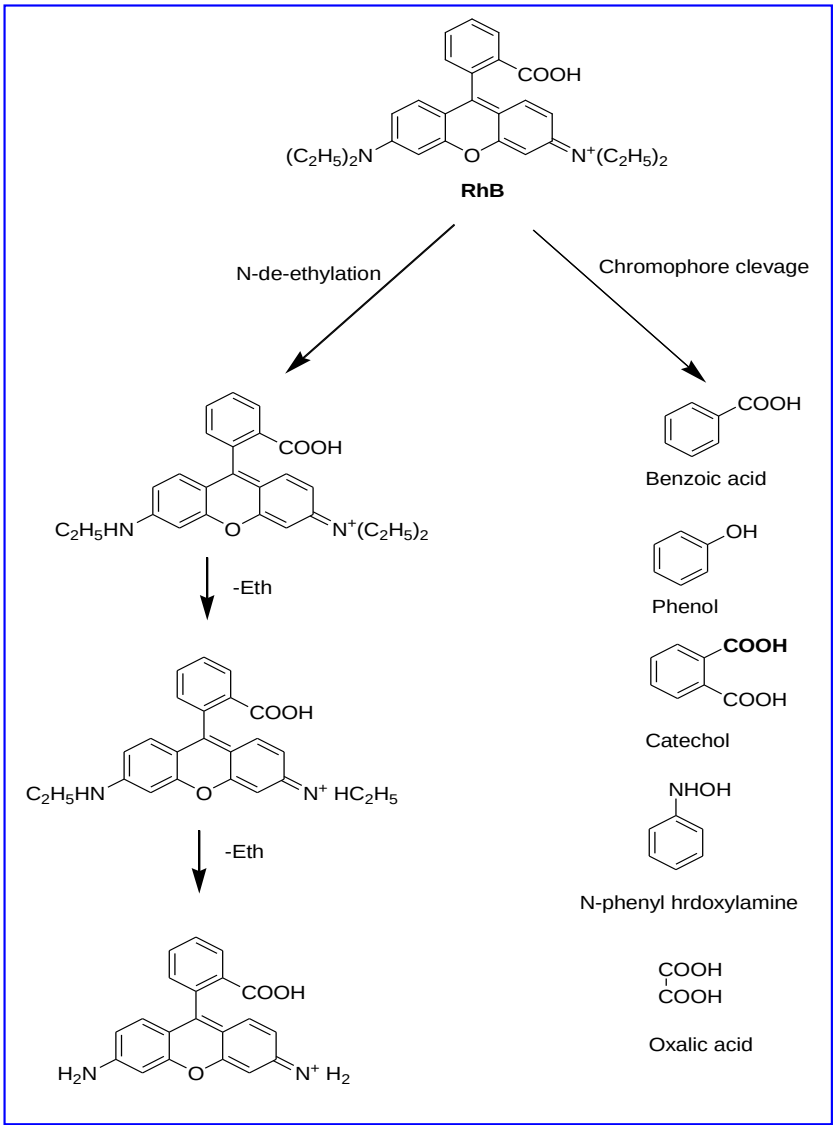

Fig. 8. Proposed degradation pathway of RhB dye with CdS-NW under sunlight irradiations

As the diameter (~10 nm) of both NS/NR to (50 nm) NW is increased to 5 times, and length to 17 (NS to NR) and 47 (NR to NW) times resulted in 3 and 1.2 times enhancement in RhB degradation. Therefore, it is presumed that no appreciable quantum confinement occurs in longitudinal direction due to increase in length in the micrometer range, in contrary to radial delocalization of photoexcited e^-–h^+ pairs in NW possess higher relaxation time 3.6 ns relative to 2.2 ns for NS and NR for 2.4 ns is not significant as per the length increment. In other words, the best photoactivity of NW could also be ascribed to superior crystallinity, larger per particle surface area: 314 < 5495 < 1259925 nm^2 having more surface exposed CdS; 628 < 10×10^3 < 2.5×10^6 molecules out of total 1960, 5×10^4 and 5.8×10^4 CdS molecules in each NS, NR and NW particles, respectively, utilized in photoreaction.

Thus, considering the total surface active CdS: 7.5×10^{16} out of 8.33×10^{18} molecules in 2 mg NW particles suspended in 3×10^{17} RhB molecules led to an increased dye coverage ratio: 123 (NS) < 2163 (NR) < 496033 (NW) per CdS particle is notably improved, confirming dye decomposition is photocatalytic in nature as given in table 1.

Table 1. Outlook of various parameters and their calculations used in the photodegradation study

Catalyst	Total no. of molecules in 2 mg CdS [a*]	Total no. of molecules in RhB [a*]	Total no. of particles in 2 mg CdS [b*]	No. of molecules in single CdS particle [c*]	Surface area of single CdS particle [d*]	Effective no. of molecules on the surface [e*]	RhB/CdS coverage ratio [f*]
CdS-NS	8.33×10^{18}	3×10^{17}	8×10^{14}	1960	314	628	123
CdS-NR	8.33×10^{18}	3×10^{17}	3×10^{13}	5000	5495	10,990	2163
CdS-NW	8.33×10^{18}	3×10^{17}	3×10^{10}	58×10^6	1.25×10^6	2519850	496033

In summary, we demonstrated a method of self assembling crystalline CdS–NW similar to spinning wool that can be utilized as per demand by the extent of its dissolution from AAM with NaOH.

7.4. References

[1] K.L. Meagley, S.P. Garcia, Cryst. Growth Des. 12 (2012) 707–713.

[2] X.Y. Yu, J.Y. Liao, K.Q. Qiu, D.B. Kuang, C.Y. Su, ACS Nano 5 (2011) 9494–9500.

[3] R. Singh, B. Pal, J. Mol. Catal. A: Chem. 378 (2013) 246–254.

[4] J.H. Bang, P.V. Kamat, ACS Nano 3 (2009) 1467–1476.

[5] H.B. Yang, C.X. Guo, G.H. Guai, Q.L. Song, S.P. Jiang, C.M. Li, ACS Appl. Mater. Interfaces 3 (2011) 1940–1945.

[6] H. Zhu, N. Song, H. Lv, C.L. Hill, T. Lian, J. Am. Chem. Soc. 134 (2012) 11701–11708.

[7] D.R. Pernik, K. Tvrdy, J.G. Radich, P.V. Kamat, J. Phys. Chem. C 115 (2011) 13511–13519.

[8] J. Zhang, F. Jiang, L.J. Zhang, J. Phys. Chem. B 108 (2004) 7002–7005.

[9] S. Wageh, A.A. Higazy, A.S. Hassouna, J. Mater Sci: Mater Electron. 24 (2013) 3049–3057.

[10] S. Khanchandani, S. Kundu, A. Patra, A.K. Ganguli, J. Phys. Chem. C 116 (2012) 23653−23662.

[11] T.A. Egerton, P.A. Christensen, R.W. Harrison, J.W. Wang, J. Appl. Electrochem. 35 (2005) 799–813.

[12] I.K. Konstantinou, T.M. Sakellarides, V.A. Sakkas, T.A. Albanis, Environ. Sci. Technol. 35 (2001) 398–405.

[13] L.I. Jing-yi, M.A. Wan-hong, L.E.I Peng-xiang, Z. Jin-cai, Environ. Sci. 19 (2007) 892–896.

[14] K. Yu, S. Yang, H. He, C. Sun, C. Gu, Y. Ju, J. Phys. Chem. A 113 (2009) 10024-10032.

[15] T. Aarthi, G. Madras, Ind. Eng. Chem. Res. 46 (2007) 7–14.

[16] F. Zhang, S.S. Wong, Chem. Mater. 21 (2009) 4541–4554.

Chapter 8: Preparation of Coinage Metal Doped CdS Nanorods for Highly Improved Photocatalytic Oxidation and Reduction Processes

8.1. Introduction

The intentional introduction of metal particles (impurities) into a semiconductor is believed to improve its photophysical, photocatalytic and antiphotocorrosion properties [1-5]. These properties are very sensitive to even a small change in crystal structure, defects, and surface porosity. Metal ions may influence the surface property by generation of a Schottky barrier through the metal in contact with the semiconductor surface, which acts as an electron trap that can capture e^- or h^+ and thereafter inhibit e^-/h^+ recombination [chapter 6, ref. 6-8]. Techniques; photodeposition, spin-coating, impregnation and doping like various techniques were employed to deposit/doped metal islands onto SC surface. But the uncontrolled distribution of M-NPs during metal photodeposition technique can limit their efficiency because most of them get aggregated onto the SC surface and results in improper alignment of M–SC arrays [6-10]. On the other hand, the replacement of some cations with external metal ions by means of doping provides a pathway for symmetric distribution of metal particles, which result in the better Fermi energy contact and suitable stable structure for a large number of practical applications.

Most recently, Ouyang et al has synthesized $Zn_xCd_{1-x}S$ photoluminescent colloidal for synthesis- structure property relationship [11]. Ni doped CdS hollow spheres have been noticed in the literature for the enhancement in photoactivity and stability of the catalyst by Lio et al [12]. It has been well-accepted that photoactivity is found to be highly dependent upon the size distribution of metal deposits, interfacial contact area and nature of metal-support interactions. Conventional metal deposition techniques led to uncontrolled and irregular size distribution of metal particles onto the SC surface that having a poor electrical contact, i.e., M-NPs present only on the surface and not at all uniformly mixed with the crystal. Moreover, higher amount of metal ions present would act as recombination centres for e^-/h^+ pairs through the following process:

$$M^{n+} + n^{e-}{}_{CB} \rightarrow M^{0+}$$

As in our earlier study, we have synthesized M (Au, Ag and Cu) - CdS nanocomposites by various routes and investigated their influential effects, hence, this is very interesting to introduce above metals into CdS-NR lattices at different doping levels to observe change in their overall properties. Metal ion doping is believed to improve the physicochemical properties

because it can lead to shift of band edge levels that drive oxidation and reduction reactions, creation of doping levels, narrowing of the band gap for higher visible spectral response, suitable stable structure, homogeneous distribution of charge and more importantly the improvement of ionic bond formation.

Herein, Au^{3+}, Ag^{+} and Cu^{2+} metal ion with different concentration were doped into CdS-NR to know the effect of nature and concentration of dopant onto various properties; optical, structural, magnetic, surface and current-voltage characteristics, and photocatalytic oxidation and reduction reactions. The products of m-dinitrobenzene (*m*-DNB) i.e., m-phenylenediamine (*m*-PDA) and m-nitroanilne (*m*-NA) are important intermediates for the synthesis of pharmaceuticals, agrochemicals and dyes industries. The significant differences in reduction potentials of m-DNB (0.17 eV) and CdS (-0.4 eV vs NHE) favors the reduction reaction by conduction band electrons.

8.2. Experimental section

8.2.1. Synthesis of coinage metal doped CdS-NR

Au^{3+}, Ag^{+} and Cu^{2+} were doped by facile method as discussed in *chapter 2, section 2.2.6.*

8.2.2. Photocatalytic and other properties

Current density- voltage characteristics of pure and doped samples were studied as mentioned in *chapter 2, section 2.2.9.* Magnetic properties; magnetic susceptibility was calculated as discussed in *chapter 2, section 2.2.10*. The photocatalytic activity of various doped samples was evaluated for the photooxidation of 5 ml salicyldehyde (0.5 mM) and reduction of m-dinitrobenzene (5 mM) in a test tube containing 10 mg catalyst under UV and sunlight irradiation. The reaction samples were analyzed by UV–vis spectrophotometer after filtration with 0.22 µm cellulose filter. Photoreduction of m-DNB (5 ml, 5 mM) with CdS samples has been carried out under UV light irradiation for 1 h and analyzed by High Performance Liquid Chromatography (HPLC, Agilent, 1120 Compact LC, 254 nm) using C-18 column and MeOH: H_2O (70:30) as mobile phase (ACN: H_2O (70:30) for nitrobenzaldehyde) at a flow rate of 1 ml min^{-1}.

8.2.3. Characterizations

As synthesized doped CdS samples were characterized by DRS, PL, XRD, EDX, TEM spectroscopy. The performance of the DSSC is evaluated from manually recorded photocurrent-photo-voltage curves. The surface area was determined by using BET adsorption isotherms.

Magnetic properties were determined by using Goy's magnetic susceptibility apparatus as mentioned in *chapter 2, section 2.3.14*.

8.3. Results and discussion

8.3.1. Optical study

Diffuse absorbance spectra and band gaps of the 10 mol% coinage metals (Au^{3+}, Ag^{+} and Cu^{2+}) doped CdS-NR are displayed in Fig. 1. The red-shift of the absorption edges also implies that the band gaps of the $M_xCd_{1-x}S$ solid solution can be precisely controlled through the variation of M^{n+}/Cd^{2+} molar ratios in precursors. It is evident from the Fig. 1a that pure CdS-NR exhibited absorbance around 485 nm. Addition of doping (impurities) into CdS matrix led to fine red shift in the absorption band. It has been observed here that absorbance band is tuned to 560 nm with the increasing level of dopant into CdS-NR. The excitonic feature of semiconductors may experience broadening in the transverse direction of CdS-NR corresponds to lowest energy transition 1S (e) → $1S_{3/2}$ (h).

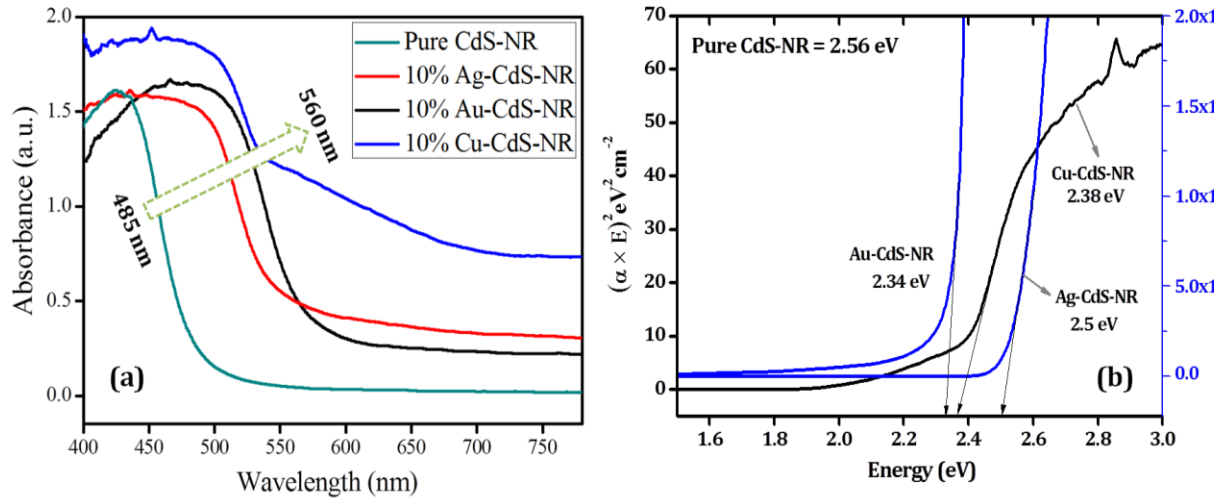

Fig. 1. (a) Diffused absorbance spectra and corresponding (b) band gaps of various pure and doped CdS samples.

Here, we observed that the nature and increasing content of coinage metal that has to be doped in CdS nanostructures play a crucial role to fine-tune its UV-visible spectrum. Interestingly, doping of 10% Au^{3+}, Ag^{+} and Cu^{2+} into CdS-NR improved its spectrum range for maximum absorption from 485 nm to correspond 560, 542 and 536 nm, respectively. Corresponding, band gaps have been calculated by Tauc plots to be 2.56, 2.5, 2.38, and 2.34 eV for pure, 10 mol % Au^{3+}, Cu^{2+}

and Ag^{+} doped CdS-NRs. Herein, it has been observed that an increase in wt% from 1 to 10 in all metals, remarkable improved the spectrum response of CdS-NR, and that is also reflected by their color variations (Fig. 2). Probably due to intermixing of Cd ions with Au^{3+}, Ag^{+} and Cu^{2+} ions led to a remarkable change in the electronic states of CdS. Large number of SPR electrons can flow from metal to CdS domain and resulted in a change in the absorption spectrum. Hence, it is very interesting to tune the spectral region by increasing/decreasing dopant concentration.

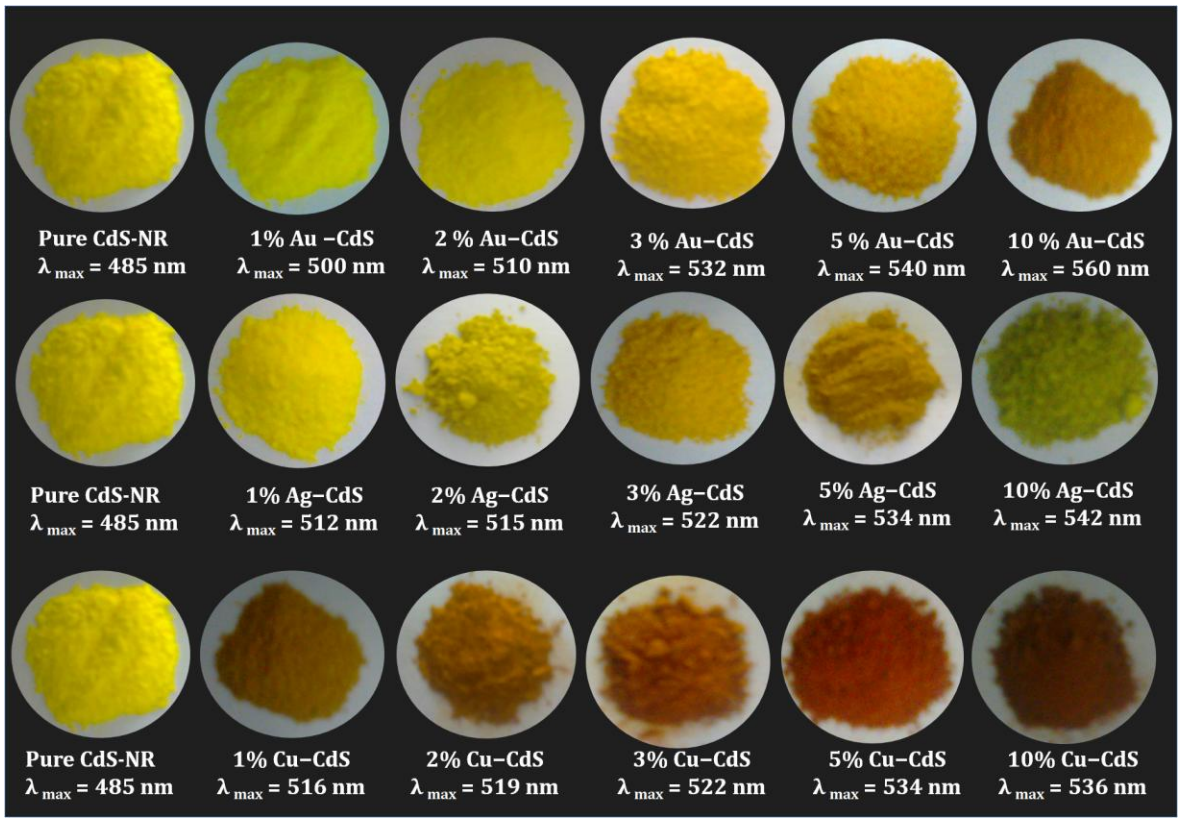

Fig. 2. Tunability of colors in CdS samples after doping with Au, Ag and Cu metals.

Photoluminescence (Fig. 3) has been measured to elucidate possible defects and transitions in 10 mol% Au^{3+}, Ag^{+} and Cu^{2+}-doped CdS nanorods. It has been observed that fluorescence (λ_{ext} = 380 nm) of doped samples exhibited a fine red shift from 506 nm to 508 nm for Au^{3+} doping, to

533 nm for Ag^{+} doping and Cu^{2+} doping with varying wt%. Band edge emission; 506-532 nm and surface trap emission; 530 nm are notably assigned due to recombination of charge carriers.

It has been found that band edge emission significantly red-shifted with the addition of dopant concentration. This green emission band was associated with emission due to electronic transition from CB to acceptor level due to interstitial sulfur ions. Fluorescence quenching in M-CdS nanocomposites can be attributed to transfer of exciton energy into metal domain by Forster resonance energy transfer (FRET) mechanism and due to ultrafast transfer of photoinduced charge from SC to metal nearby. Moreover, introduction of different wt% Au^{3+}, Ag^{+} and Cu^{2+} into CdS-NR dramatically quenched the fluorescence emission due to the prevention of electron-hole recombination owing to rapid electron capture by the metal-NPs onto CdS surface [12-17]. Hence, an electron-transfer from the CdS to metal- NPs reduced the surface defects & trap sites and thereby changes the optical properties.

The change in intensity between 506 nm -532 nm, corresponding to band edge emission and 533 nm, corresponding to surface trap states with 10% Au^{3+}, Ag^{+} and Cu^{2+} are also shown in Fig 3c and 3d.

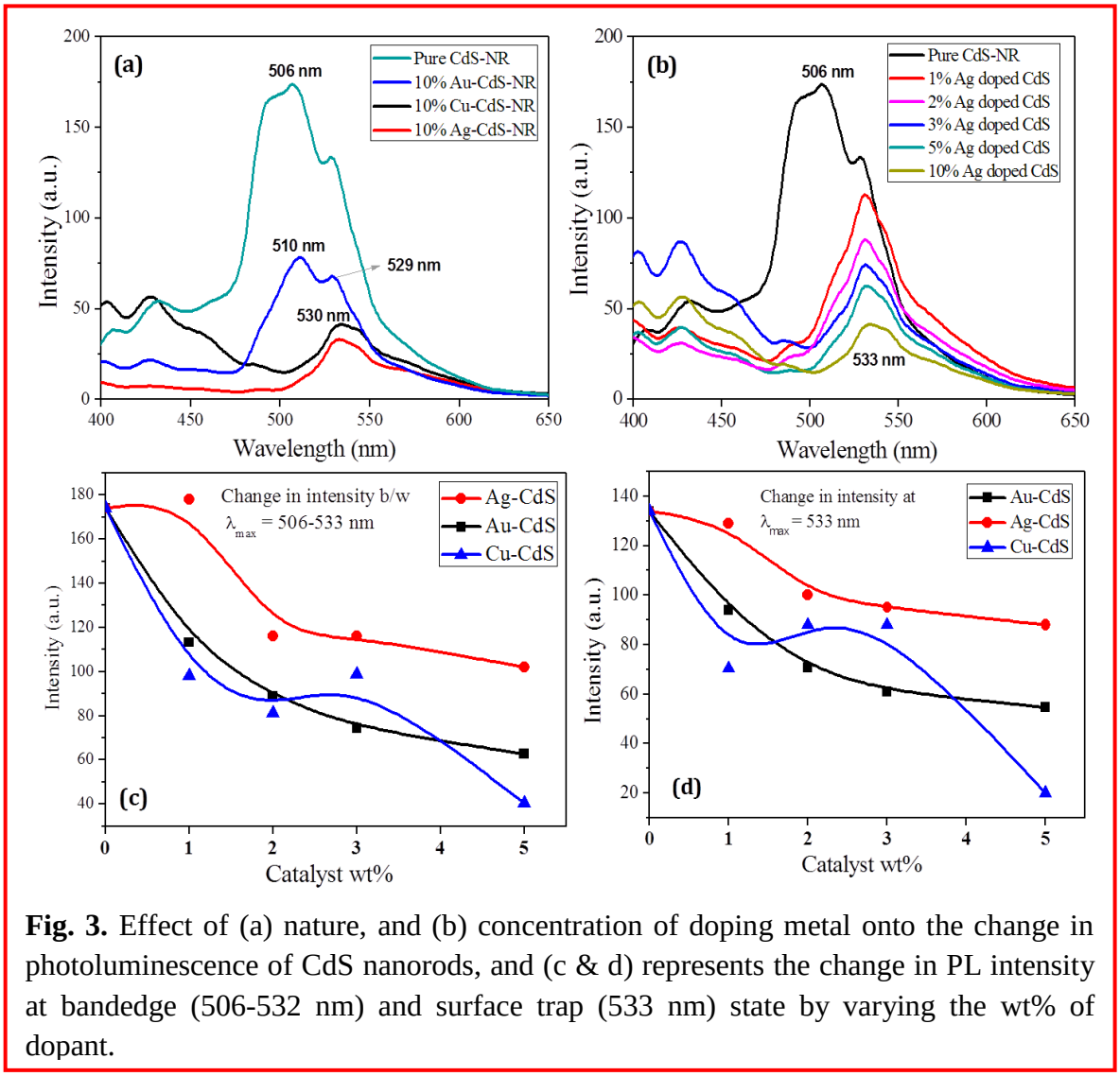

Fig. 3. Effect of (a) nature, and (b) concentration of doping metal onto the change in photoluminescence of CdS nanorods, and (c & d) represents the change in PL intensity at bandedge (506-532 nm) and surface trap (533 nm) state by varying the wt% of dopant.

8.3.2. Structural analysis

The XRD patterns are very similar and indexed to the hexagonal phase of the wurtzite crystal structure of CdS (JCPDS No. 41-1049 data card). No peaks of any other segregated phases (AuS, AgS or CuS) or impurities were detected even at 10 mol% loading, indicated the effective doping of metal ions into CdS hexagonal crystal. The average crystallite size was estimated based on the broadening of the {002} diffraction peak using the *Scherrer equation* are found to be 27.7, 22.6, 21.46, 21.45 and 13 nm for pure, and corresponding 1, 2, 3 and 5 mol wt%, respectively as shown in Fig 4.

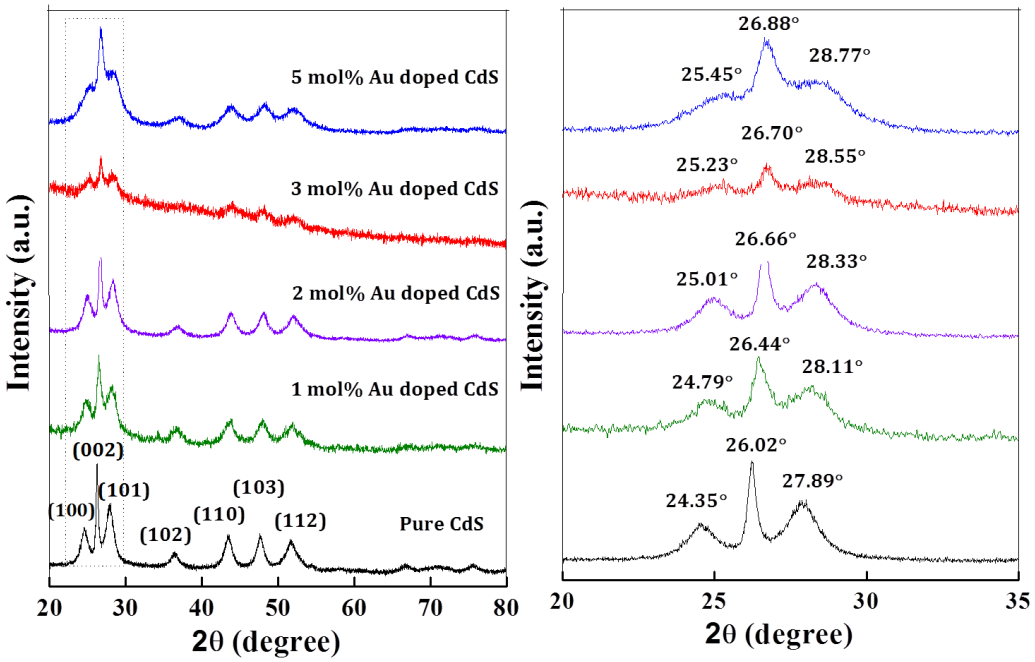

Catalysts	Pure CdS-NR	1% Au-CdS	2% Au-CdS	3% Au-CdS	5% Au-CdS
Crystallite size (nm)	27.70	22.64	21.45	21.41	13.00
Lattice size (°A)					
(a)	4.194	4.153	4.133	4.121	4.076
(c)	6.844	6.694	6.651	6.663	6.663

Fig. 4. X-ray diffraction patterns of $Au_xCd_{1-x}S$ (x = 0, 0.01, 0.02, 0.03, 0.05) and enlarge (100), (002), and (101) peaks reflecting their crystal distortion with various lattice and crystallite size parameters are summarized in table.

The concentration of Au^{3+} doping at different levels into CdS-NR led to a remarkable change in the distortion of crystal structure, which was observed by enlarging the graph between 20-35 degree angles. It has been observed that the increase in Au^{3+} doping content led to a decrease in a grain size from 27.70 nm to 13 nm and lattice size from a = 4.194 (c =6.844) to a = 4.076 (c = 6.663) A°. The various lattice parameters and crystallite sizes as an effect of doping are summarized in the table of Fig. 4.

A similar trend has been observed in case of Ag^{+} and Cu^{2+} doped CdS samples as shown in Fig. 5 and 6. It can be seen that diffraction peaks (especially along 100, 002 & 101) & (110, 103 &

112) planes, shifted to higher and lower degree side (2θ) as the CdS was doped with coinage metals due to lattice mismatching.

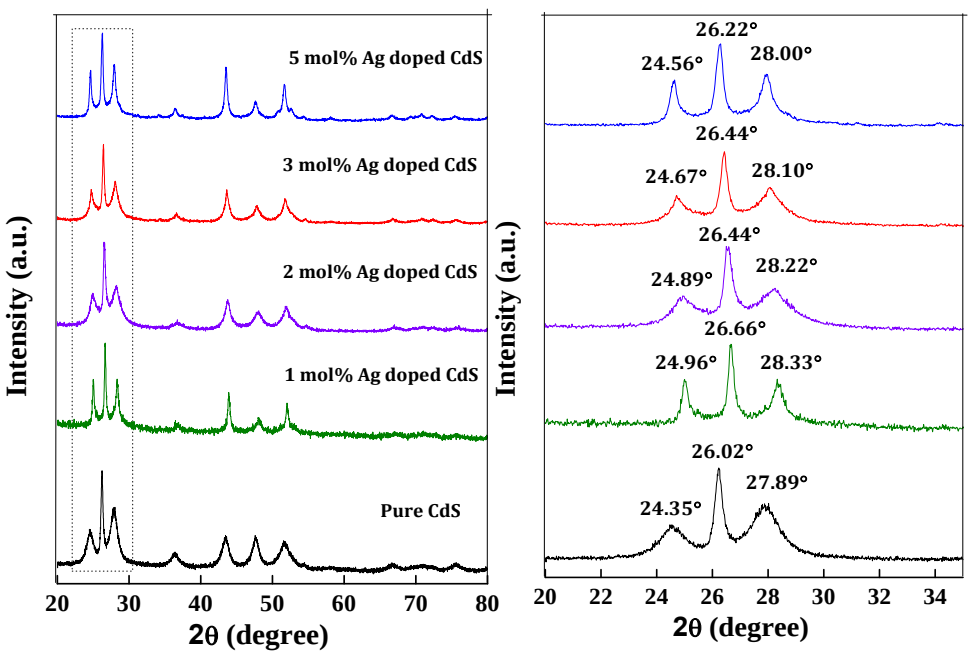

Catalysts	Pure CdS-NR	1% Ag-CdS	2% Ag-CdS	3% Ag-CdS	5% Ag-CdS
Crystallite size (nm)	27.70	38.00	36.90	31.40	30.80
Lattice size (°A)					
(a)	4.194	4.123	4.142	4.167	4.173
(c)	6.844	6.721	6.723	6.774	6.781

Fig. 5 (a) X-ray diffraction patterns of $Ag_xCd_{1-x}S$ (x = 0, 0.01, 0.02, 0.03, 0.05) and enlarge (100), (002), and (101) peaks reflecting their crystal distortion with various lattice and crystallite size parameters are summarized in table.

The atomic radii of Au^{3+}, Ag^{+} and Cu^{2+} are 144, 144, 128 pm found to be little mismatched with Cd has atomic radii 144 ±9 pm. Thus the incorporation of these metals into hexagonal CdS led to a remarkable distortion in the structure. A corresponding shift in 2θ values and lattice parameters has been summarized in the table.

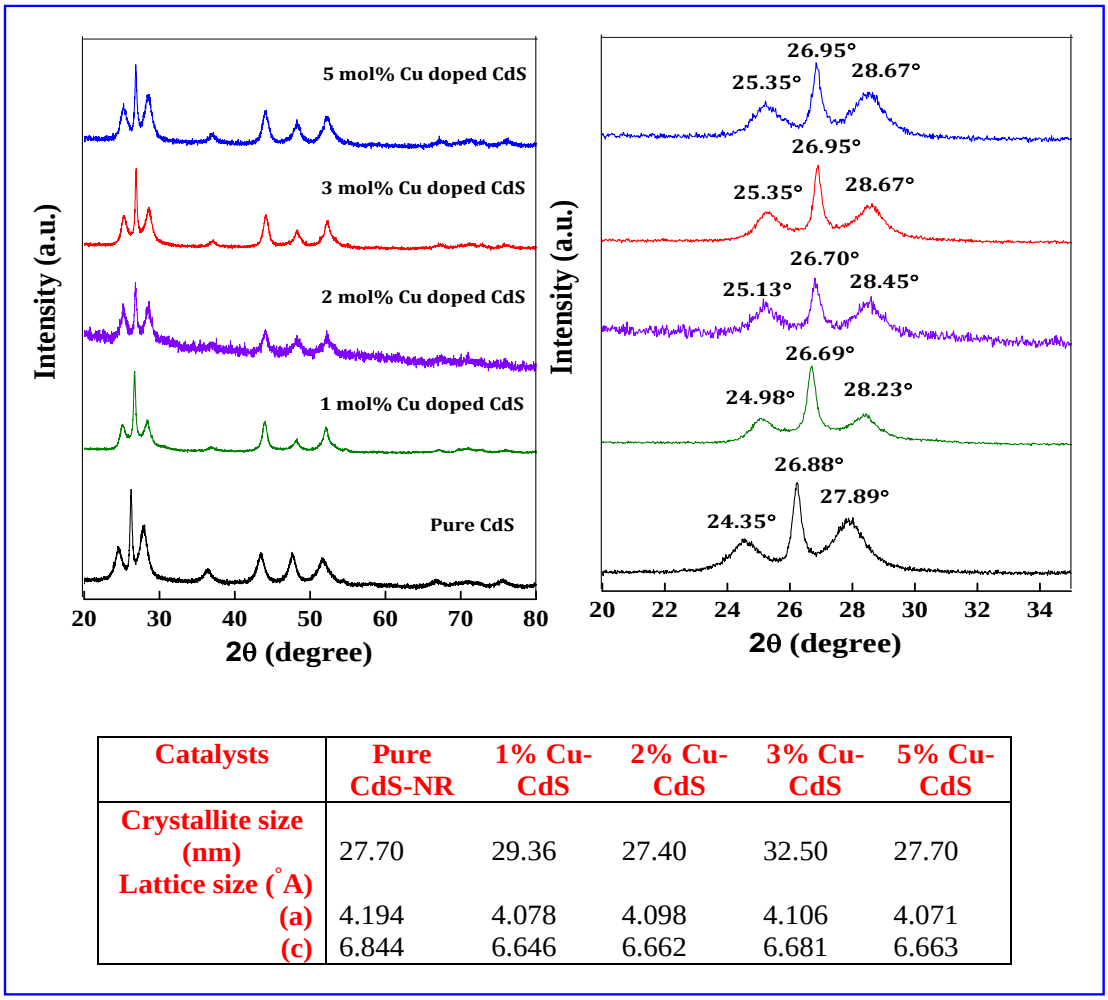

Catalysts	Pure CdS-NR	1% Cu-CdS	2% Cu-CdS	3% Cu-CdS	5% Cu-CdS
Crystallite size (nm)	27.70	29.36	27.40	32.50	27.70
Lattice size (°A)					
(a)	4.194	4.078	4.098	4.106	4.071
(c)	6.844	6.646	6.662	6.681	6.663

Fig. 6 (a) X-ray diffraction patterns of $Cu_{1-x}Cd_xS$ (x = 0, 0.01, 0.02, 0.03, 0.05) and enlarge (100), (002), and (101) peaks reflecting their crystal distortion with various lattice and crystallite size parameters are summarized in table.

Lattice parameters were calculated and compared with pure CdS-NR to observe the crystal distortion. Lattice size (given in table 1) was calculated to be 6.844, 6.694, 6.663, and 6.663 nm for pure, 1, 3 and 5 mol% Au^{3+} doped CdS-NR. The slight decrease in lattice size is justified the mismatching of ionic radii of different metals with Cd^{2+} ion.

The *surface area* of pure CdS-NR was found to be 90.56 m^2/g while, 1 mol% Au^{3+}, Ag^{+} and Cu^{2+}-doped CdS-NR exhibited a surface area of 60.44, 55.05 and 6.87 m^2/g. The decrease in the surface area for coinage metal-doped CdS can be attributed to the partial filling of the pores in CdS by Au^{3+}, Ag^{+} and Cu^{2+} nanoparticles. A similar trend of results previously observed for semiconductors doped with transition metals. Further, the effect probably depends upon the

individual metal characteristics. Interestingly, an increase in doping content (mol %) into CdS-NRs significantly decreases its surface area. The surface area has been found to be decreased further; 40.55, 35.75 and 17.05 m^2/g corresponds to 2%, 3% and 5% Au doped CdS-NRs as a function of their high density of pores filing with increasing wt. content.

The dissimilar effect of different coinage metals as a function of their number of unpaired electrons has been evaluated further by their *Magnetic susceptibility* values. Magnetic susceptibility, the degree of magnetization induced by materials in the presence of external magnetic field, was calculated for pure and doped CdS samples by Goy's magnetic susceptibility apparatus. By using the equation,

$$\chi_g = CL\,(R\text{-}R_o) / m\,(10^9)$$

Where, C is the calibration constant, the L = length of sample, R = susceptibility value for known wt of sample, R_o = susceptibility value for std. compound (- 31), m = mass of sample in grams. Magnetic susceptibility has been found to be -27,251 × 10^{-9} for pure CdS-NR. Significantly, magnetic susceptibility has been found to be -24,870 × 10^{-9}, -20,456 × 10^{-9} and -15,787 × 10^{-9} for 1, 2 and 5% Au^{3+} doped CdS samples. The negative values of magnetic susceptibility indicated the diamagnetic character of pure and doped CdS samples. The less negative values for Au doped CdS-NRs that are notably increases with wt% reflected towards their less diamagnetic characters due to replacement of Cd^{2+} cations with metal ions having unpaired electrons.

The photovoltaic behavior (J-V) or current density -voltage characteristics of 5 mol% Au doped CdS-NR in comparison to pure CdS sample is shown in Fig. 6. The curve corresponding to Ruthenium-based N719 dye sensitized CdS-NR indicates a short circuit current (*J*sc = 0.270 mA/cm^2), an open circuit voltage (V_{oc} = 23.9 mW), fill factor = 0.283 and efficiency (η) = 1.82 x 10^{-3} %. This trend is improved with

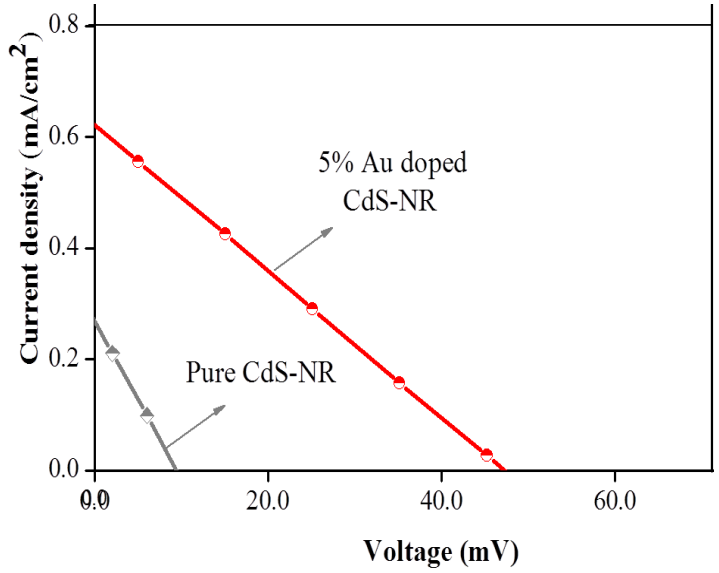

Fig. 7. Current density-voltage characteristics for pure and 5% Au doped CdS-NRs on TiO_2 substrate.

doping of Au into CdS-NR with (Jsc = 0.552 mA/cm^2), an open circuit voltage (V_{oc} = 47.4 mW), fill factor = 0.246 and efficiency (η) = 6.46 x 10^{-3} %. Thus, reduction in e^-/h^+ recombination rate as Au^{3+} doped act as a sink for the photogenerated charge carriers seems to be the cause of its better performance over undoped sample. Doping of Au^{3+} into CdS-NR (5 mol%) remarkably increase its light absorption (harvesting) capacity beyond of its limiting range and at the same time decrease in band gap position quickly transfer photogenerated charge carriers to TiO_2 electrode and boost the overall efficiency.

8.3.3. Morphological and composition study

TEM analysis revealed the nanorods like morphology of 2% Au^{3+}, Ag^+ and Cu^{2+} doped CdS nanorods as shown in Fig. 8. The length and diameter of these nanorods lie in the range of 100-150 nm and 5-10 nm. Elemental detection X-ray (EDX) study was carried out to get an idea of present metal and their atomic weight %. However, the elemental analysis carried out using EDX confirms the presence of 1.88, 2.58 and 1.39 atomic weight % of Au^{3+}, Ag^+ and Cu^{2+} in 2% doped CdS samples.

8.3.4. Photocatalytic study

The effect of nature and varying concentration of coinage metals has been tested by a photooxidation of salicyldehyde shown in Fig. 9. Photolysis and dark adsorption led to a very little change in concentration of the salicyldehyde. In contrast,

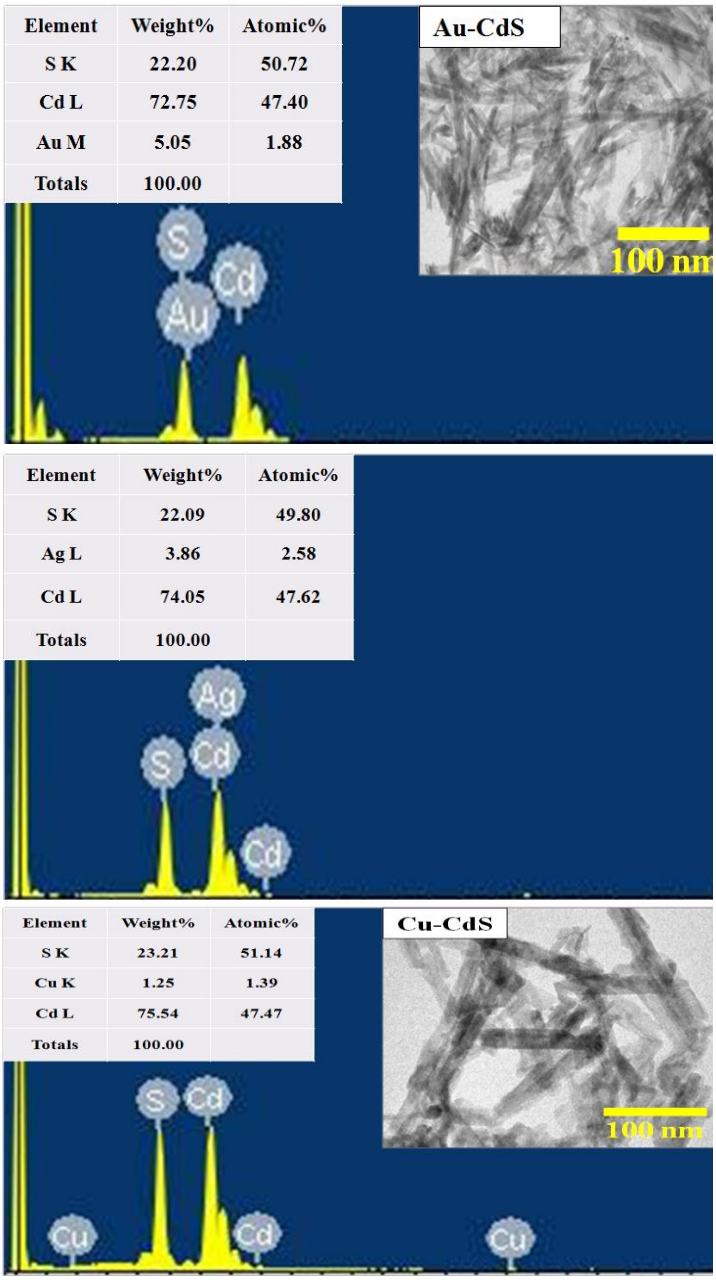

Fig. 8. EDX patterns of 2 mol% Au, Ag and Cu doped CdS-NR and in inset their corresponding TEM images.

doping of Au^{3+}, Ag^{+} and Cu^{2+} led to a sharp change in concentration of salicyldehyde and the rate of the photooxidation of salicyldehyde has been found to be as; CdS < Cu^{2+}-CdS < Ag^{+}-CdS < Au^{3+}-CdS (Fig. 9a).

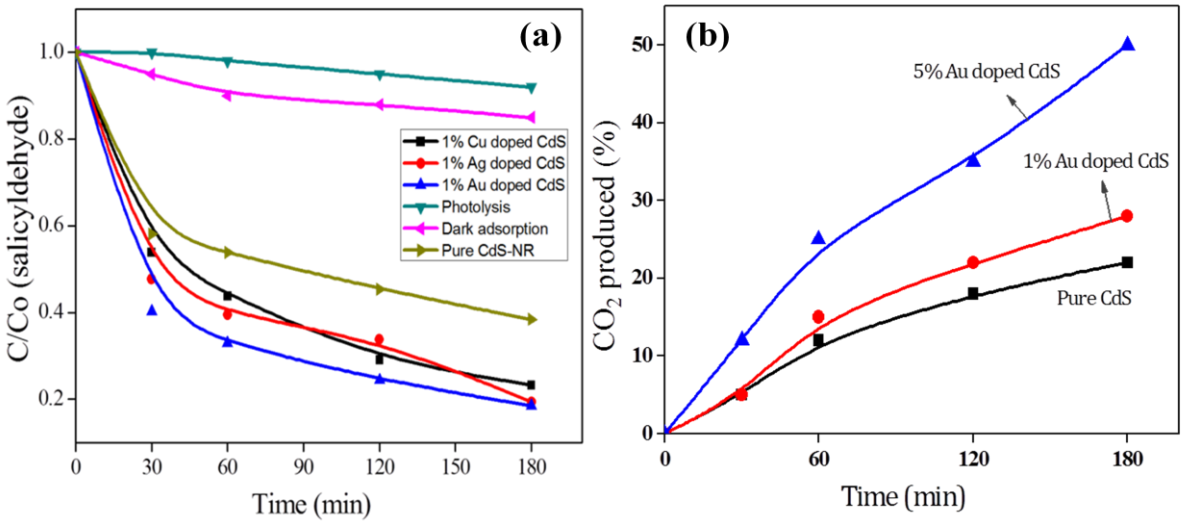

Fig. 9. (a) C/Co Plots of Salicyldehyde (0.5 mM) with time, and (b) corresponding CO_2 produced (%) by various pure and M-doped CdS samples.

The % degradation has been found to be noticeably improved; 42, 55, 60 and 64% for pure, 1 mol% Cu^{2+}, Ag^{+} and Au^{3+} doped CdS-NR after 1 hour of sunlight exposure. Varying the Au^{3+} content into CdS matrix led to a remarkable increased in photoactivity i.e., 64, 66, 80 and 83% for 1, 2, 3 and 5 mol% Au^{3+} doped samples. *This can be well explained on the basis of better Fermi level* [18] *equilibration ((+0.5 V versus NHE) than the conduction band of CdS (−1.0 V versus NHE)) and higher surface area 60.44 m^2/g in comparison to very less for Cu^{2+} doped CdS-NR 6.87 m^2/g, which result in better adsorption by availing higher number of active sites and thereby, accelerate the PCA. Interestingly, less grain size for Au^{3+} doped CdS-NR (22 nm) and number of defects as evident from PL study, in comparing to Ag^{+} and Cu^{2+} doped samples seems to be a possible reason for its better performance. Current density-voltage characteristics also signify the real role play by Au^{3+} doped CdS sample in terms of light harvesting capacity beyond of its limiting range and shift in band edge positions.*

The linear increase in CO_2 production has been observed in the first two hours, and after that rate of production become quite slow (Fig. 9b). Hence, 5% Au^{3+} doped CdS-NR exhibited maximum mineralization of salicyldehyde and hence the optimum CO_2 rate. The % production of CO_2 after

long time exposing to sunlight was found to be 22, 28 and 50 % for pure, 1 and 5% Au doped CdS samples.

The effect of nature and concentration of coinage metals in their photocatalytic properties was tested by reduction of m-dinitrobenzene (m-DNB, 5 mM) under UV light irradiations (Fig. 10).

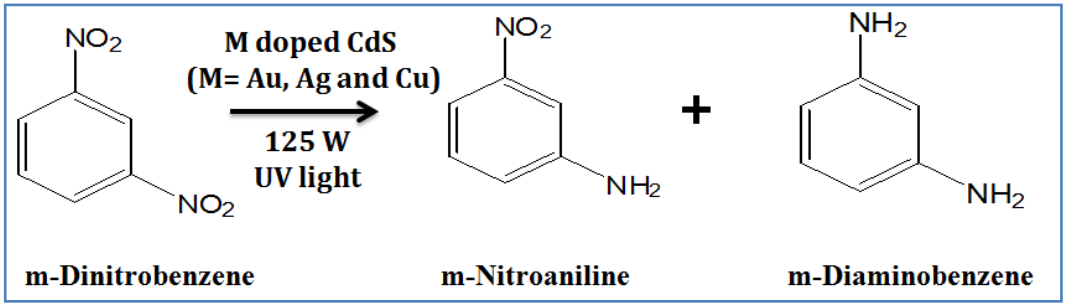

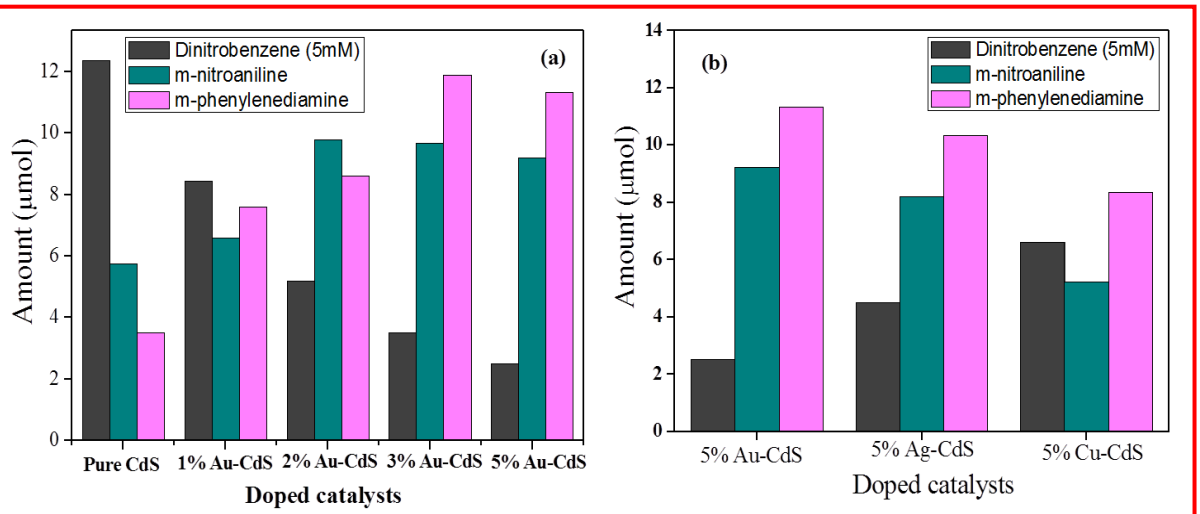

Fig. 10. Histogram of photoreduction of 5 mM m-DNB after 5 h of UV light irradiations by the effect of (a) concentration, (b) nature of doping metal.

It has been observed that the photoreduction rate (µmol) of m- DNB was improved with increasing doped content from 1% to 5 % relative to undoped sample over the different time periods. Comparative trend m-DNB reduction by varying the content of Au^{3+} doping into CdS and variation in nature of doping is shown in Fig. 10a and 10b. The rate of reduction was found to be increased by increasing the Au^{3+} doping content. Further, in 5% Au^{3+}, Ag^{+} and Cu^{2+} doped CdS-NR, 5% Au^{3+} doped CdS-NR sample found to be best in photoreduction of m-DNB in comparison to Ag^{+} and Cu^{2+} doped samples. Corresponding formation of m-phenylenediamine

(PDA) and m-nitroaniline (NA) with the decrease in concentration of m-DNB has been also given.

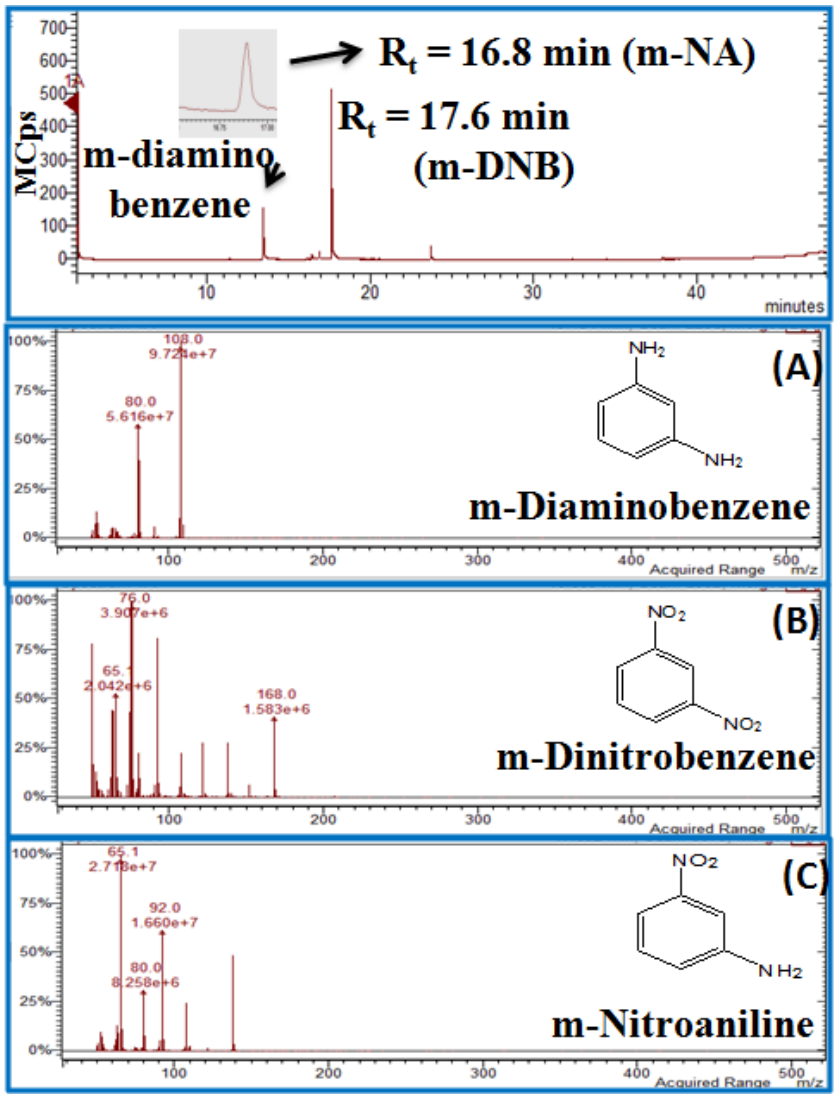

Fig. 11. GC-MS analysis of m-DNB with 5% Au doped CdS after irradiations with UV light of 2h.

The GC-MS analysis as given in Fig. 11, confirmed the presence of m-DNB and its important intermediates; m-diaminobenzene and m-nitroaniline at retention time 16.8, 13.5, and 16.8 respectively during 2 h reaction.

Similarly, reduction of 4-nitrobenzaldehyde (5 mM) has been carried out with different Au, Ag and Cu metals and with their wt%. These histograms suggested that Au^{3+} doped CdS-NRs (Fig. 12a) proved to be the best photocatalyst for the reduction of 4-nitrobenzaldehyde in comparison

to other Ag^{+} (Fig. 12b) and Cu^{2+} (Fig. 12c) doped CdS-NR under similar conditions. The reduction was found to be accelerated further by increasing the wt. content of Au doping. A comparative graph (Fig. 12d) of 4-nitrobenzaldehyde with pure, Au^{3+}, Ag^{+} and Cu^{2+} doped CdS-NR was also given.

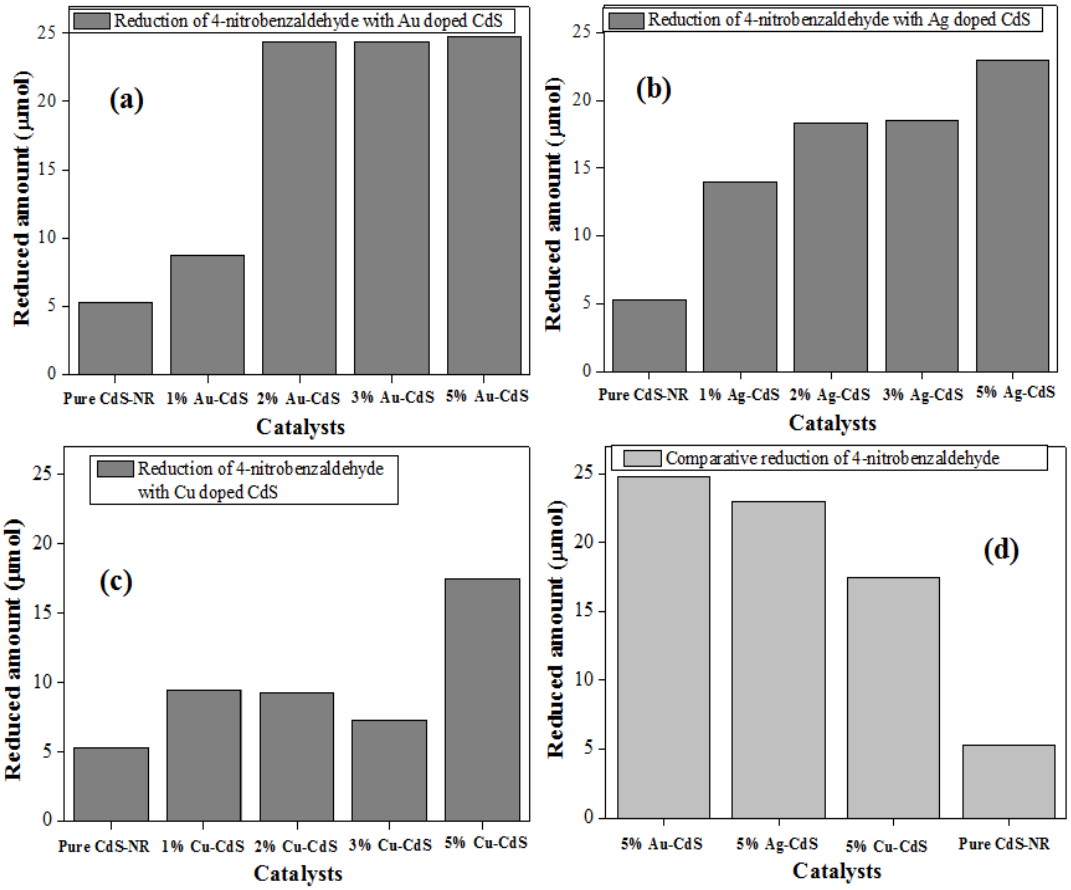

Fig. 12. Histogram showing photoreduction of 4-nitrobenzaldehyde (5 mM) with various Au, Ag and Cu doped CdS samples under UV light exposure of 2 h.

The effect of nature of metal and its doping concentration influenced photophysical, photochemical and structural properties of CdS-NR. Absorbance and luminescence features of CdS-NR can be easily controlled by the appropriate doping content of Au, Ag and Cu metal ions. Au doped CdS-NR found to be the best photoactive catalyst for oxidation of salicyldehyde and reduction of nitroaromatics as a function of their increase surface area, improved current-voltage characteristics, less grain size, and better Fermi level contact.

8.4. References

[1] W. Zheng, K. Singh, Z. Wang, J. T. Wright, J. V. Tol, N. S. Dalal, R. W. Meulenberg, G. F. Strouse, J. Am. Chem. Soc. 134 (2012) 5577–5585.

[2] W. Zheng, G. F. Strouse, J. Am. Chem. Soc. 133 (2011) 7482–7489.

[3] W. Zheng, P. Kumar, A. Washington, Z. Wang, N.S. Dalal, G.F. Strouse, K. Singh, J. Am. Chem. Soc. 134 (2012) 2172–2179.

[4] T.E. Rosson, S.M. Claiborne, J.R. McBride, B.S. Stratton, S.J. Rosenthal, J. Am. Chem. Soc. 134 (2012) 8006–8009.

[5] R. Begum, A. Chattopadhyay, Langmuir 27 (2011) 6433–6439.

[6] P.R. Yu, K. Zhu, A.G. Norman, S. Ferrere, A.J. Frank, A.J. Nozik, J. Phys. Chem. B 110 (2006) 25451−25454.

[7] P.V. Kamat, J. Phys. Chem. C 112 (2008) 18737−18753.

[8] N. Guijarro, T. Lana-Villarreal, I. Mora-Sero, J. Bisquert, R. Gomez, J. Phys. Chem. C 113 (2009) 4208−4214.

[9] A. Salant, M. Shalom, I. Hod, A. Faust, A. Zaban, U. Banin, ACS Nano 4 (2010) 5962−5968.

[10] X.G. Peng, L. Manna, W.D. Yang, J. Wickham, E. Scher, A. Kadavanich, A.P. Alivisatos, Nature 404 (2000) 59−61.

[11] J. Ouyang, C.I. Ratcliffe, D. Kingston, B. Wilkinson, J. Kuijper, X. Wu, J.A. Ripmeester, K. Yu, J. Phys. Chem. C 112 (2008) 4908-4919.

[12] M. Luo, Y. Liu, J. Hu, H. Liu, J. Li, ACS Appl. Mater. Interfaces 4 (2012) 1813−1821.

[13] P.V. Kamat, J. Phys. Chem. C 111 (2007) 2834–2860.

[14] B. Levy, J. Electroceram. 1 (1997) 239–272.

[15] M. Greatzel, Chem. Ing. Tech. 67 (1995) 1300–1305.

[16] M. Ni, M.K.H. Leung, D.Y.C. Leung, K. Sumathy, Renewable Sustainable Energy Rev. 11 (2007) 401–425. (e)

[17] A.B. Murphy, P.R.F. Barnes, L.K. Randeniya, I.C. Plumb, I.E. Grey, M.D. Horne, J.A. Glasscock, Int. J. Hydrogen Energy 31 (2006) 1999–2017.

[18] P.V. Kamat, B. Shanghavi, J. Phys. Chem. B 101 (1997) 7675.

Conclusions

Summary of work

Chapter 1: Summarize the brief introduction and literature survey on heterogeneous photocatalysis using bare and metal-semiconductor nanostructures. Specific attention has been paid on cadmium sulfide (CdS) vis-à-vis their structure, morphology, their heterocomposites with coinage metals (Au, Ag & Cu) and their fascinating practical applications.

Chapter 2: Gives a brief description of various techniques used for synthesis and characterize bare CdS and Au/Ag−CdS composite nanostructures. CdS nanostructures of different morphologies such as; nanospheres, nanorods and nanowires of different dimensions have been synthesized by reverse micelles method, solvothermal and anodic alumina membrane (AAM) template techniques by controlling reaction conditions. Coinage metals (Au, Ag & Cu) have been introduced on/in CdS surface by means of in-situ deposition, photodeposition, impregnation and doping techniques. Sophisticated instruments; UV-vis & Diffused reflectance spectroscopy, Photoluminescence and Time resolved spectroscopy, Scanning (SEM) & Transmission electron microscope (TEM), Field emission- electron microscope (FE-SEM), High resolution (HR-TEM), BET surface analyzer, X-ray diffraction, current-voltage (IV) characteristics curves, High Performance Liquid Chromatography (HPLC), Gas chromatography-mass spectroscope (GC-MS) and Gas chromatography (GC) have been commonly used in characterization of nanomaterials to get an idea of size, shape, defects, crystal structure, crystallite size, conduction, and expected products/ intermediates.

Chapter 3: Describes the effect of size, shape and nature of metal co-catalysts, pH, and concentration of solution, catalyst loading, and light intensity for the photocatalytic degradation of salicylic acid by various bare CdS and M-CdS (M= Au, Ag & Cu) nanorods. It has been identified that photoactivity was significantly improved by tuning the morphology from NS to cylindrical symmetry; CdS-NR, and further by metal deposition (Au-CdS-NR > Ag-CdS-NR > Cu-CdS-NR > CdS-NR) as a function of superior charge delocalization and charge rectification. It is demonstrated that fluctuation of size, shape and nature of metal co-catalysts loading could be beneficial in designing highly active photocatalyst responsive in visible region for solar detoxification of toxic organic pollutants

Chapter 4: Presented a fine insight in the growth of CdS nanostructures with tunable aspect ratio by controlling their reaction conditions, especially reaction time at a particular temperature of autoclaving. The photocatalytic activity for salicylic acid oxidation under UV irradiation is gradually improved with the increasing crystallinity, length, exposed surface area per particle and decreasing surface area, surface to volume ratio and aspect ratio. The photodeposition of Au and Ag co-catalysts nanoparticles of different sizes onto CdS nanorod significantly reduced the PL emission but substantially increases the photoactivity for salicylic acid oxidation. This report indicates that, like metal oxides, nanoscale metal sulfide semiconductors of tunable aspect ratio can exhibit improved photoactivity under sun light illumination.

Chapter 5: Demonstrates the importance of CdS nanoparticles size and shape in controlling their relaxation lifetime to achieve optimum rate for photo-oxidation of salicylic acid and reduction of p-nitrophenol. Longer and wider CdS nanorods exhibited better photoactivity in comparison to spherical particles as a function of their increase lifetime of charge carriers, crystalline nature of CdS nanorod having fewer surface defects, increased delocalization of electrons–holes along lengthy CdS morphology etc. Silica coated CdS nanorods proved to be highly efficient in respect of photostability to overcome its photochemical dissolution and thereby improves the photoactivity for longer light exposure. Hence, control of surface structure, geometric dimensionality and tuning crystallinity may lead to a highly photoresponsive CdS nanostructure.

Chapter 6: Summarize the importance of effective contact area developed by M-nanorod−SC-nanorod {Au(NR)–CdS(NR)} interface, owing to the longer relaxation lifetime than conventional metal–semiconductor junctions. Interestingly, Au(NR)–CdS(NR) nanocomposites result in improved stability and the activity, which did not decrease even after three recycles. Notably, very low resistance and thus high conductance in Au(NR)–CdS(NR) in contrast to bare CdS and Au(NS)–CdS(NR) composites, highlights the importance of interface in conduction. The overall high performances of Au nanorod–CdS nanorod composite can be well explained in terms of beneficial advantages of charge transport kinetics at the coupled nanorod interface. These observations open up new opportunities to highly improve the efficiency of solar cells.

Chapter 7: Presented a method of self assembles longer and wider crystalline CdS–nanowires very similar to spinning wool like morphology by using anodic alumina membrane (AAM) template. It has been experimented that higher crystallinity, least surface defects, better charge

separation evident from longer relaxation lifetime seems to be the cause for its outstanding performance and maximum (>80%) photoluminescence quenching in 1D-CdS nanowires. Many beneficial surface properties of lengthy CdS nanowires for efficient removal of toxic dyes under solar exposure as compared to the very poor activity of conventional photocatalyst materials are summarized.

Chapter 8: Summarize the effect of nature of metal and its doping concentration on absorption, photoluminescence, photochemical and structural properties of CdS-NR. Variety of colors of CdS can be easily tuned by variation in the content and nature of coinage doping metal. Au doped CdS-NR (1-5%) found to be the best photoactive catalyst for oxidation of salicyldehyde and reduction of nitroaromatics as a function of their increase surface area, improved current-voltage characteristics, less grain size, and better Fermi level contact.

List of Publications

[1] **Rohit Singh** and Bonamali Pal, "Fine-tuning the photoluminescence and photocatalytic properties of CdS nanorods of varying dimensions," **Materials Research Bulletin** 48 (2013) 1403–1410.

[2] **Rohit Singh** and Bonamali Pal, **"**Study of excited charge carrier's lifetime for the observed photoluminescence and photocatalytic activity of CdS nanostructures of different shapes," **Journal of Molecular Catalysis A: Chemical** 371 (2013) 77–85.

[3] **Rohit Singh** and Bonamali Pal, **"**Highly enhanced photocatalytic activity of Au nanorod–CdS nanorod heterocomposites," **Journal of Molecular Catalysis A: Chemical** 378 (2013) 246–254.

[4] **Rohit Singh** and Bonamali Pal, **"**Woolen bun shaped CdS microspheres enfolded 1D nanowires for the superior photooxidation of dyes: A comparative case study**" Journal of Molecular Catalysis A: Chemical** 396 (2015) 15–22.

[5] **Rohit Singh** and Bonamali Pal**,** "Enhanced photocatalytic activity of coinage metal cadmium sulfide nanorod composites under sun light irradiation," **Advanced Materials Research,** 678 (2013) 189-192**.**

[6] Jaspreet Kaur, **Rohit Singh** and Bonamali Pal, "Influence of coinage and platinum group metal co-catalysis for the photocatalytic reduction of *m*-dinitrobenzene by P25 and rutile TiO_2" **Journal of Molecular Catalysis A: Chemical**, DOI:10.1016/j.molcata.2014.11.007**.**

[7] Bonamali Pal, **Rohit Singh and** Shilpa Singla "Effect of Au and Pt deposition and thermal treatment on the photocatalytic activity of as-prepared ZnS nanorod**, International Journal of Nanoscience**, 12 (2013) 13500324.

[8] **Rohit Singh** and Bonamali Pal, "Influence of Au photodeposition and doping in CdS nanorods: optical and photocatalytic study, **Particulate Science and Technology** DOI:10.1080/02726351.2014.933148.

[9] **Rohit Singh** and Bonamali Pal, "Preparation, surface and crystal structure, band energetics, optoelectronic and photocatalytic properties of $Au_xCd_{1-x}S$ nanorods" under review in **ChemPlusChem**.

Papers/ posters in Conferences

[1] **Rohit Singh** and Bonamali Pal, "Preparation and Characterization of CdS Nanorods of Varying Aspect Ratio for Photocatalytic Reaction" National Symposium on Nanoscience and nanotechnology **(Nanostech – 2011),** Benchmarking- Science and Society.

[2] Rohit Singh and Bonamali Pal, "Photoresponsive Properties of Cadmium Sulfide (CdS) Nanorods of Variable Aspect Ratio Prepared by Two Different Techniques" International Conference on Frontiers in Nanoscience, Nanotechnology & their Applications (**NanoSciTech– 2012).**

[3] **Rohit Singh** and Bonamali Pal, "Ag-Doped CdS Nanorods with the Enhanced Photoluminescence and Photoactivity," International conference on Emerging Technology: Micro to Nano **(ETMN– 2013).**

[4] **Rohit Singh** and Bonamali Pal, "Influence of Au Photodeposition and Doping in CdS Nanorods: Optical and Photocatalytic study," International Conference on Powder, Granule and Bulk Solids: Innovations and Applications **(PGBSIA– 2013).**

[5] **Rohit Singh,** Nidhi Gupta, Rupinder Kaur and Bonamali Pal, "Preparation of Metal - CdS Nanorod Composite and Their High Photocatalytic Activities," **Poster presentation** at International Conference on Nanotechnology and Medical Sciences **(ICNAMS)** October 21-23, 2010, D. Y. Patil University, Kohlapur.

[6] **Rohit Singh** and Bonamali Pal, "Excited Charge Carrier's Lifetime Controlled Photoluminescence and Photoactivity in CdS Nanostructures," **Poster presentation** at National Conference on Recent Advances in Chemical & Environmental Sciences **(RACES),** March 03, 2012, Multani Mal Modi College, Patiala.

[7] **Rohit Singh** and Bonamali Pal, "Improved photoluminescence and photocatalytic properties of Au-CdS heterocomposites through interface control," **Poster presentation** at national Conference on innovative molecules for sustainable future **(NCIMSF-2013)** October 24-26, 2013, Thapar University Patiala.